1-1-2016

Hard, Soft, and Sticky Spheres for Dynamical Studies of Disordered Colloidal Packings

Matthew Daniel Gratale
University of Pennsylvania, mgratale@sas.upenn.edu

Hard, Soft, and Sticky Spheres for Dynamical Studies of Disordered Colloidal Packings

Abstract
This thesis describes experiments which explore the role of interparticle interactions as a means to alter, and control, the properties of dense colloidal packings.

The first set of experiments studied phonon modes in two-dimensional colloidal crystals composed of soft microgel particles with hard polystyrene particle dopants distributed randomly on the triangular lattice. By mixing hard and soft spheres we obtain close-packed lattices of spheres with random bond strength disorder, \textit{i.e.,} the effective springs coupling nearest-neighbors are either very stiff, very soft, or of intermediate stiffness. Video microscopy, particle tracking, and covariance matrix techniques are employed to derive the phonon modes of the corresponding ``shadow'' crystals, thereby enabling us to study how bond strength disorder affects vibrational properties. Hard and soft particles participate equally in low frequency phonon modes, and the samples exhibit Debye-like density of states behavior characteristic of crystals at low frequency. For mid- and high-frequency phonons, the relative participation of hard versus soft particles in each mode is found to vary systematically with dopant concentration.

The second set of experiments investigated depletion interaction potentials between micron-size colloidal particles induced by nanometer-scale micelles composed of the surfactant hexaethylene glycol monododecyl ether (C$_{12}$E$_{6}$). The strength and range of the depletion interaction is revealed to arise from variations in shape anisotropy of the rod-like surfactant micelles. This shape anisotropy increases with increasing sample temperature. By fitting the colloidal interaction potentials to theoretical models, we extract the rod-like micelle length and shape anisotropy as a function of temperature. This work introduces micelle shape anisotropy as a means to control interparticle interactions in colloidal suspensions, and shows how interparticle depletion potentials of micron-scale objects can be employed to probe the shape and size of surrounding macromolecules at the nano-scale.

The third set of experiments explored variation in the vibrational properties of colloidal glasses induced by changes in interparticle interactions. In particular, we study the vibrational phonons of quasi-2D colloidal glasses whose interparticle interactions are controlled via the temperature tunable depletion interaction described in the aforementioned experimental work. This tunable attraction enables us to study the changes in the properties of a colloidal glass as the interparticle attraction strength is gradually increased from weak (nearly hard-sphere) to strong. We observed that particle dynamics slow monotonically with increasing attraction strength and eventually plateau at very high attraction strength. The shape of the phonon density of states is also revealed to change with increasing attraction strength; specifically, glasses with low interparticle attraction strength exhibit comparatively more low frequency modes than glasses with high interparticle attraction strength.

Degree Type
Dissertation

Degree Name
Doctor of Philosophy (PhD)

HARD, SOFT, AND STICKY SPHERES FOR DYNAMICAL STUDIES OF DISORDERED COLLOIDAL PACKINGS

Matthew Daniel Gratale

A DISSERTATION

in

Physics and Astronomy

Presented to the Faculties of the University of Pennsylvania in Partial

Fulfillment of the Requirements for the Degree of Doctor of Philosophy

2016

_____

Arjun G. Yodh, Professor of Physics and Astronomy

Supervisor of Dissertation

_____

Marija Drndic, Professor of Physics and Astronomy

Graduate Group Chairperson

Dissertation Committee

Ravi Sheth, Professor of Physics and Astronomy

Peter Collings, Adjunct Professor of Physics and Astronomy

Piotr Habdas, Adjunct Professor of Physics and Astronomy

Marija Drndic, Professor of Physics and Astronomy

HARD, SOFT, AND STICKY SPHERES FOR THE DYNAMICAL STUDIES OF DISORDERED COLLOIDAL PACKINGS

Dedication

To my family.

Acknowledgements

It has been a long and winding road, and I would not be where I am today without the support of so many people.

First and foremost, my wife Kim, my better half in every sense, has been so important to me during this time. Kim, thank you for your love and support, and for our life together. I can't wait for the new adventures awaiting us in Orlando and wherever else life takes us. The rest of my family, my giant, loud, italian family, have been absolutely amazing. My parents have been there for me whenever and with whatever I needed. I hope someday I will be able to repay them for all they have done for me, and at the very least pay it forward to my children. My brother Mike and cousin Mary have an uncanny ability to make me forget whatever troubles I am having when we are together. They have kept me sane perhaps more than I can even imagine, and their support has been instrumental in all that I've done in my life. The little ones, Frederick, Mikey, and Marie, always put a smile on my face. To the rest of my family, there are too many of you to thank individually, but I just want to say, "firm embrace". Last but not least, my cat Annie was the best source of comfort and love anyone could ask for from a 12-plus pound ball of fur and attitude.

My advisor, Arjun Yodh, is an amazing mentor. He allowed me to explore my own research ideas, but pushed me to put the work in to prove the experiment was a worthwhile endeavor. He also taught me to be critical of all of my work, pushing that work to be the best it could possibly be. His patience and guidance have made me an infinitely better scientist. I truly appreciate all he has done for me.

I had the pleasure of working with some of the smartest, nicest, and funnest people over these

past seven plus years. My labmates were not only incredibly helpful in my scientific research, but also made everyday in lab a lot of fun. Peter Yunker was a huge help with many of the projects I worked on, and our daily sports conversation were some of the greatest since Saving Private Ryan. Matt Lohr's sense of humor and awful/amazing impressions made everyday a joy. Oni Basu is one of the sweetest people I have ever met. She took me under her wing when I first started in lab and was so amazingly supportive. Tim Still was an immense help to all of the my projects and was also a great friend. Ye Xu was my crackpot idea partner in crime. I had a lot of crazy ideas for experiments, and Ye was always supportive of these ideas and pushing me to explore them further. Luckily, Tim was around to reel us in with some of the crazier ideas. Zoey Davidson's programing skills were a great resource and he always knew the best places to go in Philadelphia. Wei-Shao Wei was an awesome office mate. We had a lot of fun in LRSM 305. Xiaoguang (Max) Ma was instrumental in my attractive glass project. I shiver at thinking about the state of that project without him. Caitlin Matyas only worked in the lab one summer, but was an absolute trooper, recording much of the data for my depletion experiments. There are a lot of other people, past and present, from the group I want to thank. Dan Chen, Zexin Zhang, Joonwoo Jeong, Angel Martinez, Bart Machielse, Sam Lobel, Ke Chen, Ahmed Alsayed, Yilong Han, Remi Dreyfus and Coline Bretz were all a great help to my research.

I've also been fortunate to work in collaboration with Piotr Habdas, from St. Joseph's University, Kevin Aptowicz, from West Chester University, and Peter Collings, from Swarthmore College. They all provided great insight into my various projects, and it was rewarding to work with each of them extensively on individual projects. Andrea Liu and her students Carl Goodrich and Sam Schoenholz and post-doc Dan Sussman were a great source of information on various

Soft Matter physics topics. John Crocker provided insight that was key to solving a number of problems I came across in my experiments. Millicent Minnick took care of much of the red tape and bureaucratic business for me, and I really appreciate that she took on this workload so I could focus on my research and school work. It was also always fun to just pop into Millicent's office and chat for a bit.

I was lucky to amass a great group of friends during my graduate career. Austin Joyce, Mitch Lerner, Chris Lester, Sarah Clark, Jamie Lemon, Elio Angile, Joe Majkut, Stephanie "Madgeman" Feldman Majkut, and Kaitlin Miller made life outside of lab a ton of fun, and I always looked forward to our Sunday Asian Dinners. Cristina Resczenski was so amazingly gracious and supportive, and is, and forever will be, my ice cream buddy. My weekly lunches with Mike Turk helped keep me sane and he was a great source of support. The bromance between Paul Rubin and I is something not even Jane Austen could put into words.

Finally, I want to thank a group of people that in all likelihood will never see this thesis. While I have never met, and will probably never meet, Bill Burr, Bill Simmons, Pete Holmes, Chris Hardwick, Zach Lowe, Marc Maron, Paul Scheer, Jason Mantzoukas, June Diane Raphael, and Aisha Tyler, I want to thank them for putting on the best podcasts. Listening to their podcasts got me through many an experiment and many a late night of writing. Thank you for keeping me entertained.

ABSTRACT

HARD, SOFT, AND STICKY SPHERES FOR DYNAMICAL STUDIES OF DISORDERED COLLOIDAL PACKINGS

Matthew Daniel Gratale

Arjun G. Yodh

This thesis describes experiments which explore the role of interparticle interactions as a means to alter, and control, the properties of dense colloidal packings.

The first set of experiments studied phonon modes in two-dimensional colloidal crystals composed of soft microgel particles with hard polystyrene particle dopants distributed randomly on the triangular lattice. By mixing hard and soft spheres we obtain close-packed lattices of spheres with random bond strength disorder, *i.e.*, the effective springs coupling nearest-neighbors are either very stiff, very soft, or of intermediate stiffness. Video microscopy, particle tracking, and covariance matrix techniques are employed to derive the phonon modes of the corresponding "shadow" crystals, thereby enabling us to study how bond strength disorder affects vibrational properties. Hard and soft particles participate equally in low frequency phonon modes, and the samples exhibit Debye-like density of states behavior characteristic of crystals at low frequency. For mid- and high-frequency phonons, the relative participation of hard versus soft particles in each mode is found to vary systematically with dopant concentration.

The second set of experiments investigated depletion interaction potentials between micron-size colloidal particles induced by nanometer-scale micelles composed of the surfactant hexaethylene glycol monododecyl ether ($C_{12}E_6$). The strength and range of the depletion interaction is revealed to arise from variations in shape anisotropy of the rod-like surfactant micelles. This shape anisotropy increases with increasing sample temperature. By fitting the colloidal interaction potentials to theoretical models, we extract the rod-like micelle length and shape anisotropy as a function of temperature. This work introduces micelle shape anisotropy as a means to control interparticle interactions in colloidal suspensions, and shows how interparticle depletion potentials of micron-scale objects can be employed to probe the shape and size of surrounding macromolecules at the nano-scale.

The third set of experiments explored variation in the vibrational properties of colloidal glasses induced by changes in interparticle interactions. In particular, we study the vibrational phonons of quasi-2D colloidal glasses whose interparticle interactions are controlled via the temperature tunable depletion interaction described in the aforementioned experimental work. This tunable attraction enables us to study the changes in the properties of a colloidal glass as the interparticle attraction strength is gradually increased from weak (nearly hard-sphere) to strong. We observed that particle dynamics slow monotonically with increasing attraction strength and eventually plateau at very high attraction strength. The shape of the phonon density of states is also revealed to change with increasing attraction strength; specifically, glasses with low interparticle attraction strength exhibit comparatively more low frequency modes than glasses with high interparticle attraction strength.

Contents

List of Figures

Chapter 1

Introduction

Colloids have proven to be a fundamentally interesting material in condensed matter physics with incredible spin-off applications. A well-known colloid is milk, which consists of fluid drops of oily material suspended in another fluid, water. However, the more traditional colloidal suspension consists of solid particles suspended in a fluid. The particles can range in size from a few nanometers to tens of microns. Common examples of such colloids include ink, blood, and paint. Micron-sized solid polystyrene and silica particles suspended in a fluid such as water are among the most common colloids in physics. These colloids are interesting because they are small enough to experience Brownian motion, yet large enough to be easily observed by optical microscopy [6] (see Figure 1.1a for a sample microscope image of colloids in water). The properties of such colloidal suspensions are thus thermal, like atomic and molecular systems, but unlike atoms the motions of constituent particles can be observed in real-time. Thanks to these traits, colloidal particles provide excellent models for traditional atomic and molecular systems [7,8]. For these reason, colloidal experiments have often provided insight about both the

microscopic and the macroscopic properties of all kinds of materials [9–11]. Of course, colloids are interesting soft materials in their own right; they offer a starting point for understanding pastes, inks, paints, cosmetics, food and more. Arguably, the key ingredient of the colloidal suspension is the interparticle interaction. Other particle properties are important, *e.g.*, shape [12–17]. Interparticle interactions and arrangement geometry ultimately determine the structures that form and the properties of those structures [18–24].

In many colloidal experiments, the interaction between the constituent particles is like a hard-sphere. In a hard-sphere system, particles experience no interaction except at contact; at contact, they experience an infinite potential wall (see Figure 1.1c). Ideal hard-sphere particles are incompressible, and the free energy of hard-sphere systems is solely a function of the systems' entropy [25–28]. However, not all systems, and indeed not all colloids, can be described with hard-sphere models. Various other forms of interparticle interaction potentials have been developed (or arise naturally) for colloids, and these interactions have subsequently been utilized to explore a rich phase space of behaviors beyond that of the hard-sphere systems.

Perhaps the second most commonly studied interaction between colloidal particles is the attractive interaction. In this case, a potential well is present in the interparticle potential (see an example of depletion attraction potential in Figure 1.1d). Depending on the well depth, the spheres become more (or less) sticky. The use of sticky spheres provides a means for the colloidal systems to model other features of traditional atomic and molecular materials. Perhaps, more importantly, they enable the creation of new soft materials such as colloidal gels [4, 29–31], and they can drive new phenomena such as re-entrance in colloidal glasses [29–34]. Attraction between colloidal particles can also provide a means for assembly in colloidal systems [18, 35–46].

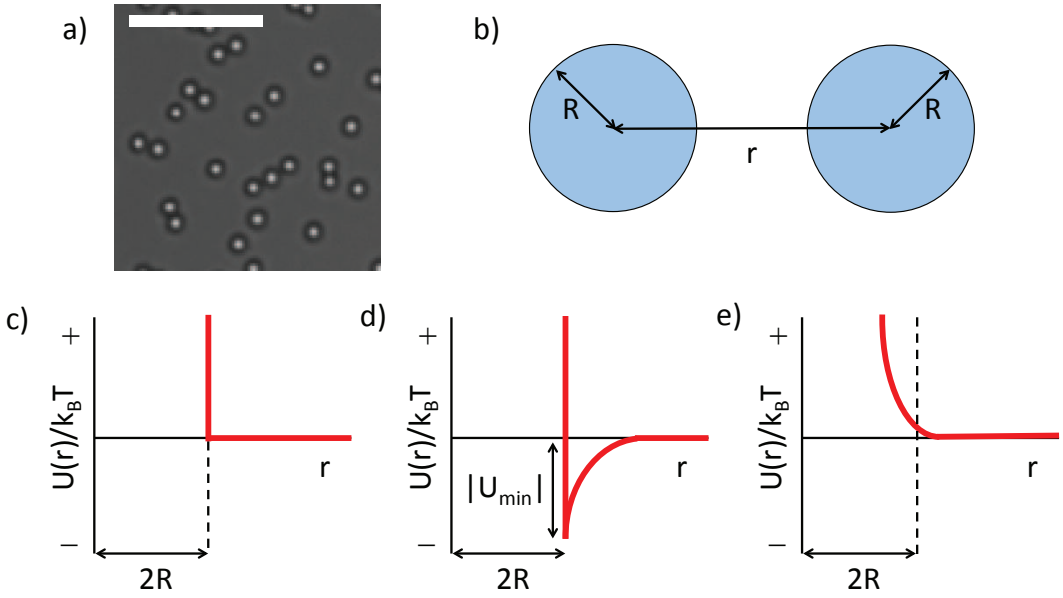

Figure 1.1: a) Experimental image of colloidal particles (polystyrene, diameter $= 1.5\ \mu$m). Scale bar is $10\ \mu$m. b) Cartoon schematic of two colloidal particles of radius R separated by a center-to-center distance r. c) The classic hard-sphere potential. No interaction arises between particle until contact ($r = 2R$), wherein interaction potential jumps from 0 to infinity. Spheres cannot overlap or be compressed. d) An example of an attractive interparticle potential. This example is closely akin to the entropic depletion interaction, which will be discussed at length later in this thesis. The strength of the attraction is related to the depth of the potential well, *i.e.*, $|U_{min}|$. e) Schematic of the potential between two soft spheres. In this case, particles can be compressed.

A third type of colloid/colloidal-interaction derives from so-called "soft-spheres" wherein the constituent particles can be compressed, and this compressibility leads to a soft sphere repulsive interaction potential at short range (see Figure 1.1e). Experiments with colloids composed of these kinds of particles expose, among other things, connections between particle stiffness and colloid rheological properties (especially at high volume fraction) [23, 24]. Other experiments suggest that the particle softness can qualitatively affect the phase behavior of suspensions [47]; specifically, this work observed that crystallization could be frustrated as particles were made "softer".

In this thesis I will discuss experiments which explore the role of interparticle interactions

as a means to alter, and control, the properties of dense colloidal packings. The experiments investigate how adding or altering the three interactions discussed above (hard-sphere, soft-sphere and attractive) affect the bulk behavior of colloidal systems. Specifically, in one set of experiments we studied the vibrational behavior of colloidal crystals consisting of both soft-spheres and hard-spheres on an ordered lattice [48]. In another set of experiments, we developed and were able to understand how a tunable depletion attraction is induced between micron-size particles via changes in the shape of surfactant micelles (*i.e.*, micelles that are suspended along with the particles in water). Another set of experiments explored the consequences of varying the strength of this attraction in colloidal glasses; in particular, changes in the vibrational phonon behavior of the colloidal glasses are studied as a function of increasing/decreasing interparticle attraction.

In addition to the work above, during my time at Penn I have also had the pleasure of contributin (as a co-author) to a variety of other interesting colloidal experiments. In one paper, we investigated how particle shape influences the bending rigidity of colloidal monolayer membranes [49]. In another paper, we explored the relationship between the number of nearest neighbors and the vibrational phonon spectra of colloidal glass clusters [50]. In a third paper, we probed the vibrational signatures of the cross-over from dense glassy to sparse gel-like colloidal packings [4]. In a fourth paper, we assembled 2-dimensional colloidal particle arrays on nematic liquid crystal interfaces [1], and we studied the particle dynamics. The remainder of this chapter will provide a brief introduction to each of the primary projects to be discussed in this thesis. An outline of the thesis organization is also provided.

1.1 Soft-sphere Colloidal Crystals with Hard-sphere Dopants

The macroscopic behavior of disordered (glassy) materials generally differ from their (ordered) crystalline counterparts [11, 51–53], and the search for the microscopic origins of these differences is a fascinating and ongoing pursuit [54–61]. Recently, a number of studies have observed significant differences between the vibrational behavior of glasses and crystals, differences that are primarily apparent at low frequencies. Specifically, crystals follow the Debye model at low frequencies, where their Density of States ($DOS(\omega)$) grows as the frequency ω to the power of the dimension (d) minus one, *i.e.* $DOS(\omega) \sim \omega^{d-1}$. In disordered glasses, the $DOS(\omega)$ grows faster than the Debye model predicts and exhibits an excess of low frequencies modes. This excess of modes is sometimes called the "Boson peak" [62]. Further, low frequency modes in crystals display long-wavelength behavior, usually in the form of plane waves, while in glasses they can have a quasi-localized nature that have been suggested to be correlated with structural rearrangements or soft spots [2, 63–69].

To date, the vast majority of studies of glasses have focused on systems wherein the microscopic constituents are *structurally* disordered. This approach is reasonable, since structurally disordered solids typically form from rapidly quenched atomic and molecular liquids [70, 71] and, in the case of colloids, from densely-packed rapidly loaded and/or polydisperse suspensions [2, 11, 26, 51, 72–80]. Structural disorder, however, is not the only kind of disorder present in nature. Disorder can also be introduced into a crystalline material, for example, via heterogeneous bonds (heterogeneous interactions) between constituent particles [81]. Interestingly, simulations and numerical studies suggest that similarities and differences exist between systems with pure structural disorder versus bond disorder [82–86], but experimental studies of such

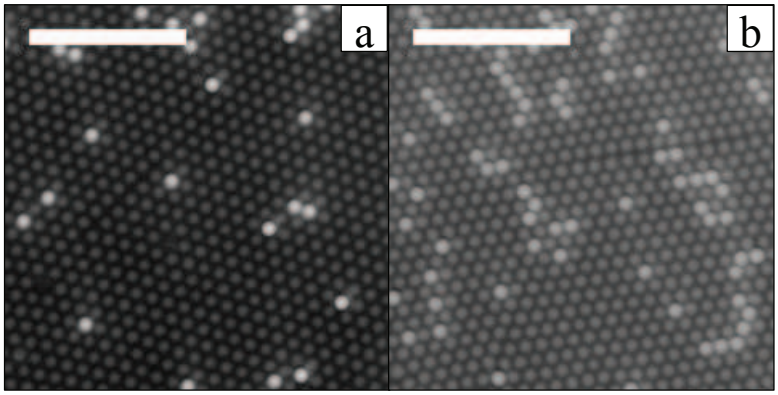

Figure 1.2: Images of a soft PNIPAM particle colloidal crystal doped with a) 2% and b) 11% hard polystyrene particles. The white spheres are polystyrene particles, and the grey spheres are PNIPAM particles. Scale bars are 10 μm.

systems are lacking. Further, most studies have investigated bulk (material) properties like the shape of the DOS, but little is known about the behavior of individual particles which make up such systems. Thus, experiments that derive information about individual particle motions can provide complementary insights and can help to elucidate similarities and differences between structurally disordered versus bond-interaction disordered systems.

Chapter 2 of this thesis discusses experiments which explore the role of bond disorder in crystals [48]. To accomplish this goal, crystals were created with two species of colloidal particles: "soft" PNIPAM microgel particles and "hard" polystyrene sphere dopants. Three types of bonds were thus present in the crystals due to the three possible interparticle combinations (hard-hard, soft-hard, soft-soft). In this way we created geometrically ordered colloidal crystals with bond heterogeneity. The number fractions of hard and soft particles were varied in an effort to control the amount of bond disorder. Particle trajectories were measured using standard video microscopy techniques [87], and the vibrational phonon modes were calculated using previously established covariance matrix methods [2, 73, 88–90].

From these experiments we learned (over the parameter space that we were able to explore) that regardless of number fraction of hard and soft particles, all crystals exhibited Debye behavior at low frequencies. Soft spheres dominated the motion of the intermediate frequency modes, and these modes had an extended character. The high frequency phonon modes were dominated by hard spheres and were highly localized. Numerically generated spring networks corroborated the experimental results and also enabled us to extrapolate to higher number fractions of hard spheres, which are currently not experimentally accessible.

1.2 Tuning Depletion Interactions: Variations with Depletant Shape

As part of our effort to study interaction potential effects in glasses, we developed a system for tuning attractive interactions in suspension. This work was interesting in its own right.

A well-known attraction arises between large colloidal particles when many small non-adsorbing particles, called depletants, are added to the suspension. This attractive force is entropic in origin and is often called the depletion force [91, 92]. Over the years, depletion forces have proved valuable as a means to control and study phase behavior [17, 29–34, 93–101], to direct self-assembly [18, 35–46, 102–104], and to control the stability of colloidal suspensions [105–118]. Depletion forces are also used in applications such as formulation and processing of food [119–122] and paint [123], and related entropic effects called macromolecular crowding are believed to play a role in cell biology [124, 125]. It is thus important to fully understand depletion phenomena and to continue to explore new means to induce and manipulate depletion forces.

In laboratory experiments, most depletants are spherical, but sometimes depletants with other

shapes are utilized, such as rods or disks [105, 106, 126–139]. The functional form and strength of the induced entropic potential depends on depletant shape. For example, at the same volume fraction, ρ, small rods of length L will induce a stronger attraction than small spheres with diameter L [126–128], and the spatial form of the potential induced by rods is steeper than that of spheres. In practice, it is often desirable to vary interaction strength and this task is usually accomplished by varying depletant volume fraction, *e.g.*, by adding more small particles into the suspension [17, 30–34, 42–44, 93, 97, 98, 102, 105, 107–109] or by changing the sphere radius *in situ* [36, 37, 46, 99–101, 104].

In my thesis work, we show how depletant shape anisotropy (*e.g.*, the length of rod-like surfactant micelles) can be employed to tune interparticle attractions. Briefly, for colloidal spheres of radius R in a suspension of smaller rods of length L ($2R >> L$) and cross-sectional diameter D, there exists a shell of thickness $L/2$ around the colloidal spheres that the center of the depletants cannot enter. This shell is referred to as the "excluded volume". When the excluded volumes of the two spheres overlap, a volume called the "overlap volume" is created. This overlap volume decreases the total excluded volume in the sample, and, in turn, increases the accesible free volume to the depletants. This situation is entropically favorable for the depletants, and thus an entropic force proportional to the overlap volume is induced between the two colloidal spheres by the depletants. When the rod length L increases, and cross-sectional diameter D and rod volume fraction ρ is held constant, the overlap volume increases, which increases the entropic force between colloidal spheres. Cartoon representations of the depletion interaction between colloids induced by rod-shaped depletants are presented in Figure 1.3.

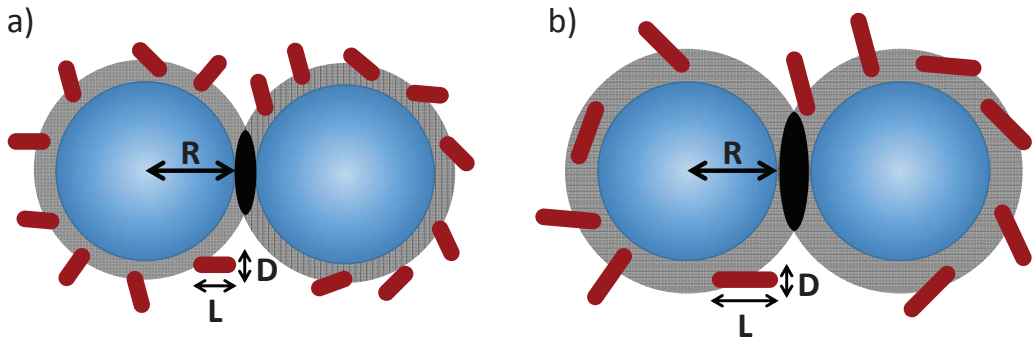

Figure 1.3: Depletion between colloidal particles of radius, R, in suspension of rods with length, L, and cross-sectional diameter, D. The rod centers cannot fit within regions of excluded volume (grey shaded region). a) When excluded volumes of two spheres overlap, the rod entropy increases in proportion to excluded volume overlap (black region), and an attractive force thus arises between colloidal particles. b) When rod length, L, is increased, while keeping rod volume fraction, ρ, and cross-sectional diameter, D, constant, then the excluded volume overlap increases, and the strength and range of the attraction between colloidal particles increases. Rods and colloidal particles not drawn to scale.

Chapter 3 of this thesis discusses experiments wherein depletion interactions between micron sized colloidal spheres are controlled by tuning the shape anisotropy of the nano-scale depletants. In the process, the work introduces depletion interaction measurements of micron-scale objects as a new method to extract information about the size and shape of surrounding macromolecules at the nano-scale. Specifically, temperature-dependent interparticle interaction potentials are derived from video microscopy measurements of the pair correlation function of micron-sized silica spheres suspended in the presence of hexaethylene glycol monododecyl ether ($C_{12}E_6$) surfactant micelles. The length and shape anisotropy of the micelles, as a function of temperature, were extracted by fitting the measured interaction potentials to existing theoretical models for the depletion forces of rod-like/ellipsoidal depletants [131].

We found that the measured depletion potentials vary substantially in magnitude and range

with temperature. Specifically, both the potential well depth and its range increase with increasing temperature. These effects arise from shape anisotropy variation, wherein nearly spherical $C_{12}E_6$ micelles at low temperatures evolve into cylindrical micelles of varying length at higher temperatures. The resultant derived dimensions of suspended micelles are found to be roughly consistent with small angle neutron scattering (SANS) data for $C_{12}E_6$ [3]. To our knowledge this is the first experiment to explicitly demonstrate temperature tuning of shape anisotropy as a means to modulate the depletion interaction.

1.3 Effects of Interparticle Attraction Strength in Disordered Colloidal Packings

The glass transition is considered by many to be one of the greatest challenges in condensed matter physics [140]. To date, much of the experimental, theoretical and simulation work studying glasses have focused on systems containing hard-spheres [10, 11]. More recently, however, studies have observed that many properties of glasses depend on the details of the underlying interparticle interactions [141–145].

At least two kinds of disordered packings are found at high packing fraction, ϕ; they depend on the strength of the interparticle attraction (see Fig. 1.4 for a cartoon representation of the currently accepted state diagram). In "repulsive glasses", the interparticle attraction strength is weak (or zero), and in "attractive glasses" the interparticle attraction strength is strong. Perhaps the biggest difference observed thus far between repulsive glasses and attractive glasses concerns particle dynamics. Particle dynamics have been observed to be slower in attractive glasses than in repulsive glasses [17, 19, 30, 32–34, 146]. It has also been observed in attractive glasses that

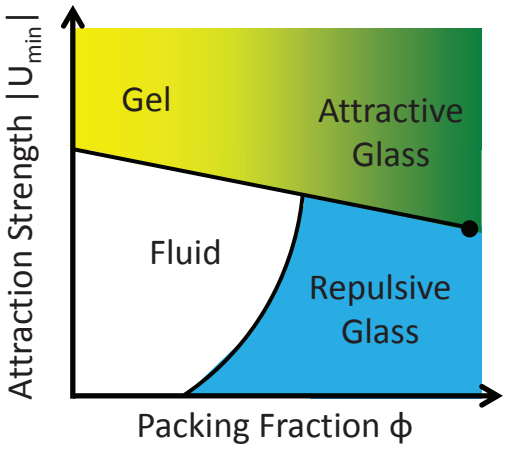

Figure 1.4: Qualitative state diagram for disordered glassy packings as a function of packing fraction ϕ and interparticle attraction strength $|U_{min}|$.

particle dynamics are heterogeneous over a wider range of time and length scales compared to repulsive glasses [146]. Additionally, the cooperative rearrangement regions (CRRs) are string-like in repulsive glasses, while in attractive glasses they are compact and involve more particles than the repulsive systems [146].

While previous research has uncovered these differences between particular repulsive and attractive glasses, much less work has been done to elucidate the transition from a repulsive glass to an attractive glass. For example, it is not known whether such a transition is gradual or discontinuous. Additionally, the mechanisms at the microscale which vary as the transition is approached and crossed have not been worked out. Experiments studying the transition from the repulsive glass state to the attractive glass state could help advance the currently accepted mode-coupling theory describing such systems, or potentially encourage the development of a new framework with which to describe glassy systems, and could thus lead to a better understanding of the glass transition. Furthermore, understanding the changes in glasses induced by changes in

the interparticle bonds could help derive methods to control the properties of glasses.

Chapter 4 of this thesis discusses experiments that begin to explore the transition from the repulsive to the attractive glass state. Dense packings of a binary colloidal suspension in a solution of $C_{12}E_6$ surfactant micelles enable us to study colloidal glasses as a function of the strength of interparticle attraction. The two sizes of colloidal particles frustrate crystallization, creating a disordered colloidal glass. The use of $C_{12}E_6$ surfactant micelles as depletants, as discussed above and in **Chapter 3**, allowed us to vary the attraction strength between colloidal particles. We were thus able to gradually increase the interparticle interaction of a colloidal glass from weakly attractive to strongly attractive, and concurrently study how the vibrational properties of colloidal glasses change with changes in interparticle attraction.

Our initial results show that particle dynamics slow monotonically with increasing attraction strength and saturate when the interparticle attraction strength becomes sufficiently strong. The shape of the vibrational density of states also changes with increasing attraction strength. Specifically, repulsive glasses have comparatively more low frequency modes than attractive glasses. Further, the low frequency phonon modes in attractive glasses were observed to be spatially extended, whereas the motion was found to be more quasi-localized in repulsive glasses. These changes in the vibrational and dynamical behavior signify the transition from the repulsive glass state to the attractive glass state.

1.4 Organization of Thesis

The remainder of this thesis is organized as follows. **Chapter 2** will present published results on the vibrational phonons of two-dimensional soft-particle colloidal crystals with hard-particle

dopants, *i.e.,* with bond-strength disorder [48]. **Chapter 3** will present results that have been submitted for publication which elucidate the change in depletion attraction between colloidal particles induced by changes in the shape of surfactant micelle depletants. **Chapter 4** will present initial work on the behavior of colloidal glasses induced by changes in interparticle attraction strength. **Chapter 5** summarizes the results presented in the previous chapters and proposes ideas for future study.

Chapter 2

Phonons in Two-Dimensional Colloidal Crystals with Bond Strength Disorder

2.1 Introduction

The search for the microscopic origins of the differences between disordered (glassy) materials and their (ordered) crystalline counterparts is an interesting and ongoing enterprise [54–61]. A variety of disordered solids, ranging from metallic to colloidal glasses, have been found to exhibit similar vibrational properties [147–156]. Thus far, most of this research has focused on materials wherein the microscopic constituents are *structurally* disordered; these states of matter typically form from rapidly quenched atomic and molecular liquids [70, 71] and, in the case of colloids, from rapidly loaded densely-packed and/or polydisperse suspensions [2, 11, 26, 51, 72–80].

However, other kinds of disorder are present in nature. For example, disorder can be introduced into a crystalline material via heterogenous interparticle interactions or, alternatively,

heterogeneity in the bonding between constituent particles [81]. Simulations and numerical studies suggest that similarities and differences exist between systems with pure structural disorder versus bond disorder [82–86], but experimental studies of such systems are lacking. The simulations and numerical studies carried out thus far have primarily focused on the shape of the phonon density of states, often in search for insights into the origin of the boson peak. However, little is known about the concomitant behavior of individual particles that make up such systems.

In this chapter, we experimentally investigate the vibrational behavior of two-dimensional (2D) colloidal crystals with bond-strength disorder. These colloidal crystals are composed primarily of "soft" poly(N-isopropylacrylamide) (PNIPAM) microgel particles, with "hard" polystyrene (PS) particle dopants distributed randomly on the lattice. Thus, we study 2D structurally ordered lattices with a distribution of bond strengths; nearest-neighbor bonds are either very stiff, very soft, or of intermediate stiffness. Video microscopy is employed to track the motion of all particles, and particle displacement covariances are used to derive the phonon modes of the corresponding "shadow" crystals with the same geometric configuration and interactions as the experimental colloidal system, but absent damping. Thus, we explore phonon modes in crystals with bond strength disorder as a function of increasing dopant concentration, and, among other things, we ask whether it is possible to create a geometrically ordered solid with bond-strength disorder whose phonons do not follow the Debye model at low frequencies. The bulk of the work discussed in this chapter has been published [48].

2.2 Contextual and Theoretical Background

2.2.1 Low-frequency Phonon Behavior of Ordered Crystalline Solids: The Debye Model

The Debye model is the traditional theory employed to describe the vibrational phonon modes in solid materials. In the Debye model the low frequency phonon modes are described as plane waves with a dispersion relations $\omega = c\,\vec{k}$; here ω is the phonon frequency of a given mode, $\vec{k}$ is its wavevector, and c is the speed of sound. The density of states ($DOS(\omega)$) is defined as the number of modes in the frequency interval $[\omega, \omega + d\omega]$.

In crystals, constituent particles are arranged in a periodic array, *i.e.*, the crystal lattice. Given this periodic array of particles, the Debye model assumes evenly spaced modes in k-space. Thus, the number of modes for each frequency ω is proportional to the area of a surface with constant (corresponding) $\vec{k}$. Following this model for a d-dimensional solid, the density of states is proportional to phonon frequency to the power $d-1$, *i.e.*,$DOS \propto \omega^{d-1}$. The Debye model has proven to accurately predict the low frequency phonon behavior of many solids. For example, the Debye model accurately predicts the contributions of the phonons to the temperature, T, dependence of the specific heat, C_V, of crystalline solids at low temperatures: $C_V \propto T^3$.

2.2.2 Low-frequency Phonon Behavior of Disordered Solids

While the behavior of ordered crystalline solids at low frequencies is accurately predicted by the Debye model, the behavior of disordered glassy materials is different from their crystalline counterparts and is not captured by the Debye model. Specifically, an excess of low-frequency vibrational modes can exist in disordered solids compared to what is predicted by the Debye

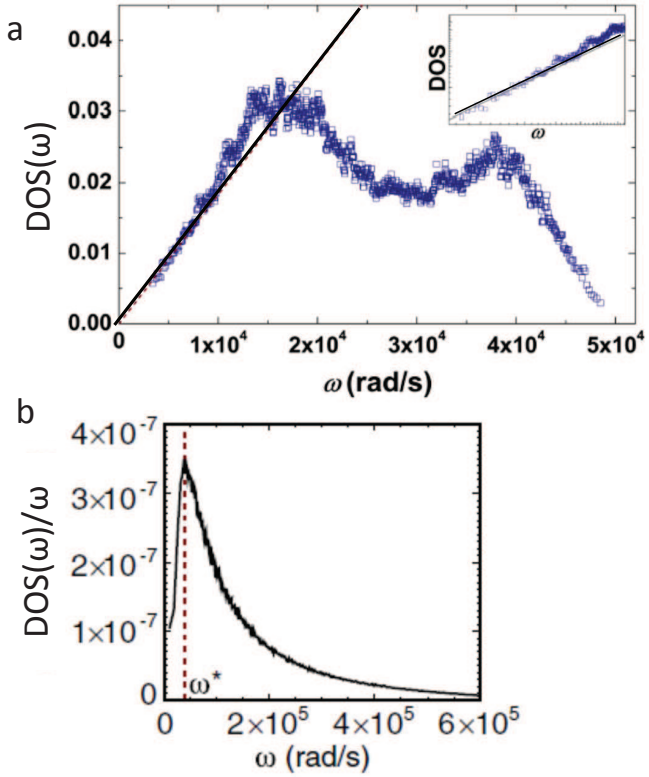

Figure 2.1: a) $DOS(\omega)$ for a 2D colloidal crystal at a liquid crystal-air interface reported in ref. [1]. Black line represents Debye prediction for 2D system, $DOS(\omega) \sim \omega$. Inset focuses on low frequency regime. Note this inset is in log-log scale with a slope equal to 1. Observe $DOS(\omega)$ follows Debye prediction at low frequencies. b) Density of states scaled by Debye predictions, $DOS(\omega)/\omega$, for a 2D colloidal glass reported in ref. [2]. The location of the Boson peak is represented by ω^*.

model [62]. This effect is visualized by scaling the $DOS(\omega)$curve by ω^{d-1} (the expected Debye behavior), *i.e.*, $DOS(\omega)/\omega^{d-1}$. For crystals, $DOS(\omega)/\omega^{d-1}$ is a constant at low-frequencies (see Figure 2.1a). For glasses, a "bump" is observed at low-frequencies (Figure 2.1b). This bump is commonly referred to as the "Boson peak". Along with this excess of modes at low frequencies, the modes at low-frequencies were found to be quasi-localized and display enhanced participation in regions prone to rearrangements [2, 63–69].

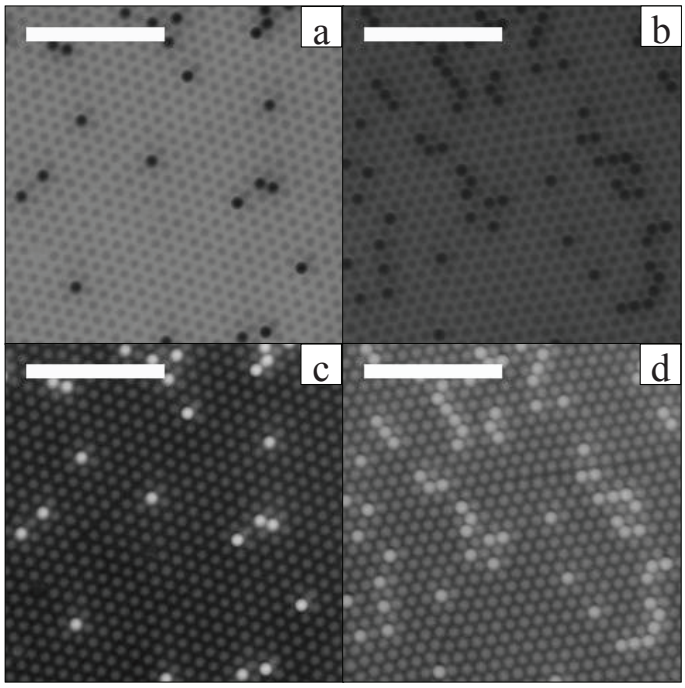

Figure 2.2: Raw images of a soft PNIPAM particle colloidal crystal doped with a) 2% and b) 11% hard polystyrene (PS) particles. c) and d) Inverted images of a) and b), respectively. In a) and b) the black spheres are PS particles, and the grey spheres are PNIPAM particles. In c) and d) the white spheres are PS particles, and the grey spheres are PNIPAM particles. Scale bars are 10 μm.

2.3 Experimental and Analytical Methods

2.3.1 Sample Preparation and Imaging

My experiments employed ensembles of particles sandwiched between a glass slide and cover slip (Fisher Scientific), creating a quasi-2D chamber. Polystyrene (PS) particles (Invitrogen) had a diameter of 1.1 μm and the poly(N-isopropylacrylamide) (PNIPAM) particles [157] had

a diameter of $\sim$1.1 μm. Because of this similarity in size, the particle mixture readily self-assembled into a triangular crystal. PNIPAM particles have a soft interparticle potential [158], while polystyrene particles are much more hard-sphere-like [27, 28, 146]. Since two different species of particles are employed, *i.e.*, soft PNIPAM and hard polystyrene, three different interparticle interaction combinations arise (soft-soft, soft-hard, and hard-hard). A small amount of Fluorescein dye ($\sim 0.2\%$ w/v, Sigma-Aldrich) was added to the aqueous suspension of particles in order to improve imaging contrast. The dye was excited using light from a mercury lamp that was directed through a 488 nm wavelength bandpass filter; the resulting video images consisted of dark particles on a bright background. Sample images are shown in Fig. 2.2a-b.

We thus create crystals with three distinct interparticle potentials distributed randomly on the triangular lattice. Particle motion was recorded using video microscopy, while the samples were kept at a temperature of $25\ ^{\circ}C$ using an objective heater (Bioptechs) connected to the microscope oil immersion objective. Video data of $N_{tot} \approx 1000 - 1500$ particles was recorded at a rate of 60 frames per second for 500 seconds. The raw images (dark particles on a bright background) were then inverted to yield images of bright particles on a dark background (Fig. 2.2c-d), and the motion of all particles was extracted using standard particle tracking techniques [87].

2.3.2 Vibrational Phonons Calculated from Particle Trajectories

We derive the vibrational properties using the displacement covariance matrix method. This state-of-the-art methodology has been described previously [2,73,88–90]. Here we measure $\mathbf{u}(t)$ the $2N_{tot}$-component vector of the displacements of all particles from their average positions $(\bar{x}, \bar{y})$. Then we compute the time-averaged displacement covariance matrix, $C_{ij} = \langle u_i(t) u_j(t) \rangle_t$ where $i, j = 1, ..., 2N_{tot}$ run over particles and positional coordinates, and the average runs over

time (*i.e.*, over all frames). In the harmonic approximation, the potential energy V of the system is given by:

$$V = \frac{1}{2}\mathbf{u}^T K \mathbf{u}, \tag{2.1}$$

where K is the matrix of effective spring constants between all pairs of particles, with each element defined as:

$$K_{ij} = \frac{\partial^2 V}{\partial u_i \partial u_j}. \tag{2.2}$$

The hamiltonian of the system is:

$$H = \frac{1}{2}\mathbf{u}^T K \mathbf{u} + \frac{\mathbf{p}^2}{2m}, \tag{2.3}$$

where $\mathbf{p}$ is the momentum vector for the system. Knowing the hamiltonian of the system provides us with the form of the system's partition function Z, which is:

$$Z \propto \int d\mathbf{u} d\mathbf{p}\, e^{-\beta(\frac{1}{2}\mathbf{u}^T K \mathbf{u} + \frac{\mathbf{p}^2}{2m})}, \tag{2.4}$$

where β is $\frac{1}{k_B T}$. With the partition function we can calculate the time-averaged displacement covariance matrix, $C_{ij} = \langle u_i(t) u_j(t) \rangle_t$. Using basic statistical mechanics, and the form of the partition function from equation 2.4, we find that:

$$\langle u_i(t) u_j(t) \rangle_t = \langle \int d\mathbf{u} d\mathbf{p}\, \mathbf{u}\mathbf{u}^T e^{-\beta(\frac{1}{2}\mathbf{u}^T K \mathbf{u} + \frac{\mathbf{p}^2}{2m})} \rangle_{ij} / Z. \tag{2.5}$$

Note that the integral over momentum space only involves the momentum term in the exponent, and so we can separate the momentum and position integrals, which we can also do for the

partition function Z, *i.e.,*:

$$\langle u_i(t)u_j(t)\rangle_t = \frac{\langle \int d\mathbf{p}\, e^{-\beta\frac{\mathbf{p}^2}{2m}} \int d\mathbf{u}\, \mathbf{u}\mathbf{u}^T e^{-\beta\frac{1}{2}\mathbf{u}^T K\mathbf{u}}\rangle_{ij}}{\int d\mathbf{p}\, e^{-\beta\frac{\mathbf{p}^2}{2m}} \int d\mathbf{u}\, e^{-\beta\frac{1}{2}\mathbf{u}^T K\mathbf{u}}}. \tag{2.6}$$

The momentum terms cancel here, and we are left with just the integral over the displacement phase space. Here we see that this measurement yields "static" information about the sample, *i.e.* only dependent upon the particle positions and the interparticle interactions.

Solution of the displacement Gaussian integrals reveals that the covariance matrix C is directly related to the stiffness matrix K by $(C^{-1})_{ij}k_BT = K_{ij}$. The experimental covariance data therefore gives the vibrational properties of the so-called "shadow" system; this "shadow" system of particles has the exact same static properties as our experimental system (*i.e.,* with the same covariance and stiffness matrices, C and K), but does not have the damping of our experimental system. The phonon eigenvectors and frequencies are derived from the dynamical matrix D, which is directly related to the stiffness matrix with $D_{ij} = K_{ij}/m_{ij}$, where $m_{ij} = \sqrt{m_i m_j}$ with m_i the mass of particle i. Diagonalizing the dynamical matrix gives the eigenvalues λ_i and eigenvectors $\mathbf{e}(\omega_i)$ of the shadow system phonons. The eigenvalues λ_i correspond to the phonon frequencies ω_i squared, *i.e.* $\lambda_i = \omega_i^2$, of the phonon modes, while the eigenvectors $\mathbf{e}(\omega)_i$ correspond to the particle amplitudes associated with each of the phonon modes. Again, we remind the reader that the displacement covariance and spring constant matrices, C and K, respectively, only depend on the static interactions between particles and the geometric configuration of the particles, both of which are the same for the real and shadow systems.

The accumulated mode number $N(\omega)$ is then derived from the calculated phonon modes. Note, $N(\omega)$ is defined as the number of modes with frequency less than or equal to ω. As stated

previously, the more commonly used phonon density of states $DOS(\omega)$ is defined as the number of modes per frequency interval $d\omega$, $DOS(\omega) = dN(\omega)/d\omega$. Thus, $N(\omega)$ is the integral of the $DOS(\omega)$ over the interval $d\omega$.

2.3.3 Corrections to Derive "True" Phonon Frequencies

Recently, it has been observed that the scheme described above to derive phonon eigenfrequencies is only truly correct when the ratio of (image) frames to degrees-of-freedom (number of modes) is very large. If the data is not sufficient to satisfy this criteria, then the "true" eigenfrequencies of the system are best found by linearly extrapolating the finite-frame data to an infinite number of frames [90, 159]. The phonon eigenfrequencies measured here were extracted using data derived from a finite number of frames. The total number of frames was approximately ten times the number of degrees of freedom in the system (*i.e.* twenty times the number of particles). Thus the phonon frequencies of each mode were corrected using data from three different numbers of image frames and then linearly extrapolating the data. Specifically, the inverse of the phonon frequencies, $1/\omega$, was plotted as a function of the ratio of the number of degrees of freedom to the number of frames. An infinite number of frames would give a ratio of zero. We then fit the three calculated frequencies to a straight line. The y-intercept of this fitted line is the inverse "true" frequency. Figure 2.3 presents a representative example of one such plot for the 10th mode of the 11% hard-particle crystal.

Figure 2.4 shows the experimental as well as extrapolated accumulated mode number $N(\omega)$ as a function of frequency ω for all samples. It is apparent from these plots that, while there was some change in the frequencies, the overall trends remained the same. The extrapolated "true" frequencies are reported herein, but we can confidently say that the number of frames used in

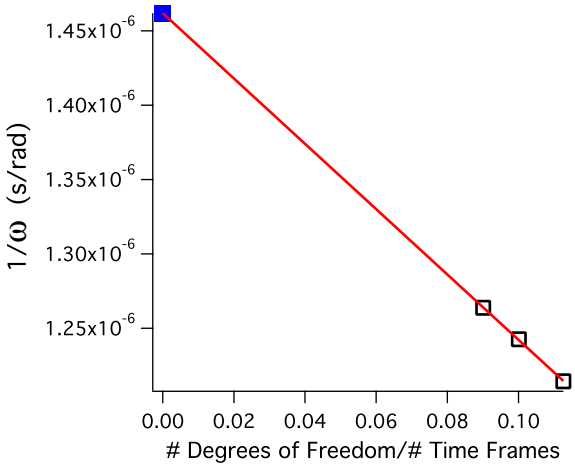

Figure 2.3: Hollow black squares are the inverse of the phonon frequency $1/\omega$ for the 10th mode of the 11% hard-particle crystal found using three different number of frames. Red line is the linear fit of the three points. Blue square is the "true" frequency extrapolated to infinite frames.

the experiments also provide a qualitatively accurate depiction of our system.

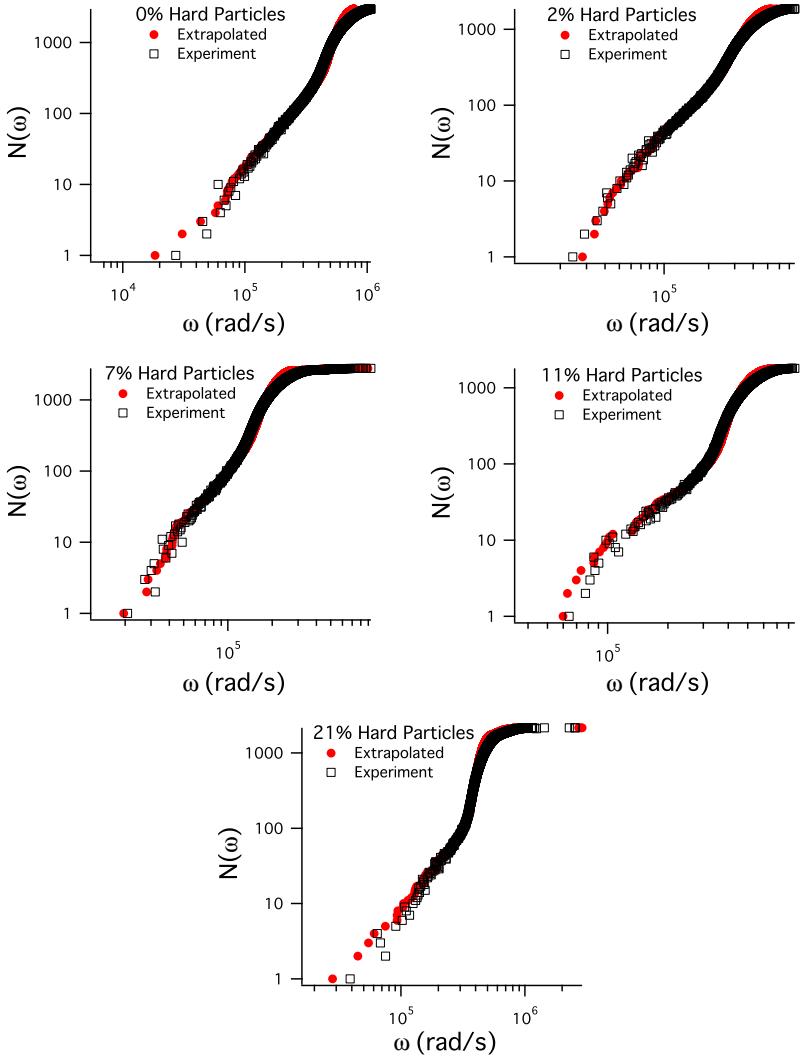

Figure 2.4: Accumulated mode number $N(\omega)$ as a function of frequency ω for all samples from experiments with (filled red circles) and without (hollow black squares) extrapolation correction.

2.4 Results and Discussion

2.4.1 Characterization of Crystal Structure

To characterize the triangular crystalline order of the samples, the orientational and translational correlation functions, $g_6(r)$ and $g_T(r)$, respectively, were computed for all of the crystals. $g_\alpha(r{=}|\mathbf{r}_i\text{-}\mathbf{r}_j|) = \langle\psi^*_{\alpha i}(r_i)\psi_{\alpha j}(r_j)\rangle$, where r_i and r_j are the positions of particles i and j, and $\alpha = 6, T$. ψ_{6i} and ψ_{6j} are the orientational order parameters for particles i and j, and ψ_{Ti} and ψ_{Tj} are the translation order parameters for particles i and j. The orientational and translational order parameters for a given particle j are defined as $\psi_{6j} = (\sum_{k=1}^{nn} e^{6i\theta_{jk}})/nn$, where θ_{jk} is the angle between particle j and its neighbor k and nn is the number of nearest neighbors. $\psi_{Tj} = e^{i\mathbf{G}\cdot\mathbf{r_j}}$, where $\mathbf{G}$ is a primary reciprocal lattice vector determined from the peak in the sample's 2D structure factor, $s(k)$.

In Fig. 2.5, the orientational correlation function $g_6(r)$ is large (> 0.8) at short distances and does not significantly decay over the longer distances probed; this observation suggests that all the samples possess good triangular order. The translational correlation functions for the 0%, 11%, and 21% hard-particle samples were found to exhibit excellent translational order (see Fig. 2.5), *i.e.*, $g_T(r)$ were large (> 0.8) at short distances and did not significantly decay at the longer distances probed. However, $g_T(r)$ decayed more rapidly at longer distances for the 2% and 7% hard-particle crystals. This decay is due to a single, large grain boundary that divided these particular samples into two well-ordered domains.

To confirm that these grain boundaries did not substantially affect the vibrational properties reported for these samples (*i.e.*, based on measurements over the full field of view), we calculated the phonon modes of the smaller (pristine) subsections, *i.e.*, the two grains with excellent

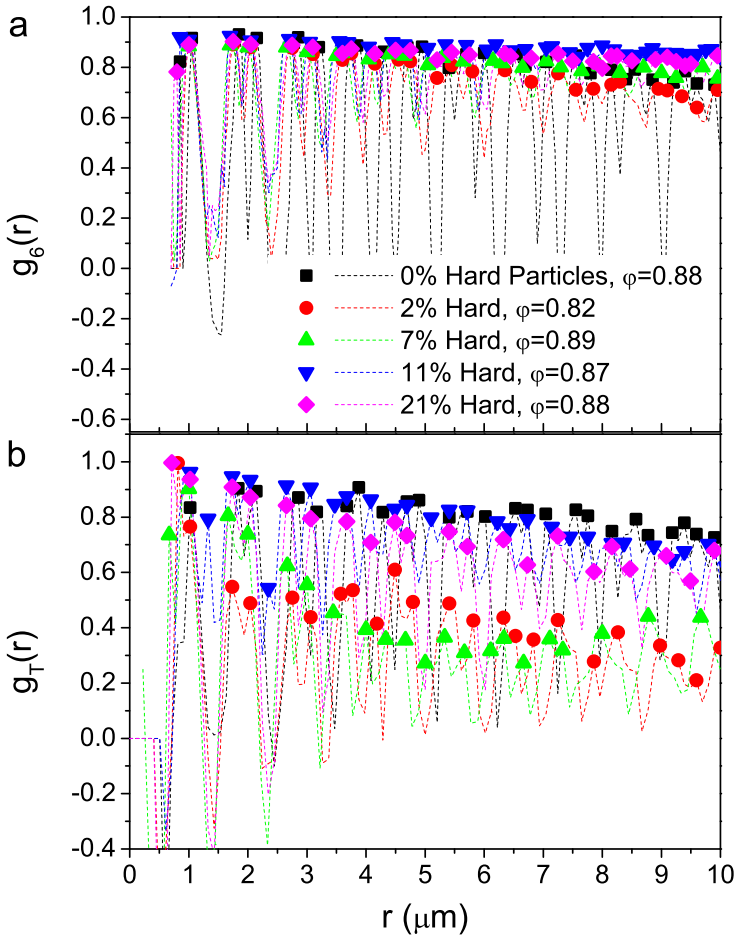

Figure 2.5: a) The orientational correlation functions, $g_6(r)$, and b) the translational correlation function, $g_T(r)$, of all crystals studied. Symbols represent local maxima and the dashed lines represent the full correlation function.

crystalline order, (Fig. 2.6). By comparing the basic trends for both fields-of-view, we confirmed that the presence of the grain boundary did not alter any of our primary conclusions. Specifically, since the number of particles is smaller in these subsections, the total number of modes is obviously smaller. Therefore, to fit data of the subsections onto the same plot as those of the full fields of view (labeled Full Field in Fig. 2.6), the accumulated mode number $N(\omega)$ was rescaled by the maximum accumulated mode number $N(\omega_{max})$. The participation fractions $P_F(\omega)$ and

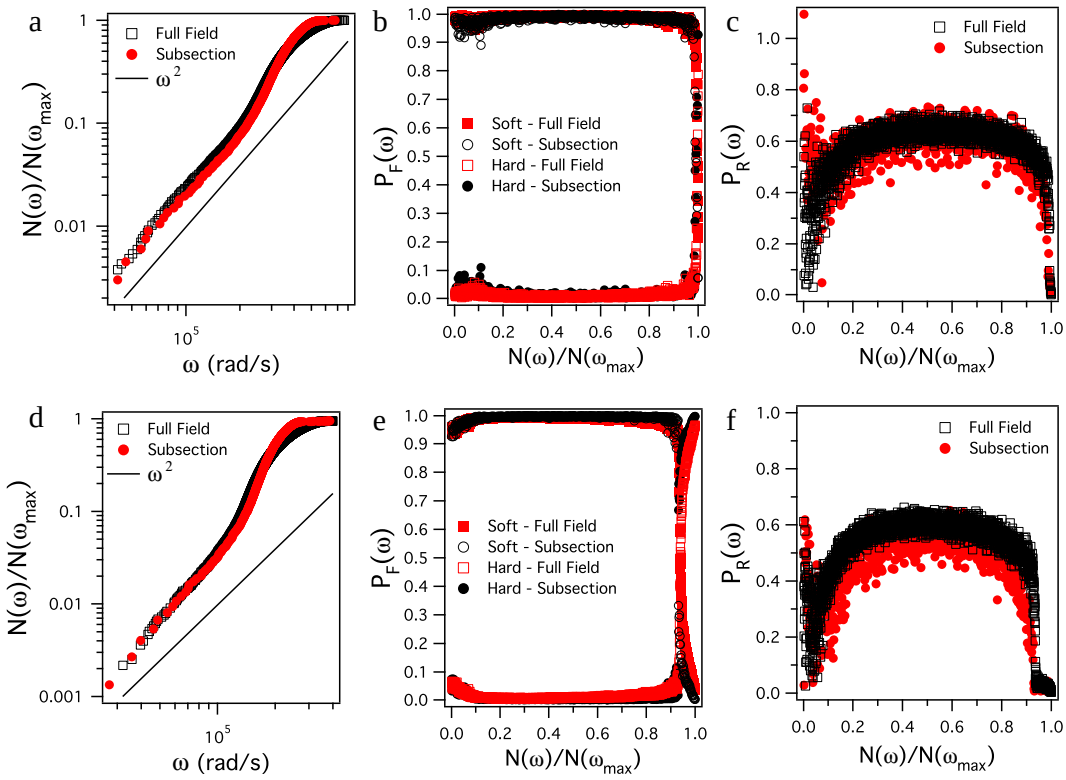

Figure 2.6: a-c) Data of full field of view and subsection of 2% hard-particle doped crystal. d-f) Data of full field of view and subsection of 7% hard-particle doped crystal. a) and d) Scaled accumulated mode number $N(\omega)/N(\omega_{max})$ as a function of frequency ω. Black line represents Debye model predictions (line is offset for clarity). b) and e) Participation fraction $P_F(\omega)$ as a function of scaled accumulated mode number $N(\omega)/N(\omega_{max})$. c) and f) Participation ratio as a function of scaled accumulated mode number $N(\omega)/N(\omega_{max})$.

participation ratios $P_R(\omega)$ in Fig. 2.6b-c and Fig. 2.6e-f are also plotted as a function of the accumulated mode number divided by the maximum accumulated mode number $N(\omega)/N(\omega_{max})$.

2.4.2 Particle Cluster Statistics

The spatial distribution of hard particle dopants in our experimental samples was not completely random, although the deviations from random distributions were relatively small. The origin of this effect is not entirely clear, but it could have arisen via aggregation effects during sample

loading. Nevertheless, to quantify the randomness we compared the measured distribution of hard-particle cluster sizes in our experiments to standard statistical predictions for random systems. The comparison indicates that the experiments have slightly more hard-particle clusters than predicted, especially at the lower dopant concentrations

By examining all possible configurations of two particle types on a hexagonal lattice, we were able to derive the probability $P(N)$ of a hard-particle being found in a cluster of N hard-particles. Given a hexagonal crystal with number fraction of hard spheres ϕ, the probability $P(N)$ of finding a hard sphere in clusters of $N = 1, 2, 3, 4, 5$ are:

$$P(1) = (1-\phi)^6 \tag{2.7}$$

$$P(2) = 6\phi(1-\phi)^8 \tag{2.8}$$

$$P(3) = 3\phi^2(1-\phi)^9[2 + 9(1-\phi)] \tag{2.9}$$

$$P(4) = 12\phi^3(1-\phi)^{10}[1 + 4(1-\phi) + 9(1-\phi)^2] \tag{2.10}$$

$$P(5) = 15\phi^4(1-\phi)^{11}[2 + 7(1-\phi) + 20(1-\phi)^2 + 31(1-\phi)^3]. \tag{2.11}$$

Figure 2.7 presents the theoretically derived probabilities for truly random systems compared to our experimental observations, as well as the results of computationally generated spring network distributions. We observe that the computationally generated spring networks line up with the theoretical probabilities. The experimental system with 21% hard particles follows the theoretical and computationally generated probabilities. However, for the experimental samples with 2%, 7%, and 11% hard particles, the probability of finding a hard particle in a cluster of

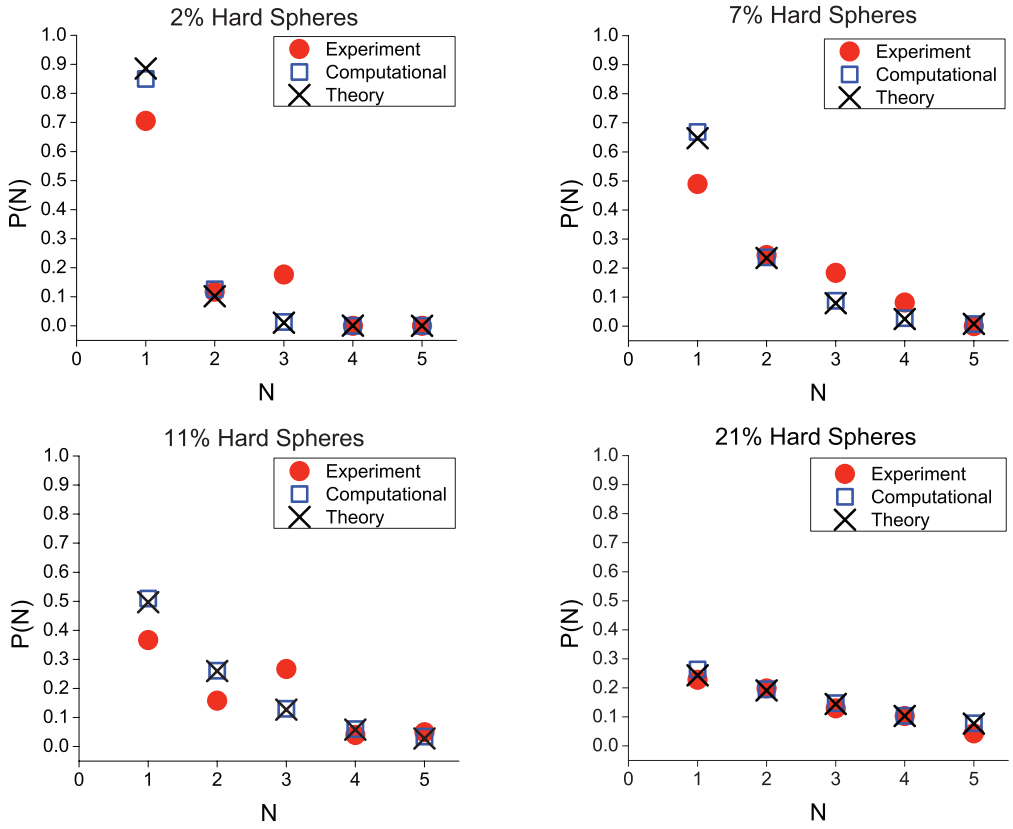

Figure 2.7: Probability $P(N)$ of finding a hard particle in a cluster of N hard particles from experiments (filled red circles), theoretical probabilities (black X's), and computationally generated spring networks (hollow blue squares).

$N > 1$ is higher in experiment than in theoretical and computationally generated predictions, though these deviations are not very large

We suspect that this clustering of hard particles arises from phase separation of hard and soft spheres during the sample preparation process. Phase separation between the hard and soft particles was observed at low packing fractions (see Fig. 2.8). During sample preparation, significant flow arises as the suspension of particles spreads throughout the sample chamber. It is at this time that phase separation begins; phase separation is arrested when the high packing fraction required for crystallization is obtained. Thus, slightly more clusters of hard particles are found

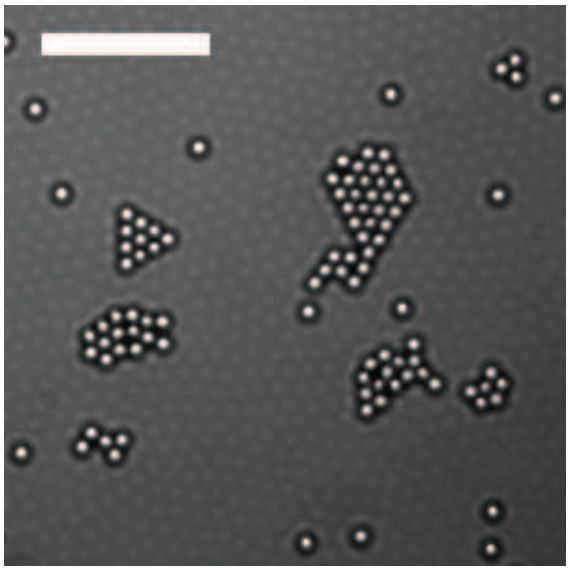

Figure 2.8: Phase separation between hard polystyrene spheres (white dots) and PNIPAM microgels (gray dots) at low packing fraction. Scale bar is 10 μm.

in our samples than predicted. Nevertheless, even with non-ideal circumstances (*i.e.*, not a truly perfect hexagonal lattice and not a truly random distribution of hard particles), all of our hard-particle doped soft-particle crystals displayed similar Debye-like behavior at low frequencies, soft particle dominated behavior at intermediate frequencies, and hard particle dominated high frequencies.

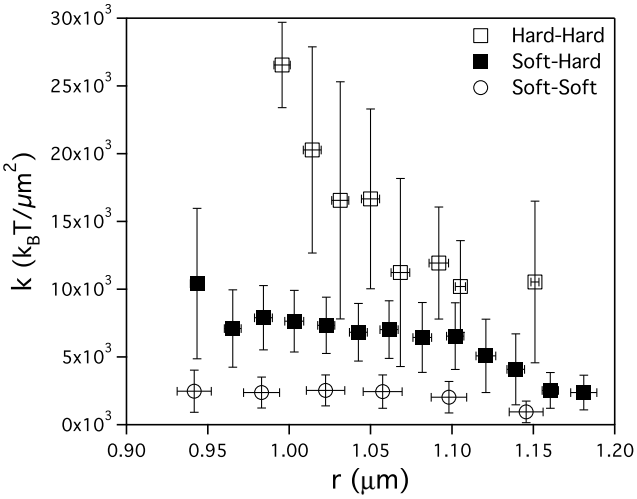

Figure 2.9: Effective spring constants k between two hard particles (hollow squares), two soft particles (circles), and hard-particle/soft-particle pairs (filled squares) derived from the computed spring constant matrix K as a function of average particle separation r for the 21% hard-particle doped crystal.

2.4.3 Spring Stiffness Heterogeneity

From the spring constant matrix K, it is apparent that three distinct nearest neighbor springs are present, corresponding to the three nearest neighbor particle combinations. Figure 2.9 shows the effective spring constants k as a function of the average particle seperation r measured in the 21% hard-particle crystal. Notice that hard-hard particle pairings have the stiffest springs, soft-soft particle pairings have the softest springs, and soft-hard particle pairings have springs with an intermediate stiffness.

2.4.4 Vibrational Phonon Behavior

For a 2D crystal, the Debye model predicts that the accumulated number of phonon modes, $N(\omega)$, should grow as the frequency-to-the-second-power (frequency-squared) in the low frequency regime [160]. In Fig. 2.10 the measured $N(\omega)$ is plotted for all doped crystals ($2\%, 7\%, 11\%, 21\%$

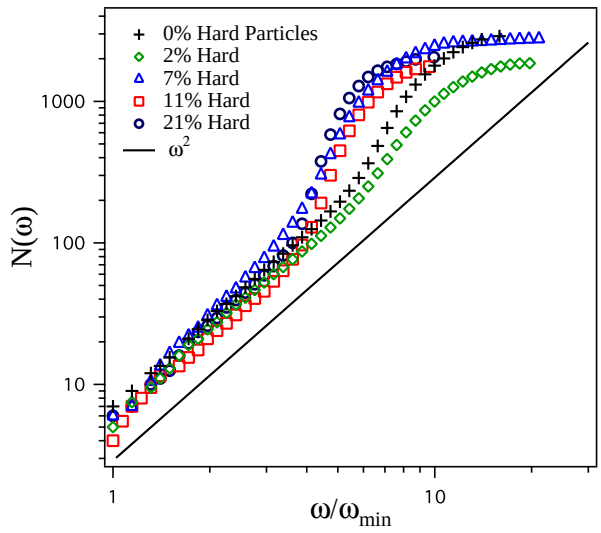

Figure 2.10: Accumulated mode number, $N(\omega)$, for all doped crystals and pure PNIPAM crystal as a function of the frequency ω scaled by the minimum frequency ω_{min} for each sample. The solid black line represents Debye law scaling, $N(\omega) \sim \omega^2$. The accumulated mode numbers are logarithmically binned.

PS/hard particles), as well as for a pure PNIPAM crystal (0% PS/hard particles). At low frequencies, $N(\omega)$ exhibits similar scaling with frequency in all crystals. This scaling is very close to the Debye model prediction. Thus, despite different degrees of bond strength disorder, the low frequency DOS behavior is quite similar to that of a perfect crystal (*i.e., a crystal with* 0% *dopant particles*).

At intermediate frequencies $N(\omega)$ grows faster than predictions of the Debye model, and at the highest frequencies, $N(\omega)$ plateaus. Note, a somewhat similar DOS behavior at low-intermediate frequencies was also observed by Kaya *et al.* [88]; in their paper, however, they derived the phonon information using two-dimensional slices within a three-dimensional colloidal crystal. They attributed this deviation from Debye behavior to a heterogeneous distribution of microgel particle stiffness and argued that the deviations were related to the boson peak. Without delving too deeply into the limitations (potential pitfalls) of their analysis approach [88],

we simply note that our low-frequency data does not support the existence of a boson peak in these systems. To better understand how crystalline behavior is preserved at low frequencies, as well as to elucidate the behaviors exhibited by these systems at higher frequencies, we utilize the derived eigenvectors of the present system to obtain spatial information about the phonon modes.

First, we quantify the contributions of soft and hard particles to each mode. This information is derived by calculating the participation fractions of each species for each mode. The eigenvectors of each mode have components (*i.e.*, associated displacement amplitudes) corresponding to each particle and each direction; for example, $\mathbf{e}(\omega) = (e_{1x}(\omega), ..., e_{N_{tot}x}(\omega), e_{1y}(\omega), ..., e_{N_{tot}y}(\omega))$, where N_{tot} is the total number of particles in the sample. Further, all eigenvectors are normalized such that $|\mathbf{e}(\omega)| = \sum_\alpha (e^2_{\alpha x}(\omega) + e^2_{\alpha y}(\omega)) = 1$, where α runs over all particles. The participation fraction for particle α in a mode with frequency ω is therefore given by $P_{F,\alpha}(\omega) = e^2_{\alpha x}(\omega) + e^2_{\alpha y}(\omega)$. Thus, the participation fraction of hard spheres in a mode with frequency ω is $P_{F,Hard} = \sum_h (e^2_{hx}(\omega) + e^2_{hy}(\omega))$, where h is the set of indices corresponding to hard spheres in the eigenvector. Similarly, the participation fraction of soft spheres is $P_{F,Soft}(\omega) = 1 - P_{F,Hard} = \sum_s (e^2_{sx}(\omega) + e^2_{sy}(\omega))$, where s is the set of indices corresponding to soft spheres in the eigenvector.

Second, we quantify the spatial extent of each mode by calculating its participation ratio. (Note, participation ratio and participation fraction have very different meanings; this vocabulary is unfortunate, but since the field has adopted it, we adopt it here too.) The mode participation ratio is defined as $P_R(\omega) = (\sum_\alpha e^2_{\alpha x}(\omega) + e^2_{\alpha y}(\omega))^2 / (N_{tot} \sum_\alpha e^4_{\alpha x}(\omega) + e^4_{\alpha y}(\omega))$. A low numerical value for the participation ratio indicates that the mode is spatially localized, while a

high value indicates the mode is spatially extended. The participation ratio cut-off used to separate localized from extended modes is typically set to be 0.2 [2, 4]. Modes with a participation ratio below (above) 0.2 are considered localized (extended).

The general behavior of the bond-disordered crystals can be gleaned from Fig. 2.11 wherein representative phonon modes of an 11% hard-particle-doped crystal are shown, along with the accumulated mode number, $N(\omega)$, the participation fraction, $P_F(\omega)$, and the participation ratio, $P_R(\omega)$. Interestingly, at low frequencies, where Debye-like behavior was observed in the accumulated mode number, the participation fractions of hard and soft particles follow their respective number fractions in the sample, *i.e.*, soft and hard particles participate equally (Fig. 2.11b). This representative mode and other modes at low frequencies, exhibits long-wavelength-like extended behavior; the behavior is similar to that of corresponding modes at low frequencies in perfect crystals. Note also that a few low frequency modes have very low participation ratios (*i.e.*, they have at least some quasi-localized character); we believe these effects are probably due lattice point defects and/or grain boundaries [161]. In the case of point defects, these low frequency modes appear to possess both long-wavelength-like character and localized motions near lattice defects. The mode shown in Fig. 2.11d is an example of one such mode (notice the defect in the lower left hand corner). Thus, though the participation ratio of such modes is typically below the expected participation ratio of extended modes (~ 0.5), they clearly exhibit a form of long-wavelength spatially extended behavior.

At intermediate frequencies, the accumulated mode number grows faster than would be expected had Debye scaling continued to higher frequencies. In addition, the motion in these modes is dominated by soft spheres. This effect is best quantified by the participation fraction.

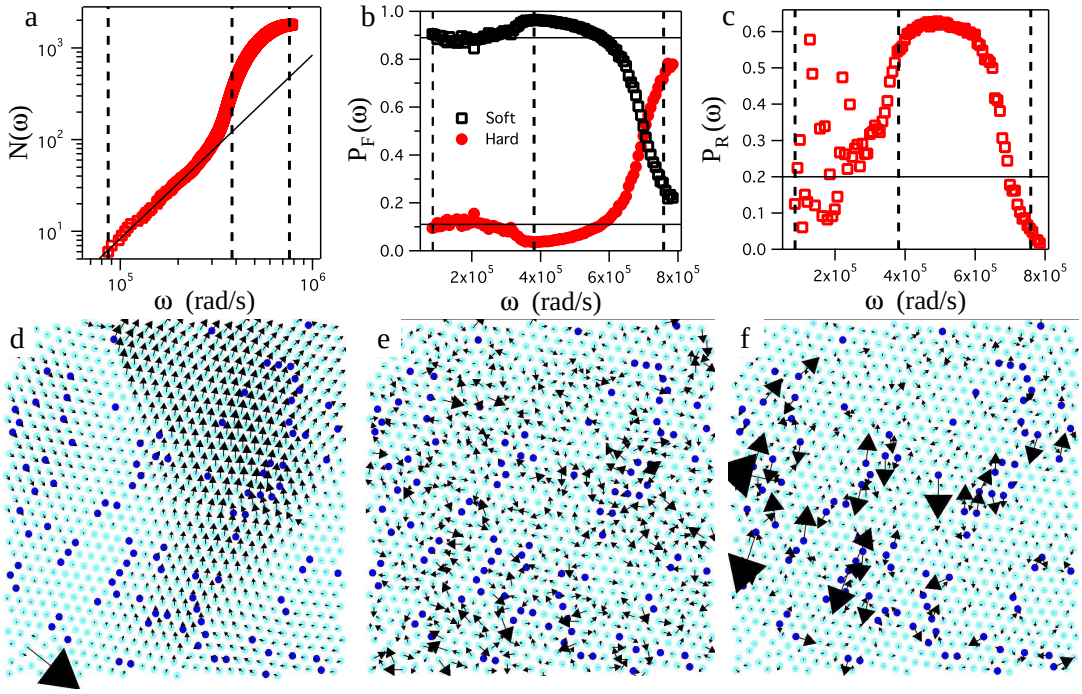

Figure 2.11: Mode characterization and representation for 11% hard-particle crystal. a) Accumulated mode number $N(\omega)$ with solid black line representing Debye law scaling, $N(\omega) \sim \omega^2$, and dotted black lines show where representative modes (d-f) are found on plot. b) Participation fraction $P_F(\omega)$ of hard (filled red circles) and soft (hollow black squares) spheres. Horizontal solid black lines show number fractions of soft and hard particles, 89% and 11% respectively, and dashed black lines again show representative modes. The participation fraction of hard and soft spheres is binned (i.e. averaged) over a bin size of 20×10^3 rad/s. c) Participation ratio $P_R(\omega)$ with solid black line showing threshold for localized versus extended motion, and dotted lines again show representative modes. The participation ratio of all particles is binned over a bin size of 20×10^3 rad/s. d-f) Vector displacement plots of representative modes d) $\omega = 86.4 \times 10^3$ rad/s, e) $\omega = 381.2 \times 10^3$ rad/s, and f) $\omega = 758.7 \times 10^3$ rad/s. Dark blue dots are hard particles, light blue are soft particles, and arrows are the particles' displacements. The larger the arrow, the larger the particle's displacement.

In particular, we see that the participation fraction of soft spheres in these modes is higher than the number ratio of soft spheres in the system (Fig. 2.11b). The motion of these intermediate modes is also spatially extended, but their character appears qualitatively different than was found at low frequencies.

The highest frequency modes are dominated by hard spheres. Specifically, a crossover in

the participation fraction is observed wherein hard particles have enhanced participation, and the participation of soft spheres is diminished. The highest frequency modes do not display long wavelength extended behavior; rather, they appear to be more localized than most of the modes observed at intermediate and low frequencies. This latter effect is supported quantitatively by the participation ratio (Fig. 2.11c). The participation ratio at intermediate frequencies is far above the 0.2 threshold. At high frequencies, however, the participation ratio drops below 0.2.

We next explore the effects of differing dopant concentrations. To better compare samples with different dopant concentrations, we scale the frequencies of each sample type by its mean frequency $\langle\omega\rangle$. In this manner, we can plot the behaviors of all samples over the same relative frequency range to discern trends more easily. Further, by subtracting the number fraction of hard spheres in a sample from the measured participation fraction, *i.e.*, $P_{F,Hard}(\omega) - N_{Hard}/N_{tot}$, we can suggestively plot all participation fraction versus frequency data as shown in Fig. 2.12. Here, when $P_{F,Hard}(\omega) - N_{Hard}/N_{tot}$ has a value of zero, then all particles participate equally (*i.e.*, corresponding to their number fraction in the sample); a negative value means there is diminished participation by the hard spheres and enhanced participation by the soft spheres; a positive value means enhanced participation by the hard spheres and diminished participation by the soft spheres. The three frequency regimes observed in the 11% hard particle crystals are apparent in all doped crystals when using this plotting scheme. Equal participation is observed at low frequencies, diminished hard particle participation at intermediate frequencies, and enhanced hard particle participation at high frequencies. In addition, we find that the extent (*i.e.*, frequency range) of the high frequency regime, wherein hard particles become the primary mode participants, shifts to lower relative frequency as the number of hard-particle dopants increases.

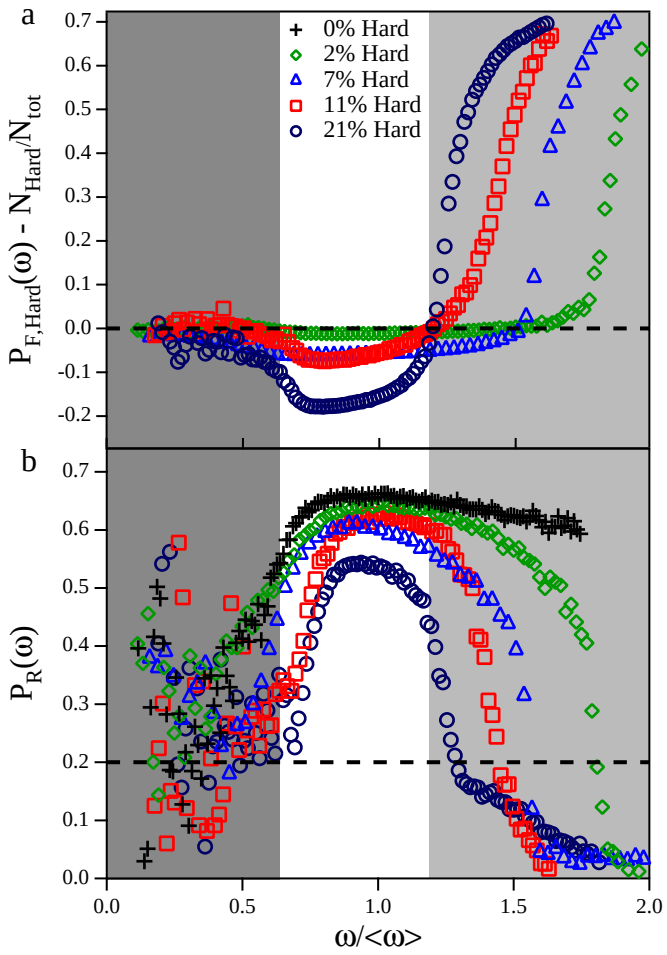

Figure 2.12: a) Hard-particle participation fractions shifted by hard-particle number fractions $P_{F,Hard}(\omega) - N_{Hard}/N_{tot}$ as a function of frequency scaled by the mean frequency $\omega/\langle\omega\rangle$ for all doped crystals. Dotted line represents equal participation. b) Participation ratio as a function of frequency scaled by the mean frequency $\omega/\langle\omega\rangle$ for all doped crystals as well as pure soft-particle crystal. Dotted line represents localized versus extended threshold. Legend is for both figures, however data for 0% hard-particle crystal only in Figure b. Both participation fraction and participation ratio data is binned (i.e. averaged) over a bin size of 20×10^3 rad/s. Note, the dark grey region represents the low frequency, equal participation regime, the white region represents the soft-sphere dominated, extended motion regime, and the light grey region represents the hard-particle dominated, localized motion regime.

The participation ratio of all doped crystals and the pure soft PNIPAM crystal are also shown in Fig. 2.12 as a function of scaled frequency. Notice that extended modes predominate at low and intermediate frequencies for all crystals, regardless of dopant concentration. The high

frequency modes in the pure soft particle crystal are also observed to be extended; however, the highest frequency modes of all doped crystals are found to be localized. Evidently, the hard particle dopants dominate motion at high frequencies, thus localizing vibrational motion since they are relatively isolated. This high frequency behavior appears similar to that observed in colloidal glasses [2, 153].

2.4.5 Computational Generated Spring Networks

To further confirm our findings, we studied computationally generated spring networks. These spring networks employed varying ratios of stiff and soft springs located randomly within the lattice. Part of our motivation for carrying out these simulations was due to the fact that the spatial distribution of hard particle dopants in the experimental samples was not perfectly random. We therefore hoped to clarify whether this lack of perfect randomness would affect any of the conclusions we made about the phonon spectra.

The computer simulations employed particles with equal masses on triangular lattices. The particles were randomly chosen to have one of two spring constants, k_1 or k_2. We set k_2 to be five times larger than k_1. Particles with spring constant k_2 are referred to as "stiff" and particles with spring constant k_1 are referred to as "soft". The effective spring between two neighboring particles is the mean value of the spring constants of the two particles. In other words, the effective spring constant k_{ij} between neighboring particles i and j is given by $k_{ij} = (k_i + k_j)/2$, where k_i and k_j are the spring constants of individual particles i and j, respectively. This model was employed to be consistent with our experiments, wherein two hard particles are coupled by an effectively stiff spring, two soft particles are coupled by an effectively soft spring, and hard-particle/soft particle pairs are coupled by an effective spring of intermediate stiffness. All

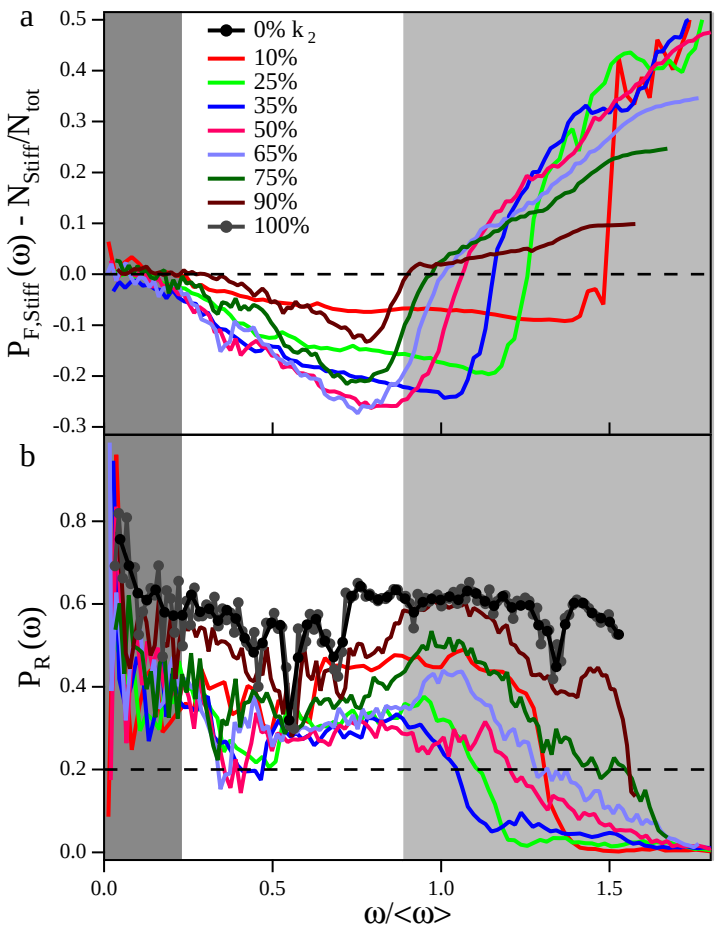

Figure 2.13: a) Stiff-particle participation fractions shifted by stiff-particle number fractions $P_{F,Stiff}(\omega) - N_{Stiff}/N_{tot}$ as a function of frequency scaled by the mean frequency $\omega/\langle\omega\rangle$ for computationally generated springs networks, excluding those which are purely soft particles or purely stiff particles. Dotted line represents equal participation. b) Participation ratio $P_R(\omega)$ as a function of frequency scaled by the mean frequency $\omega/\langle\omega\rangle$ for all computationally generated spring networks, including those which are purely soft particles (black line with dots) or pure stiff particles (grey line with dots). Dotted line represents localized versus extended threshold. Legend is for both figures, however data for 0% and 100% stiff particle crystal only in Figure b. Note, the dark grey region represents the low frequency, equal participation regime, the white region represents the soft-sphere dominated, extended motion regime, and the light grey region represents the hard-particle dominated, localized motion regime.

non-nearest neighbor springs were set to zero. We thus generated a spring constant matrix K based on nearest neighbor spring interactions; K, in turn, gives rise to a dynamical matrix D for the spring network. The eigenvalues and eigenvectors of D were calculated, and the frequencies, participation fractions, participation ratios, etc., were derived. One hundred different initial configurations were employed for each network. Networks were chosen with 0, 10, 25, 35, 50, 65, 75, 90, and 100 percent stiff particles. By averaging over 100 iterations, we minimized effects specific to any one configuration.

Plots derived from these "computationally generated data", analogous to those of the experimental data in Fig. 2.12, are provided in Fig. 2.13. Notice that the computationally generated networks exhibit the same three frequency regimes as the experimental systems. Further, the participation ratios, $P_R(\omega)$, of all computationally generated spring networks (0% to 100% stiff particles) exhibit trends similar to experiment. Thus, it appears that the small non-randomness in the experimental dopant spatial distribution does not introduce any systematic errors that affect our primary conclusions.

2.5 Conclusion

In summary, the vibrational modes in soft-particle crystals doped with hard particles exhibit three distinct frequency regimes. At low frequencies, crystalline (Debye-like) behavior in the DOS is observed in all systems regardless of doping. These low frequency modes display long wavelength behavior in which hard and soft particles participate equally. At intermediate frequencies, the modes are extended and dominated by soft particles. At the highest frequencies, the modes are more localized and dominated by hard particles. Our computationally generated

spring networks exhibit many of the trends observed here and even extrapolate to higher number fractions of hard spheres.

The experimental results imply that while the introduction of bond-strength disorder does indeed alter some of the vibrational properties of crystalline materials, compared to the introduction of structural disorder, it does not as readily destroy the crystalline/Debye-like properties at low frequencies. Thus, at least within the present experimental regimes, it appears that structural order in crystalline materials is more important than bond homogeneity for maintaining crystalline phonon properties at low frequencies. This finding is in conflict with previous simulation work on interaction disordered crystals which have found a boson peak at low frequencies when enough disorder is present [82–86]. The previous simulation work examined a variety of spring constant distributions including a box distribution with plus/minus 20% variation about the average [82], truncated Gaussian distributions with widths varying from 0.6 to 1 [83, 85], power law distributions [84], and binary distributions with a spring constant ratio of 0.1 [84, 86]. None of these simulations matches our experimental conditions exactly, and the simulations of binary distributions are closest to our experiments. However, these simulations started with a crystal of primarily hard springs and then doped it with soft springs. By contrast our experiments employed a soft crystal doped with hard particles. Also, the simulations used only two spring constants (soft and hard), whereas our experiments had three distinct spring constants (soft, hard, and intermediate stiffness) corresponding to our three inter-particle interactions, *i.e.*, soft-soft, hard-hard, and soft-hard, respectively.

2.6 Future Work

Possible future work (related to previous simulation research) could include increasing the concentration of hard spheres, or starting with hard-particle crystals and adding soft-particle dopants. These experiments should be possible but are technically more difficult because the hard polystyrene particles scatter significantly more light than the PNIPAM particles, and tracking PNIPAM particles surrounded by a large number of polystyrene particles is difficult.

Looking further to the future, it should be interesting to increase the bond-strength disparity by using softer particles. This variation, as well as the use of higher hard particle concentrations, would enable us to probe systems closer to the onset of mechanical instability. The responses of these materials to mechanical perturbations would also be interesting to study. Given that colloidal glasses have been shown to possess quasi-localized "soft spots" which correlate with the location of structural rearrangements [2, 63–68], it would be interesting to see when and if the soft spheres would become "literal" soft spots in hard crystals that facilitate rearrangements (due to thermal motion or mechanical stress). Finally, in a different vein, these systems potentially offer a new class of so-called phononic materials in which localization of elastic energy can influence wave transport [162, 163].

Chapter 3

Tunable depletion potentials driven by shape variation of surfactant micelles

3.1 Introduction

An entropic attractive force, often called the depletion force, arises between large colloidal particles in suspension when many small non-adsorbing particles or (macro)molecules, called depletants, are added to the suspension [91, 92]. Over the years, depletion forces have proved valuable as a means to control and study phase behavior [17, 30–34, 93–101, 164], to direct self-assembly [18, 35–42, 44–46, 102, 104], and to control the stability of colloidal suspensions [105, 106, 108, 110–118]. It is thus important to fully understand depletion phenomena, as well as continue to explore new means to induce and manipulate depletion forces.

Most depletants are spherical in shape. However, over the years, depletants with other geometric shapes have been utilized, *e.g.,* rods or disks [105, 106, 126–139]. Regardless of their

shape, all depletants induce entropic attractions, but the functional form and strength of the induced interparticle potential depends on their shape. At the same volume fraction, for example, small rods of length L will induce a stronger attraction than small spheres with diameter L [126–128], and the functional form of the potential induced by rods also exhibits more curvature than that of the potential induced by spheres. In practice it is often desirable to vary interaction strength, and this task is usually accomplished by varying depletion volume fraction, *e.g.,* by adding or subtracting small particles [17, 30–34, 42, 44, 93, 97, 98, 102, 105, 108] or by changing the radius of spherical depletants [36, 37, 46, 99–101, 104].

In this chapter we introduce shape *anisotropy* tuning as a means to control depletion interactions in suspension. Specifically, we employ temperature variation to change the shape of nanometer-size surfactant micelles from sphere-like to cylinder-like. As a result, the corresponding depletion potential depth and range is modulated. The potentials are derived from video microscopy measurements of the pair correlation function of micron-sized silica spheres suspended in a solution of hexaethylene glycol monododecyl ether ($C_{12}E_6$) surfactant micelles. The depletion potentials are revealed to vary substantially in magnitude and range with temperature. We demonstrate that these effects arise from shape anisotropy variation, wherein nearly spherical $C_{12}E_6$ micelles at low temperatures grow and elongate into cylindrical micelles of constant cross-sectional diameter and longer lengths at higher temperatures. By fitting the measured interaction potentials to theoretical models for depletion forces of rod-like/ellipsoidal depletants [131], we extract the length and shape anisotropy of the micelles as a function of temperature. The resultant derived dimensions of suspended micelles are found to be roughly consistent with neutron scattering data for $C_{12}E_6$ [3].

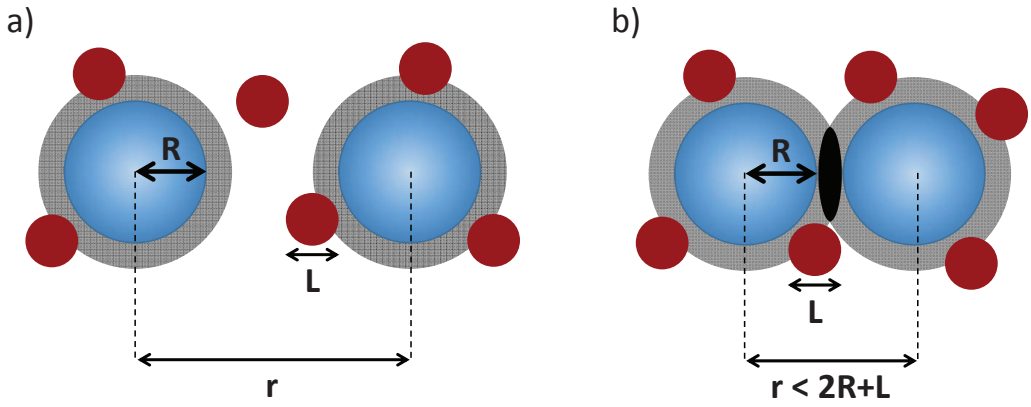

Figure 3.1: Depletion between colloidal particles of radius, R, in suspension of spherical depletants with diameter, L. a) The sphere centers cannot fit within regions of excluded volume (grey shaded region). b) When excluded volumes of two spheres overlap, the sphere entropy increases in proportion to excluded volume overlap (black region), and an attractive force thus arises between colloidal particles. Spheres and colloidal particles not drawn to scale.

3.2 Contextual and Theoretical Background

3.2.1 Depletion Due to Spherical Depletants

The depletion interaction between colloidal spheres due to small spherical depletants is well understood, especially when large and small spheres concentration are in the dilute limit. In this case, for colloidal spheres of radius R in a suspension of smaller spheres (depletants) of diameter L ($2R >> L$), there exists a shell of thickness $L/2$ around the large colloidal spheres that the center of the depletants cannot enter (Figure 3.1). This shell region is referred to as the "excluded volume". When the center-to-center distance, r, between two colloidal spheres is less than $2R + L$ (Fig. 3.1b), the excluded volumes of the two large spheres overlap, creating a so-called "overlap volume". The creation of this overlap volume effectively decreases the total excluded volume in the sample, and, in turn, increases the accessible free volume available to the depletants. This situation is entropically favorable for the depletants. It lowers the free energy

of the system, and thus an entropic force proportional to the overlap volume is induced between the two colloidal spheres in the presence of small depletants.

The functional form of the depletion interaction induced by spherical depletants is $U(r)/k_BT = -3\rho(R/L)\,(1-(r-2R)/L)$ [91, 92]. Here, L denotes depletant sphere diameter; k_B is the Boltzmann constant, T is temperature, ρ is the depletant volume fraction, r is the center-to-center distance between colloidal particles, R is the large particle radius, and $r-2R$ is the surface-to-surface distance between colloidal particles, sometimes denoted as h in other studies [126–128, 131]. Traditionally the depletant volume fraction is denoted by ϕ, however, we use ϕ to denote the *particle* packing fraction throughout this thesis. For the sake of consistency, and to hopefully minimize confusion, we use ρ to represent the depletant volume fraction. Notice, the potential minimum (attraction strength) between particles at contact ($r = 2R$) depends on depletant volume fraction and the ratio of large- to small-sphere diameter, *i.e.*, $U(2R)/k_BT = -3\rho(R/L)$.

3.2.2 Depletion Due to Thin-Rod Depletants

For thin-rod depletants, the same principles apply as in the spherical depletant case. However, while spherical depletants only have translation entropy, the rod-shaped depletants have orientational entropy as well as translation entropy. In the case of rod depletants, in the dilute concentration limit, the entropic interaction between large colloidal spheres is $U(r)/k_BT = -(2/3)\rho(RL/D^2)\,(1-(r-2R)/L)$ [126–128]. Here L is the depletant rod length, and D is the depletant rod cross-sectional width with the assumption $D/L << 1$. The potential minimum at contact remains directly proportional to the depletant volume fraction, but it also depends on rod length, *i.e.*, $U(2R)/k_BT = -(2/3)\rho(RL/D^2)$. Notice that increasing rod length, while

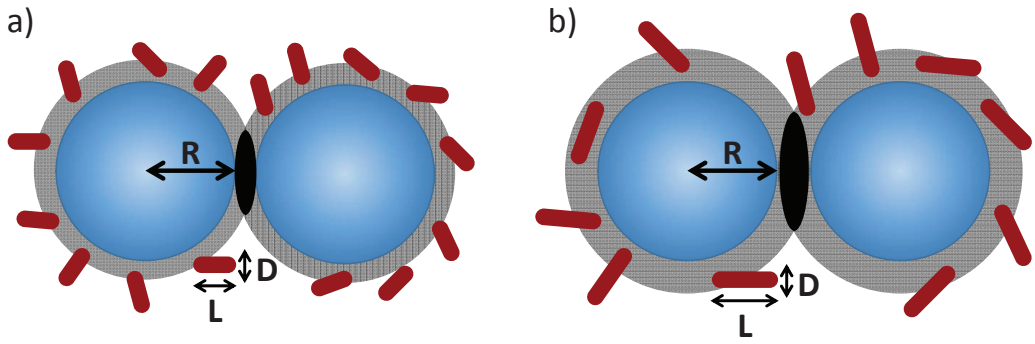

Figure 3.2: Depletion between colloidal particles of radius, R, in suspension of rods with length, L, and cross-sectional diameter, D. The rod centers cannot fit within regions of excluded volume (grey shaded region). a) When excluded volumes of two spheres overlap, the rod entropy increases in proportion to excluded volume overlap (black region), and an attractive force thus arises between colloidal particles. b) When rod length, L, is increased, while keeping rod volume fraction ρ and cross-sectional diameter D constant, then the excluded volume overlap increases, and the strength and range of the attraction between colloidal particles increases. Rods and colloidal particles not drawn to scale.

holding the rod volume fraction and cross-sectional width fixed, increases the attraction strength and decreases the number of rods. This increase in attraction strength with increasing rod length arises from a comparative increase in the free volume accessible to the longer rods, see Figure 3.2.

3.2.3 Depletion Due to Ellipsoidal Depletants

When the rod cross-sectional width of the depletant is no longer negligible compared to the rod length, then the situation becomes more complex. In this case, the depletants are better modeled as ellipsoids or cylinders. For ellipsoidal depletants the potential minimum is proportional to depletant volume fraction, and to the long/major ellipsoid axis length (L). The aspect ratio of the ellipsoidal depletants is significant too. The attraction strength grows with increasing aspect ratio, and the shape of the potential also depends on aspect ratio. The potential function for

ellipsoidal depletants has been derived [131] and is given below; it has a different functional forms for interparticle separations less than versus greater than the semi-minor axis length (D). The entropic interaction is:

$$\frac{U(r;L,D,R,\rho)}{k_BT} = \rho\frac{RL}{D^2}Q(r;L,D) \tag{3.1}$$

with

$$Q(r;L,D) = \begin{cases} x(r) - \frac{x(r)^2}{2} - \frac{2}{3} - \frac{4}{3A^2} \\ \qquad + \frac{x(r)}{A\sqrt{A^2-1}}\ln\left(A+\sqrt{A^2-1}\right) & for\ \ 2R \le r < 2R+D \\ \\ x(r) - \frac{x(r)^2}{2} - \frac{2}{3} - \frac{4}{3A^2} + \frac{\left[(Ax(r))^2+8\right]\sqrt{(Ax(r))^2-4}}{12A^2\sqrt{A^2-1}} \\ \qquad + \frac{x(r)}{A\sqrt{A^2-1}}\ln\left(\frac{2A+2\sqrt{A^2-1}}{Ax(r)+\sqrt{(Ax(r))^2-4}}\right) & for\ \ 2R+D \le r < 2R+L \end{cases} \tag{3.2}$$

where $x(r) = (r-2R)/(L/2)$ is the dimensionless interparticle separation, and $A = L/D$ is the ellipsoid aspect ratio. Note, this function may seem complicated, especially by comparison to the functional forms for spherical and infinitely thin rod depletants, but the result is quite robust. For example, in the limit where $A = 1$, *i.e.*, spherical depletants, the potential minimum at contact calculated from equation 3.1 is identical to the potential minimum for spherical depletants provided earlier ($U(2R)/k_BT = -3\rho(R/L)$). Similarly, in the opposite limit where $A \longrightarrow \infty$, *i.e.*, thin-rod depletants, the potential minimum at contact calculated from equation 3.1 is identical to the potential minimum for thin-rod depletants provided earlier ($U(2R)/k_BT = -(2/3)\rho(RL/D^2)$). While the exact functional form of the potentials in

these two limits as given by Eq. 3.1 are not identical to the functional forms shown earlier for spherical and thin-rod depletants, Piech and Walz showed numerically that the shape of the potential curves in the two limits are in fact very similar to those of the traditional spherical and thin-rod depletants. Thus we employ this functional form of the interparticle potential for fitting to interparticle potential data.

3.2.4 Depletion Interaction Due to Polydisperse Suspension of Rod-like Micelles

We also considered the distribution of sizes of the surfactant micelles in suspension by incorporating the size polydispersity of rod-like $C_{12}E_6$ surfactant micelles into our fitting procedure. Our polydispersity model of the size distribution function is derived from the "Ladder Model" described by Missel *et al* [165]. We describe the main assumptions and arguments behind this analysis below.

Since the length of rod-like surfactant micelles, L, is directly proportional to the number of surfactant molecules that compose the micelle, N, when we incorporate the micelle polydispersity into our model it is useful to denote the length of the micelles as $L(N)$. Rod-like micelles consist of two spherical caps connected by a cylindrical body. The diameter of the spherical caps is equal to the cross-sectional diameter of the rods (cylindrical body), D. Thus the smallest possible micelle length is D, *i.e.*, a spherical micelle of diameter D. The number of surfactant molecules in the spherical micelles is the minimum aggregation number, N_0. This also means that for all sizes of micelle, N_0 molecules reside in the spherical caps, and $N - N_0$ molecules reside in the cylindrical body. The total micelle length, $L(N)$, is given by $L(N) = D + (N - N_0)d/N_d$, where d is the effective diameter of the hydrophilic head of a surfactant molecule and N_d is the number of molecules which comprise a disk of diameter D

and thickness d. The quantity d/N_d is therefore the incremental length increase of a micelle by the addition of a single surfactant molecule to the cylindrical body. We derive d/N_d through geometric arguments about the shape of the micelles and the packing of the surfactant molecules in the micelles.

We first estimate the value of d by comparing the size of a single surfactant molecule to the total surface area of a spherical micelle. Specifically, we know that N_0 molecules comprise a spherical micelle of diameter D, and thus the surface area of a spherical micelle is filled with N_0 circles of diameter d (diameter of the surfactant molecules's hydrophilic head). Therefore, we can determine d from:

$$4\pi \left(\frac{D}{2}\right)^2 = N_0 \pi \left(\frac{d}{2}\right)^2, \tag{3.3}$$

where D is the spherical micelle diameter, N_0 is the minimum aggregationg number, and d is the diameter of the surfactant molecules hydrophilic head. Solving for d, we find $d = 2D/\sqrt{N_0}$.

Next, we estimate N_d, the number of molecules which comprise a disk of diameter D and thickness d, by comparing the size of a single surfactant molecule to the circumference of a circle with diameter D, *i.e.,* the circumference of a micelle's cylindrical body. To determine N_d, we find the number of molecules, of width d, that fit along the circumference of a circle of diameter D, *i.e.*, $\pi D = N_d d$. Solving for N_d, and substituting the solution for d from Equation 3.3, we find $N_d = \pi\sqrt{N_0}/2$.

Using these estimates for d and N_d, we find $d/N_d = 4D/\pi N$. Thus, we can define the incremental length increase of a micelle by the addition of a single surfactant molecule to the cylindrical body, d/N_d in terms of known quantities, specifically the micelle width D and the minimum aggregation number N_0. The equation for the micelle length, $L(N)$, can now be

written as:

$$L(N) = D + (N - N_0)\frac{4D}{\pi N_0}. \tag{3.4}$$

The number concentration of micelles of length $L(N)$ in solution, $X_{L(N)}$, has the form [165]:

$$X_{L(N)} = Ce^{-N/M}, \tag{3.5}$$

where C is a constant in units of number concentration and M is a unitless constant that defines the broadness of the distribution. The constant C is derived when normalizing the distribution for the total volume fraction of micelles in solution. The constant M is extracted by fitting to our experimentally measured $U(r)$.

The volume fraction of micelles length $L(N)$ in solution, $\rho_{L(N)}$, is then calculated using the number concentration $X_{L(N)}$:

$$\rho_{L(N)} = X_{L(N)}\left(\frac{4}{3}\pi\left(\frac{D}{2}\right)^3 + \pi\left(\frac{D}{2}\right)^2(N - N_0)\frac{4D}{\pi N_0}\right). \tag{3.6}$$

We then constrain $\rho_{L(N)}$ such that:

$$\sum_{N=N_0}^{\infty} \rho_{L(N)} = \rho. \tag{3.7}$$

Finally, we substitute $\rho_{L(N)}$ and $L(N)$ for ρ and L, respectively, in Equation 3.1, and perform a summation over N to derive the interaction potential induced by a polydisperse suspension of

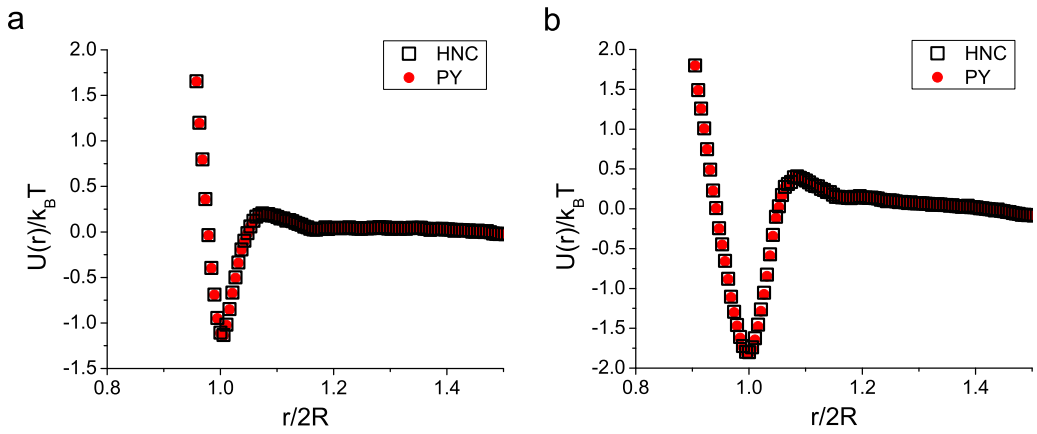

Figure 3.3: Examples of calculated interparticle interaction potentials, $U(r)/k_BT$, using the Hypernetted Chain (HNC, black squares) and the Percus-Yevick (PY, red circles) approximations for a) $25\ ^oC$ and b) $27\ ^oC$. Notice, there is little difference between the two approximations.

rod-like micelles:

$$\frac{U(r;M,N_0,D,R,\rho)}{k_BT} = \frac{R}{D^2}\sum_{N=N_0}^{\infty}\rho_{L(N)}L(N)Q(r;L(N),D). \tag{3.8}$$

The average length, $\langle L\rangle$, of the distribution is calculated from:

$$\langle L\rangle = \frac{\sum_{N=N_0}^{\infty}L(N)X_{L(N)}}{\sum_{N=N_0}^{\infty}X_{L(N)}}. \tag{3.9}$$

3.2.5 Deriving the Pair Interaction Potential

In the limit where particle packing density ϕ approaches zero, the pair interaction potential, $U(r)$, is related to the radial distribution function, $g(r)$, via the Boltzman relation, $g(r) = exp[-U(r)/k_bT]$ [166]. However, when the particle packing density, ϕ, is finite, as is the case in the experiments presented in this chapter, then $g(r)$ is instead related to the potential of mean force, $w(r)$, via the Boltzmann relation, $g(r) = exp[-w(r)/k_BT]$ [166]. This potential of mean

force $w(r)$ is due to the pair interaction potential $U(r)$ as well as the many body effects that arise at finite ϕ. Therefore, $U(r)$ is generally extracted from the experimentally calculated $w(r)$ by removing the contributions from many body effects. This extraction is accomplished by employing closure relations to solve the Ornstein-Zernike integral equation [166]. Specifically, the Hypernetted Chain (HNC) and Percus-Yevick (PY) approximations are quite often utilized for this task. The true pair interaction potential, $U(r)$, is calculated numerically from $w(r)$, where $w(r) = -k_B T ln[g(r)]$; $U(r)$ is thus calculated from the experimentally measured $g(r)$ via the following relations:

$$\frac{U(r)}{k_B T} = -ln\left[g(r)\right] + \begin{cases} \frac{\phi}{\pi R^2} I(r) & (HNC) \\ \ln[1 + \frac{\phi}{\pi R^2} I(r)] & (PY), \end{cases} \tag{3.10}$$

where $I(r)$ is the convolution integral,

$$I(r) = \int [g(r') - 1 - \frac{\phi}{\pi R^2} I(r)][g(\left|r - r'\right|) - 1] d^2 r'. \tag{3.11}$$

These equations are readily solved numerically [167]. We report results using the HNC approximation, which we found to be in excellent agreement with the PY approximation (Figure 3.3).

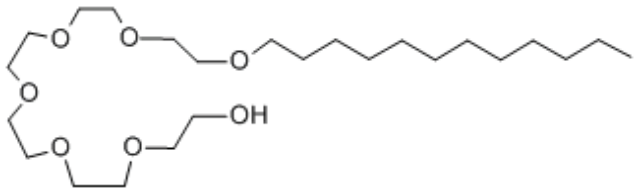

Figure 3.4: Chemical structure for hexaethylene glycol monododecyl ether ($C_{12}E_6$).

3.3 Experimental and Analytical Methods

3.4 Experimental Materials

To experimentally measure the shape-dependent depletion interaction induced by surfactant micelles, we suspend 1625 nm diameter silica microspheres (Duke Scientific) with 30 nm size standard deviation in a solution of 44 mM hexaethylene glycol monododecyl ether ($C_{12}E_6$, Molecular Formula $= C_{24}H_{50}O_7$, see Figure 3.4 for chemical structure) and 17 mM NaCl. The critical micelle concentration (CMC) of $C_{12}E_6$ is 7.2×10^{-2} mM at 25 °C [168]; the CMC is the concentration of surfactant at which micelles begin to form. The concentration of surfactant is more than 600 times that of the CMC. Thus, at such a high surfactant concentration, small changes in CMC with temperature do not significantly affect the suspended micelle volume fraction. Specifically, as the sample temperature changes, we expect the micelle volume fraction to remain constant. As a result, the depletant volume fraction was held constant in fits at all temperatures and was set equal to the volume fraction of surfactant in water, *i.e.*, $\phi = 0.02$.

Previous small angle neutron scattering (SANS) experiments provide independent estimates about the shape of $C_{12}E_6$ micelles. In these SANS experiments, micelles were modeled as rod-like with spherical caps. With increasing temperature, the length of the rods was measured to

increase, while the cross-sectional diameter remained constant. Specifically, the length increases from approximately $19 - 31$ nm over the temperature range studied in our work, and the cross-sectional diameter remains constant at approximately 4.3 nm [3]. Thus, the shape of $C_{12}E_6$ surfactant micelles can be tuned *in situ* through control of the sample temperature, and it provides an excellent model system to study shape-dependent depletion interactions. Because the aspect ratio ranges between 4.4 and 7.2, the cross-sectional diameter of the micelles is not negligible. Therefore, it is critical to employ the more complex functional form (Eq.3.1) as a theoretical model for the interaction potential [131].

Another parameter of the sample which had to be considered was the Debye screening length, κ^{-1}. In water, κ^{-1} is calculated using $\kappa^{-1} = 0.304/\sqrt{I(M)}$, where $I(M)$ is ionic strength expressed in molar concentration (mol/L) [169]. The salt concentration, $I(M) = 0.017$ mol/L, yields a screening length $\kappa^{-1} = 2.3$ nm. Although this screening length is negligible compared to the colloidal particle diameter, it is significant when compared to the micelle length and width [3]. Thus, the screening length should be included when fitting theoretical interaction potential predictions to experimental data. To this end, we introduce an *effective* rod length, $L' = L + 2\kappa^{-1}$, and an *effective* rod width, $D' = D + 2\kappa^{-1}$, in place of L and D in Equation 3.1. With this notation L and D are the "true" (bare) length and width of the rod, respectively.

Samples were prepared by loading particle-surfactant solution between two glass coverslips. The concentration of silica spheres was selected such that the areal packing density, ϕ, was approximately 0.08 in the two-dimensional (2D) regions we studied. The temperature of the sample was controlled via an objective heater (Bioptechs), and measurements were made for temperatures ranging from 22 °C to 28 °C in 1 °C steps. Bright-field microscopy video was

recorded at 30 frames per second for $65,000$ frames. Subpixel particle tracking algorithms were employed to find particle positions in each frame of the video [87].

3.4.1 Correcting Radial Distribution Function for Imaging Artifacts

When imaging colloidal particles with bright field video microscopy, the images of the spherical particles appear as Airy patterns (Figure 3.5). Further, the experimentally measured radial distribution function, $g(r)$, has a systematic error caused by overlapping of neighboring particle Airy patterns. This systematic error leads to incorrect identification of particle centroids. Therefore, to calculate an accurate pair interaction potential, $U(r)$, we must first rid $g(r)$ of this systematic error. These corrections are well known and were carried out following procedures described in references [170, 171]. They are described in detail below.

We refer to the experimentally measured radial distribution function with Airy disk errors, $\tilde{g}(\tilde{r})$, as the "raw" radial distribution function. We refer to the undistorted radial distribution function, $g(r)$, as the "true" radial distribution function. The true $g(r)$ is related to $\tilde{g}(\tilde{r})$ through conservation of probability, $g(r)dr = \tilde{g}(\tilde{r})d\tilde{r}$. From this, we see that $g(r)$ can be obtained from

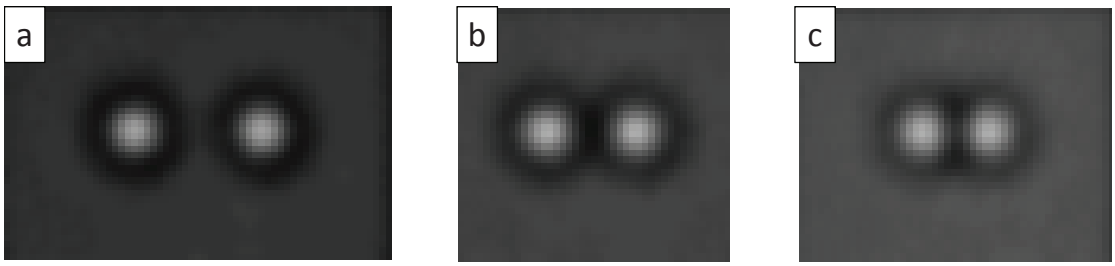

Figure 3.5: Sample images of lone colloidal particle and its mirror image used to correct particle tracking error due to overlapping Airy disks, for various known interparticle distances, r. a) Particle and mirror image with $r >$ a particle diameter, b) Airy disks barely overlapping, and c) Airy disks overlapping in the particle images.

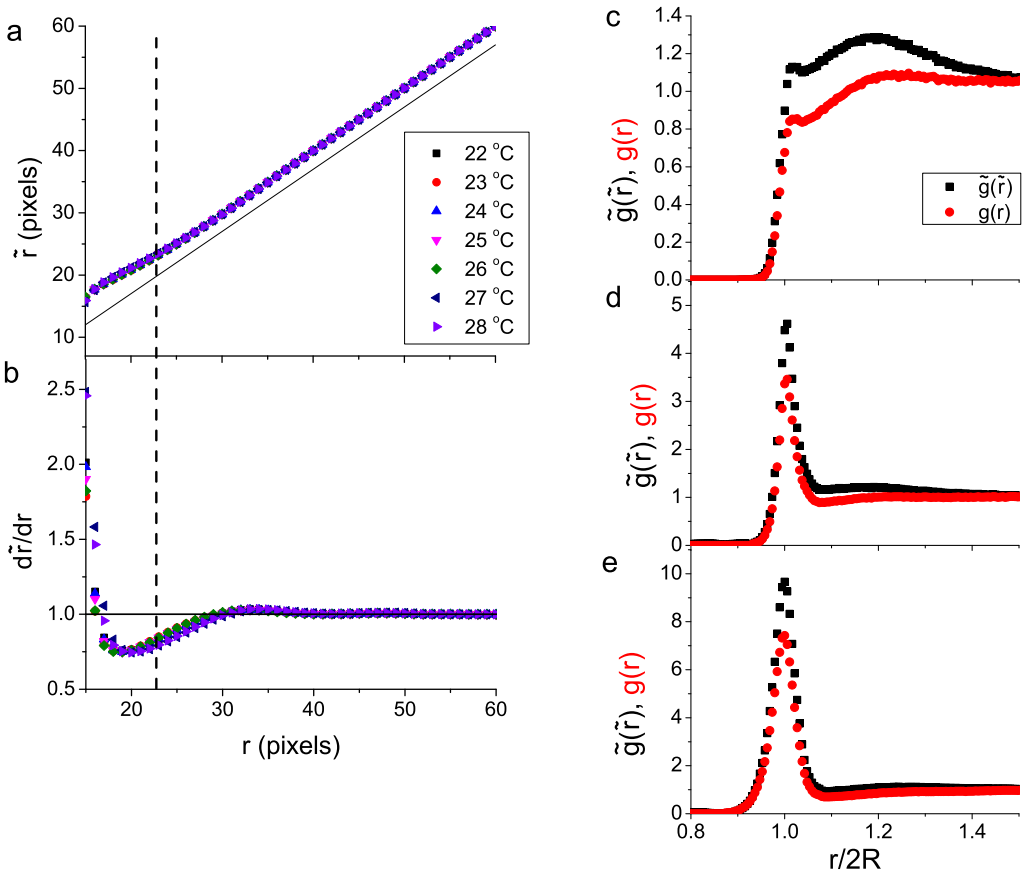

[b]

Figure 3.6: a) Measured center-to-center distance, $\tilde{r}$, as function of true center-to-center distance, r, calculated from Airy disk correction procedure for all temperatures. Solid black line represents slope$= 1$, *i.e.*, $\tilde{r} = r$. Dashed black line represents particle diameter, $2R = 18.9$ pixels. b) Derivative, $d\tilde{r}/dr$, of $\tilde{r}$ vs. r curves in a). Solid black line represents $d\tilde{r}/dr = 1$. Dashed black line represents $2R$. c)-e) Corrected and uncorrected radial distribution functions, $g(r)$ (red circles) and $\tilde{g}(\tilde{r})$ (black squares), respectively for temperatures c) $23\ ^o$C, e) $25\ ^o$C, and f) $27\ ^o$C.

the measured $\tilde{g}(\tilde{r})$ by,

$$g(r) = \tilde{g}(\tilde{r})\frac{d\tilde{r}}{dr}. \tag{3.12}$$

All that is required is to map r to $\tilde{r}$ and differentiate.

This task is accomplished by first identifying a "lone" colloidal particle, defined here as a particle with no other particles within a distance of three particle diameters, in a given frame of

the video data. A mirror image of this lone particle is created and placed some known distance away, r (Figure 3.5). The centroids of the particle and its mirror image are obtained using standard particle tracking techniques, and the distance between the measured centroid positions, $\tilde{r}$, is calculated. Thus, the measured center-to-center distance $\tilde{r}$ is calculated as a function of r for a given particle. This process is then repeated for all lone particles in the given video frame, and the average calculated $\tilde{r}$ versus r curves for all particles in the video frame is calculated. To ensure good statistics, the procedure is repeated for ten or more video frames and the resultant $\tilde{r}$ vs. r curves for each frame sampled are averaged together (Figure 3.6a). The derivative of the final averaged curve, $d\tilde{r}/dr$, is calculated (Fig. 3.6b) and then multiplied by the experimentally measured $\tilde{g}(\tilde{r})$ to yield the undistorted $g(r)$. This procedure is then carried out for each temperature separately. Exemplary $g(r)$ and $\tilde{g}(\tilde{r})$ curves are given in Fig. 3.6c)-e).

3.4.2 Finding the Pure Depletion Interaction

To account for effects of all other interactions, *i.e.*, imaging artifacts not caused by overlapping Airy disks or by the depletants, the pair interaction potential between silica spheres was also measured in the absence of depletants. This zero-depletant interaction potential was measured and then subtracted from the measured pair interaction potentials with depletants (Figure 3.7). In this way it was possible to derive pure depletion interaction potentials more accurately. At the lowest temperatures (22 °C - 24 °C), the potential well depth was small, *i.e.*, on the order of the measurement error, and full subtraction was critical. However, at higher temperatures (25 °C - 28 °C), the well depths were large and subtraction was only necessary for interparticle distances, r, larger than the range of the potential well.

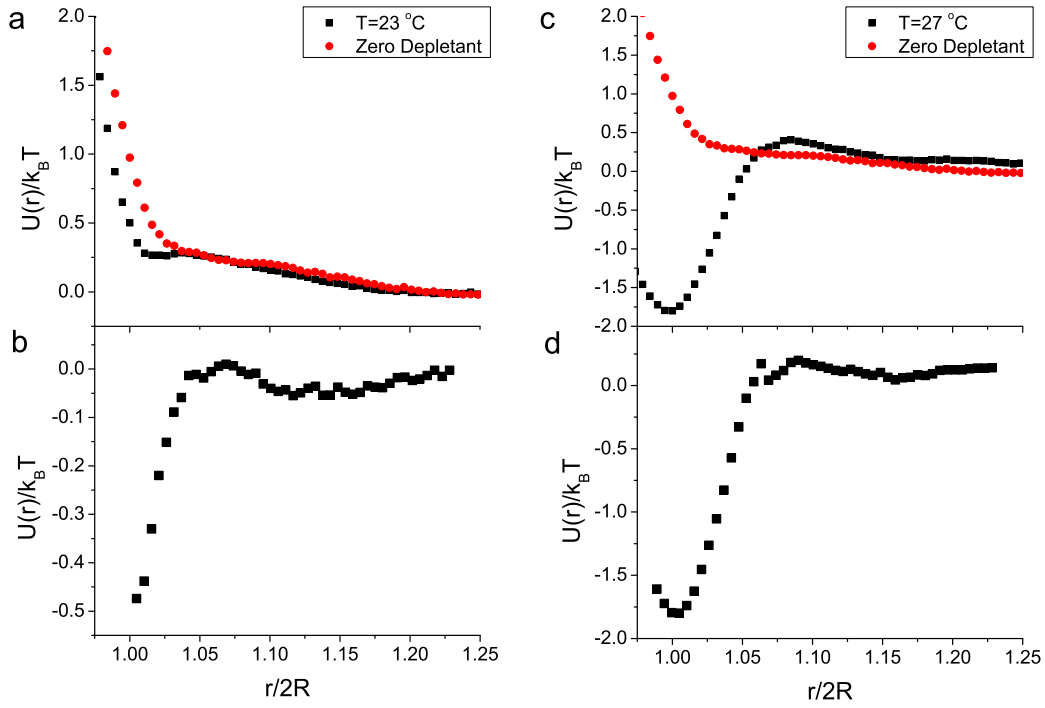

Figure 3.7: a) Measured pair interaction potentials with depletants for temperature $T = 23\ ^o$C (black squares) and zero-depletant potential (red circles). b) Pure depletion interaction potential for $T = 23\ ^o$C calculated from subtracting zero-depletant potential from measured pair interaction potential. c) Measured pair interaction potentials with depletants for temperature $T = 27\ ^o$C (black squares) and zero-depletant potential (red circles). b) Pure depletion interaction potential for $T = 27\ ^o$C.

3.4.3 Fitting Procedure

The experimental data was fit assuming a theoretical potential function, $U_t(r)$, based on the ellipsoid model (Eq. 3.1) defined earlier [131]. Here, the subscript t denotes a theoretical function. To fit the experimental data to the given $U_t(r)$ and thereby extract sample properties we implemented an iterative multi-step approach. A flow diagram of this procedure is provided in Figure 3.8.

The first step of the fitting procedure computes a theoretical potential $U_{t,i}(r; L_i', D', R, \rho)$

with an initial guess for the effective rod length L'. Here, the subscript i denotes the iteration number of the fitting procedure. The other parameters, effective cross-section diameter $D' = D + 2\kappa^{-1}$, colloid radius R, and depletant volume fraction (ρ), were tightly constrained by experiment and treated as constants. From the sample properties discussed in the materials section, D' was set to 8.9 nm, R was set to 1625 nm, and ρ was set to 0.02. The resulting initial estimate for the theoretical potential $U_{t,i}(r; L'_i, D', R, \rho)$ was then converted into a model pair correlation function, $g_{t,i}(r)$, via the Boltzmann relation, $g_{t,i}(r) = \exp[-U_{t,i}(r; L'_i, D', R, \rho)/k_BT]$.

It is important to account for the effects of colloidal particle polydispersity in the experiment. To account for this polydispersity $g_{t,i}(r)$ was broadened using a Gaussian kernel for the particle size with standard deviation σ, $\ker(r, \sigma) = \exp\left[-r^2/2\sigma^2\right]$. The standard deviation σ was set to 30 nm, *i.e.,* the value of σ for our particles as discussed in the materials section. It was kept fixed throughout the fitting process. Convolving the theoretical pair correlation function $g_{t,i}(r)$ with the Gaussian kernel yields a broadened pair correlation function, $g^B_{t,i}(r) = [g_{t,i} * \ker](r)$, which incorporates particle polydispersity. The superscript B denotes a broadened function. The broadened pair correlation function was then converted back to a broadened interaction potential $U^B_{t,i}(r; L'_i, D', R, \rho, \sigma)$ by taking the natural logarithm, *i.e.,* $U^B_{t,i}(r; L'_i, D', R, \rho, \sigma)/k_BT = -\ln(g^B_{t,i}(r))$, following the Boltzmann relation.

The effective depletant length L' was extracted by least-squares fitting of the experimentally determined $U(r)$ to the polydispersity broadened theoretical interaction potential $U^B_{t,i}(r; L'_i, D', R, \phi, \sigma)$. We observed that for initial guesses 5 nm $< L'_i < 60$ nm, the L' extracted from the fits converged to an $L' \pm 1$ nm. Finally, the "true" depletant length, L, was derived by subtracting the Debye screening length factor from the best-fit effective length, *i.e.,*

$$L = L' - 2\kappa^{-1}.$$

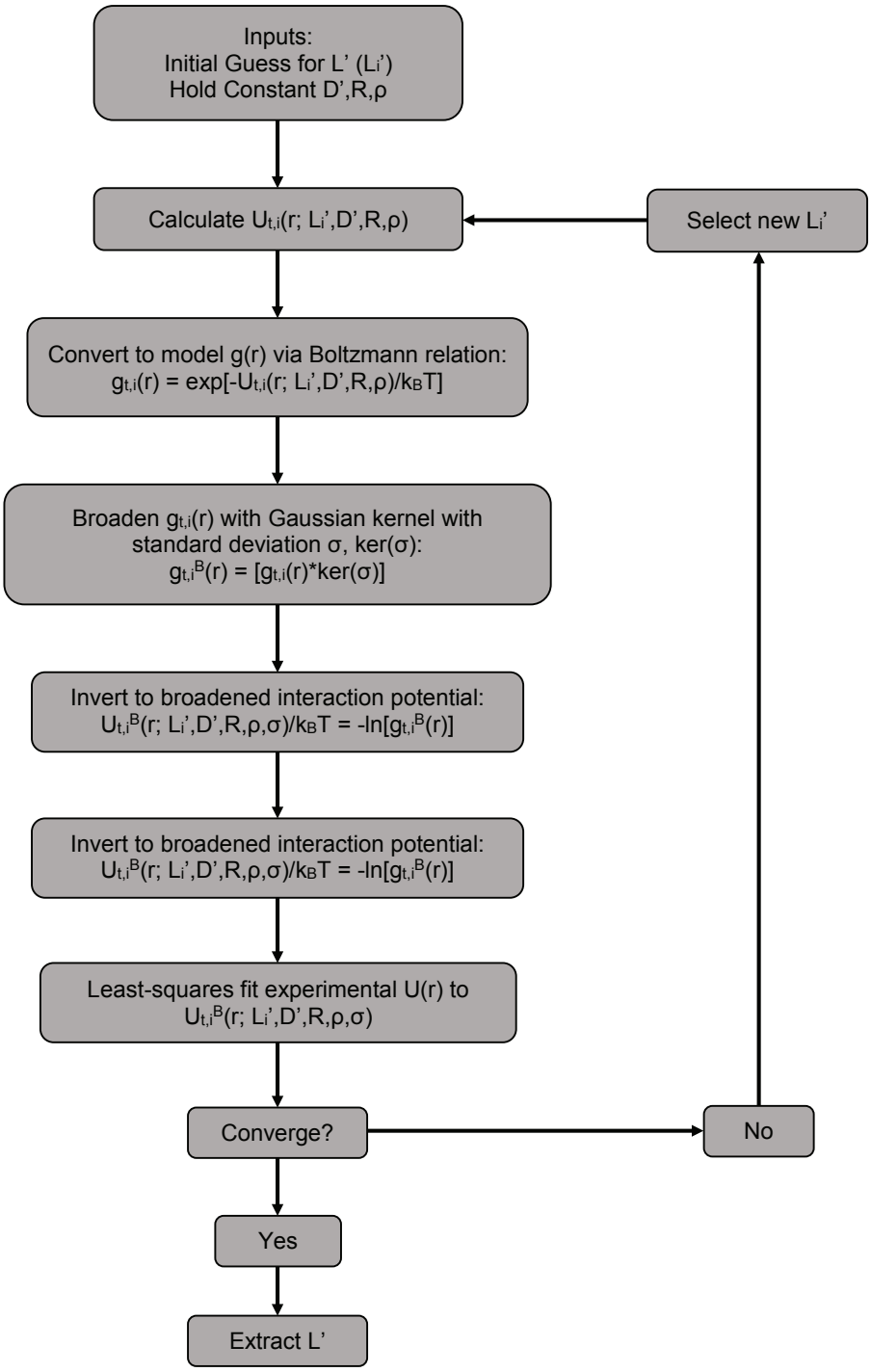

Figure 3.8: Flow chart diagram of $U(r)$ fitting procedure.

3.4.4 Incorporating Micelle Polydispersity in Fitting Procedure

To incorporate micelle polydispersity into our fitting procedure we follow a similar procedure as described above, but with some differences. The main difference is that the theoretical potential function, $U_t(r)$, is based off of the polydisperse suspension of rod-like micelles model (Eq. 3.8) instead of the (monodispersed) ellipsoidal model (Eq. 3.8). Since Equation 3.8 is not a function of L, but rather a function of M, the first step of this fitting procedure computes a theoretical potential $U_{t,i}(r; M_i, N_0, D', R, \rho)$ with an initial guess for the "decay constant" M. The values of D', R, and ρ are set to the same values as before, and again are treated as constant. The minimum aggregation number N_0 is set to 135 [172], and is also treated as constant. From this step forward the same procedure is followed as depicted in Figure 3.8, and M was extracted by least-squares fitting of the experimentally determined $U(r)$. With the value of M, the distribution of micelles sizes and the average *effective* micelle length, $\langle L' \rangle$ was calculated for all temperatures, and the "true" average length L was derived from $\langle L \rangle = \langle L' \rangle - 2\kappa^{-1}$.

For each temperature we observed that the value of M extracted from fits converged to an $M \pm 25$ for initial guesses $M - 100 < M_i < M + 100$. Such a change in M was found to cause marginal changes in the distribution of sizes and the average lengths calculated converged to $\langle L \rangle \pm 1$ nm. Another possible source of error is the value of the minimum aggregation number, N_0, which was taken from literature [172]. We observed, however, that changing N_0 by 10% led to changes in $\langle L \rangle$ of 1%. Therefore, any reasonable error in the value of N_0 causes only small errors in our results.

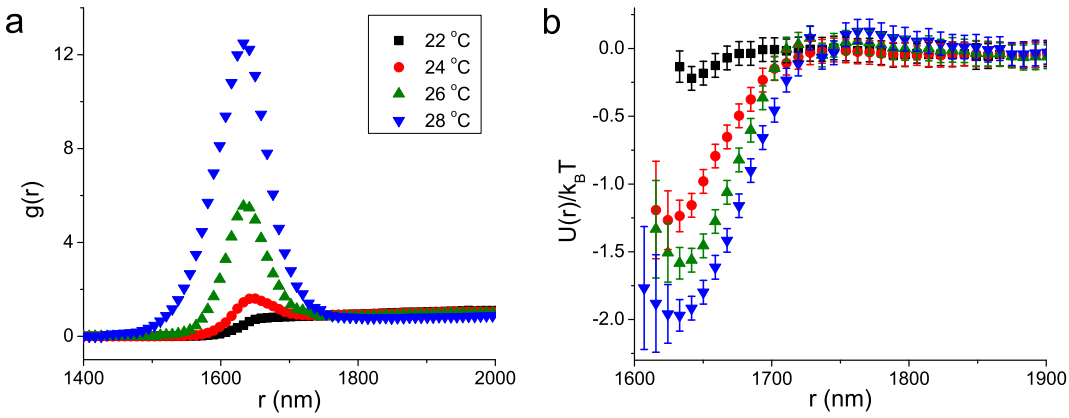

Figure 3.9: Experimentally measured a) radial distribution function, $g(r)$, and b) interparticle interaction potentials, $U(r)/k_BT$, for temperatures 22 °C, 24 °C, 26 °C, and 28 °C.

3.5 Results and Discussion

3.5.1 Measured Depletion Potentials

Depletion interaction potentials, $U(r)$, were calculated from experimentally measured radial distribution functions, $g(r)$. Exemplary $g(r)$ and $U(r)$ curves are shown in Figure 3.9. It is apparent that the depth of the potential well increases monotonically with temperature. The absolute value of the minimum of the measured potential, $|U_{min}/k_BT|$, is plotted as a function of temperature in Figure 3.10. Note that $|U_{min}/k_BT|$ denotes the potential well depth, defined here as the minimum value of the potential curve $U(r)$ (see inset of Fig. 3.10). The potential well depth, *i.e.*, attraction strength, increases from $\approx 0.2k_BT$ to $\approx 2k_BT$ over the range of temperatures studied. Thus, the interparticle interaction can be tuned from nearly hard-sphere to a strong attraction by increasing sample temperature. Further, the range of the interaction grows with increasing temperature. This effect is apparent from the widths of the $g(r)$ peaks and $U(r)/k_BT$ wells in Fig. 3.9.

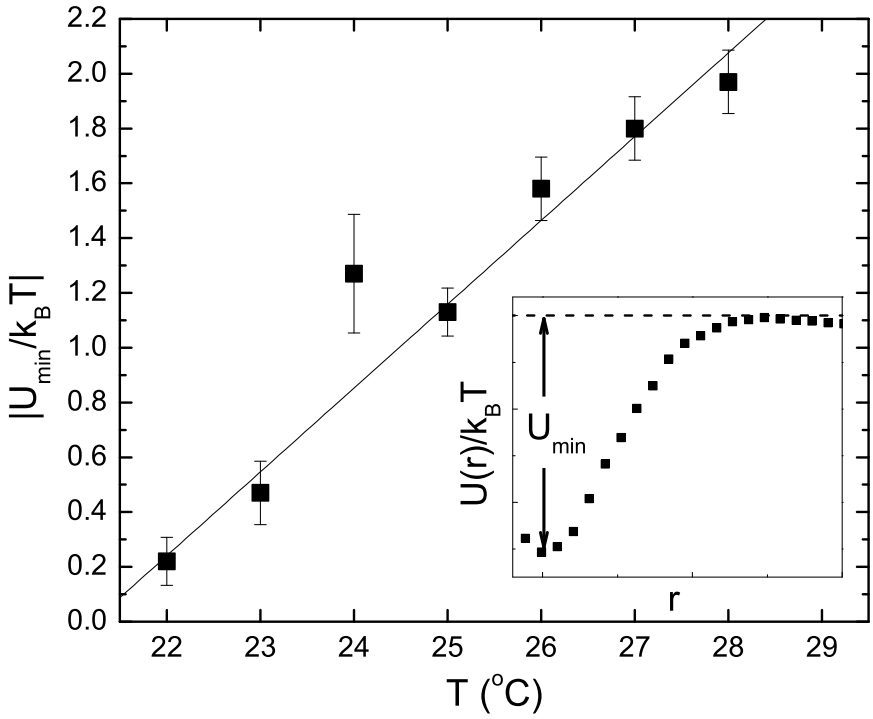

Figure 3.10: Absolute value of potential minima $|U_{min}/k_BT|$ of interaction potentials versus temperature T. Inset: Sample measured interparticle potential $U(r)$ showing U_{min} represents the potential well depth.

3.5.2 Rod Lengths Extracted from Fits

The observed increase in range and strength of the depletion attraction between colloidal particles is consistent with an increasing length of the rod-like micelle depletants. This effect is exhibited from the rod lengths L extracted from the fits. The calculated interparticle potentials with fits for all temperatures are shown in Figure 3.11. In Figure 3.12, the lengths extracted from the interaction potential fits are plotted as a function of temperature. Also shown are the lengths measured by small angle neutron scattering (SANS) [3]. The lengths extracted from the interaction potentials are in good agreement with the lengths from the SANS experiments for all but the lowest two temperatures (22 °C and 23 °C). However, the potential well depths for 22 °C and 23 °C were very small ($\approx 0.2k_BT$) and were of the same order as experimental error. Therefore,

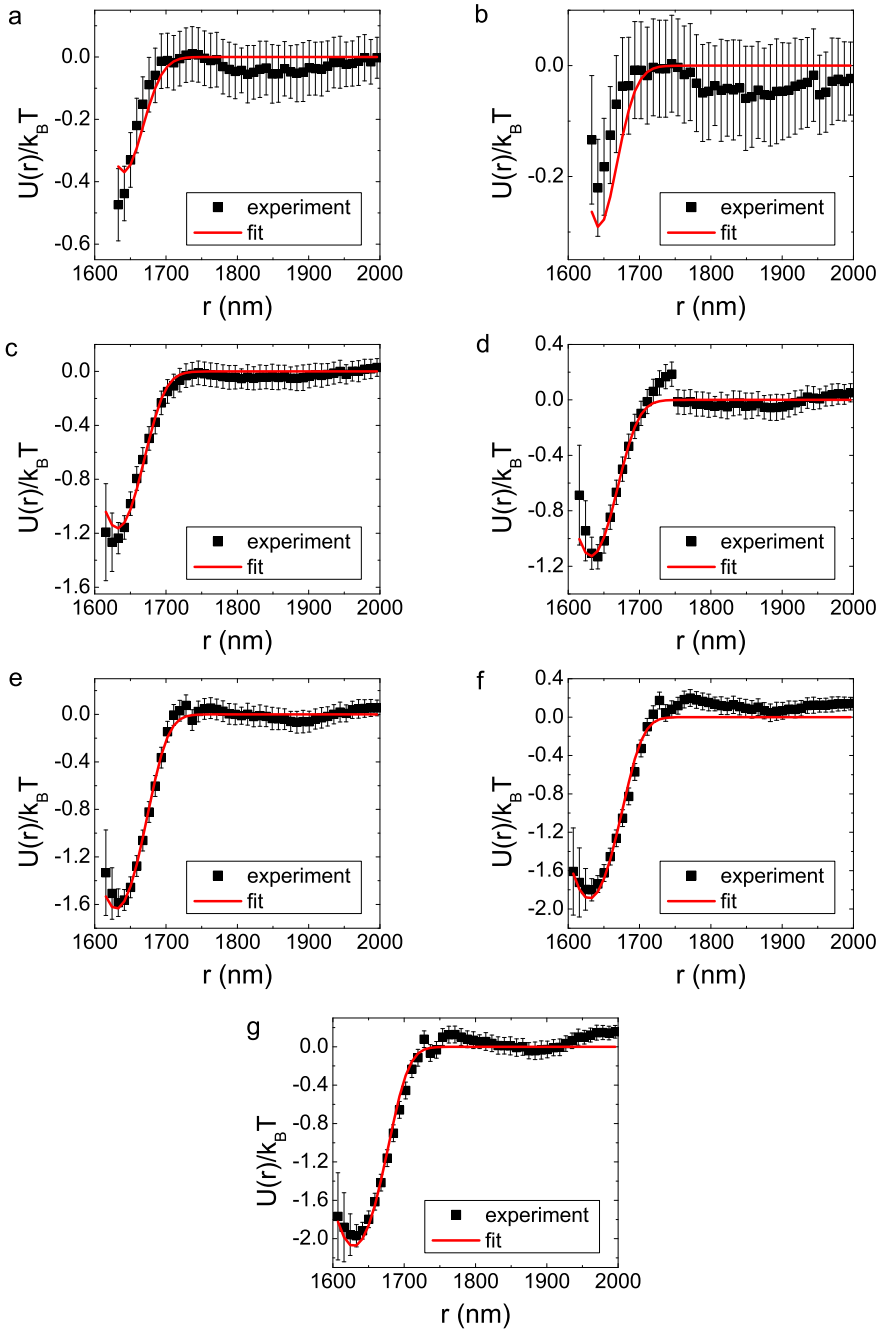

Figure 3.11: Experimentally measured interparticle potentials $U(r)/k_BT$ (black squares) and fits from the theoretical function for ellipsoidal depletants (red lines) for all temperatures. a) 22 °C, b) 23 °C, c) 24 °C, d) 25 °C, e) 26 °C, f) 27 °C, and g) 28 °C.

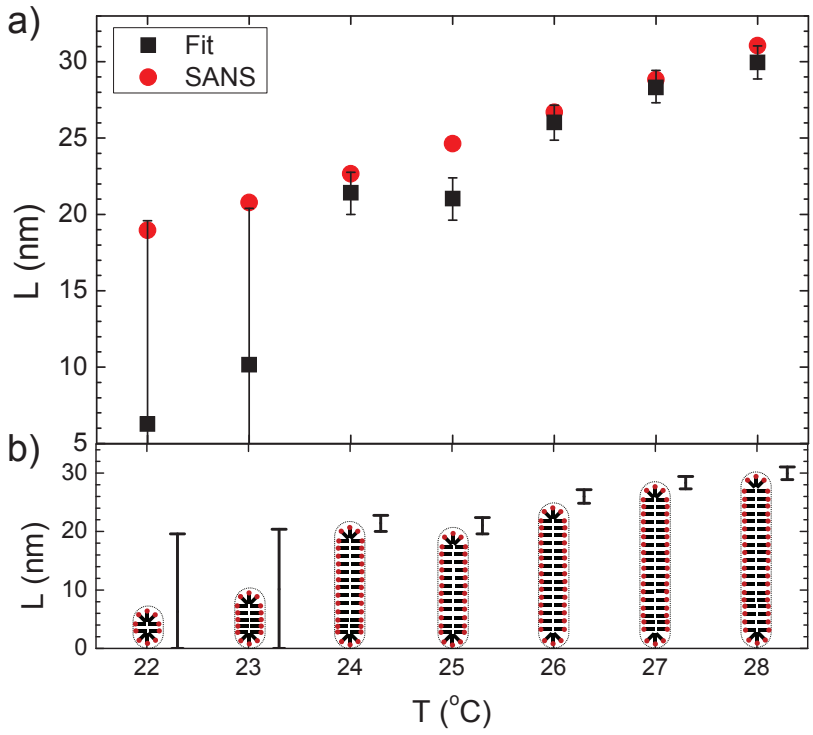

Figure 3.12: a) Rod length L of the surfactant micelles measured by depletion interaction (black squares) and by small angle neutron scattering SANS (red circles) in ref. [3] versus temperature T. b) Cartoon representations of change in dimensions, L and D, of the surfactant micelles as function of temperature T. Note here D remains constant.

data at these two (lowest) temperatures have large error bars. By contrast, the lengths measured from temperatures 24 °C to 28 °C are in good agreement with those measured by SANS. The schematic representations of the surfactant micelles as a function of temperature in Fig. 3.12b provide a visualization of the shape of the surfactant micelles over this temperature range. The cross-sectional diameter, D, stays constant at 4.3 nm, and the length, L, increases from ≈ 5 nm at 22 °C to ≈ 30 nm at 28 °C. The aspect ratio, L/D, of the surfactant micelles increases from nearly spherical (≈ 1) to rod-like (≈ 7) over the range of temperatures studied. We have thus determined the nano-scale increase in shape anisotropy of $C_{12}E_6$ surfactant micelles with increasing sample temperature by measuring the depletion interaction between colloidal spheres

induced by these micelles.

3.5.3 Distribution of Polydispersed Micelles

Using the model for a polydisperse suspension of rod-like micelles in solution, we extracted the decay constant, M, of the size distributions at all temperatures. The calculated interparticle potentials with fits for all temperatures are shown in Figure 3.13, and M as a function of temperature is plotted in Figure 3.14.

Exemplary size distributions X_L, scaled by the maximum value of the distribution, $\max(X(L))$, calculated from extracted values of M, are presented in Figure 3.15. We observed that as temperature increases, the size distribution of the micelles becomes broader. From the extracted X_L, the average micelle length, $\langle L \rangle$ was calculated at all temperatures. In Figure 3.16, the calculated average lengths are plotted as a function of temperature. Also shown are the lengths measured by SANS [3] and the lengths extracted from our fits assuming a monodisperse suspension of rods. We observed that while the fits in the polydisperse case did not appear to be as good as those in the monodisperse case, the average lengths calculated from these fits were not very far off the results obtained from our fits assuming a monodisperse suspension of rods and from SANS. Note that the average lengths at the two lowest temperatures are actually in better agreement with the SANS results than the monodisperse results. Also, the SANS results assumed a monodisperse suspension of rods. Therefore, it is not unreasonable that the results obtained using a model incorporating size polydispersity would not be in perfect agreement with those obtained assuming a monodisperse suspension of rods.

Note that the potential minimum of the fits from the polydisperse model do not agree with the minima of the experimental data. To further explore this system and model, we found the

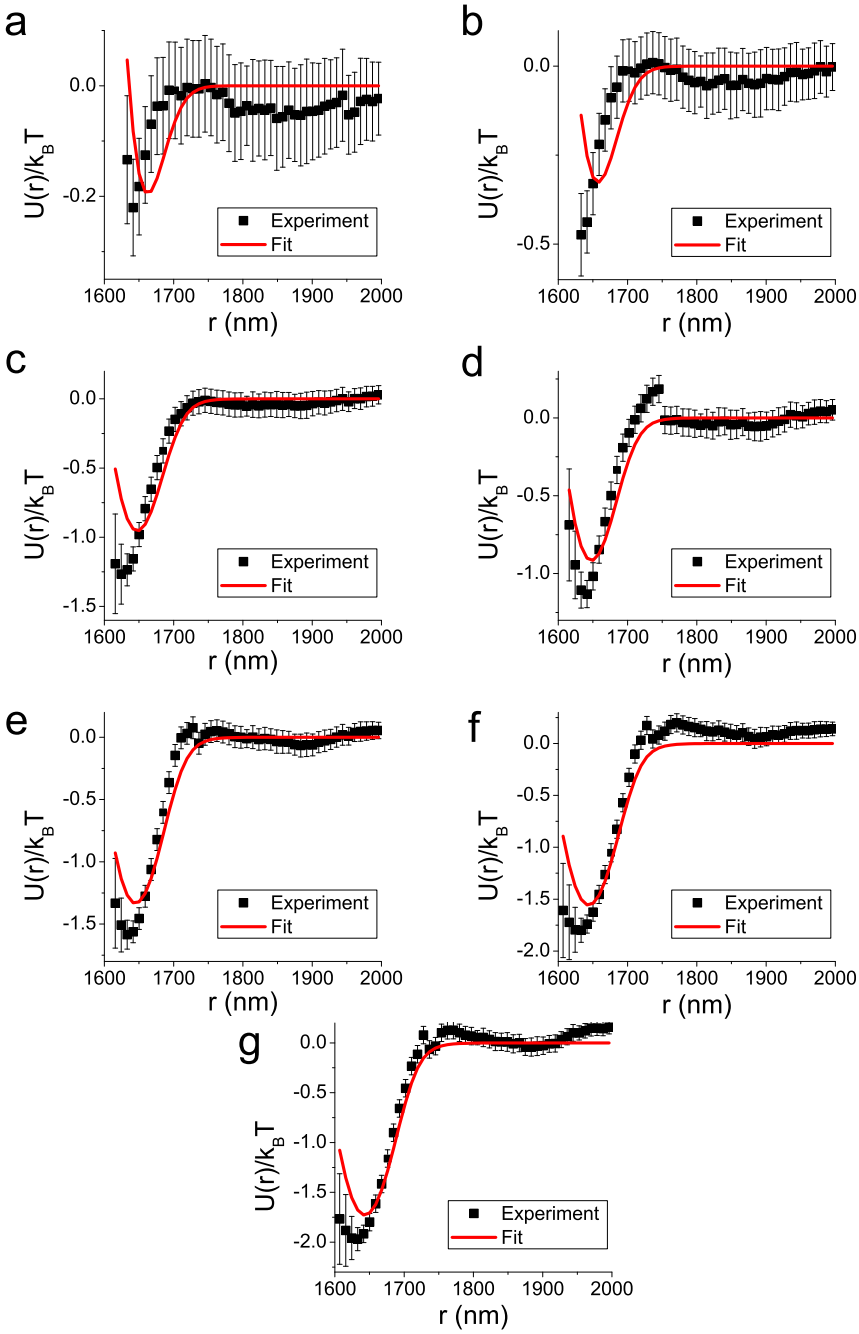

Figure 3.13: Experimentally measured interparticle potentials $U(r)/k_BT$ (black squares) and fits from the theoretical function for a polydisperse suspension of rod-like depletants (red lines) for all temperatures. a) 22 °C, b) 23 °C, c) 24 °C, d) 25 °C, e) 26 °C, f) 27 °C, and g) 28 °C.

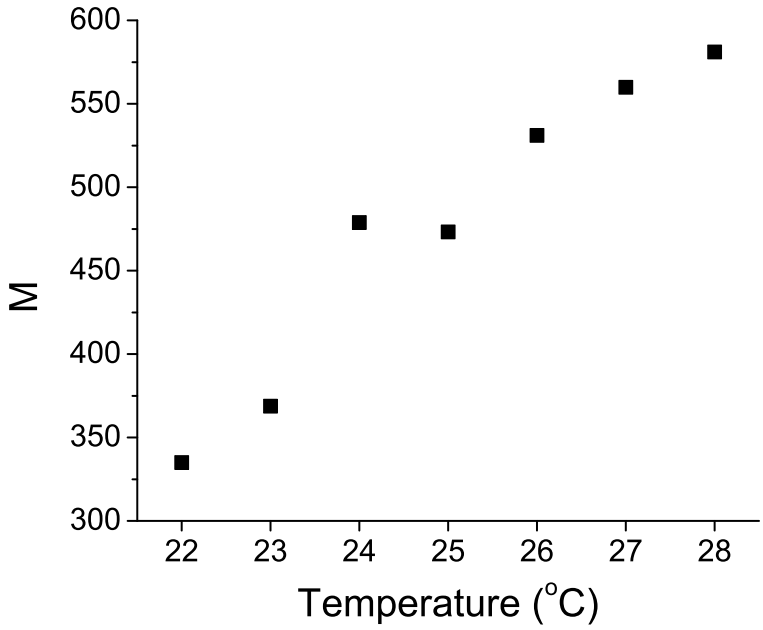

Figure 3.14: Decay constant M as function of temperature.

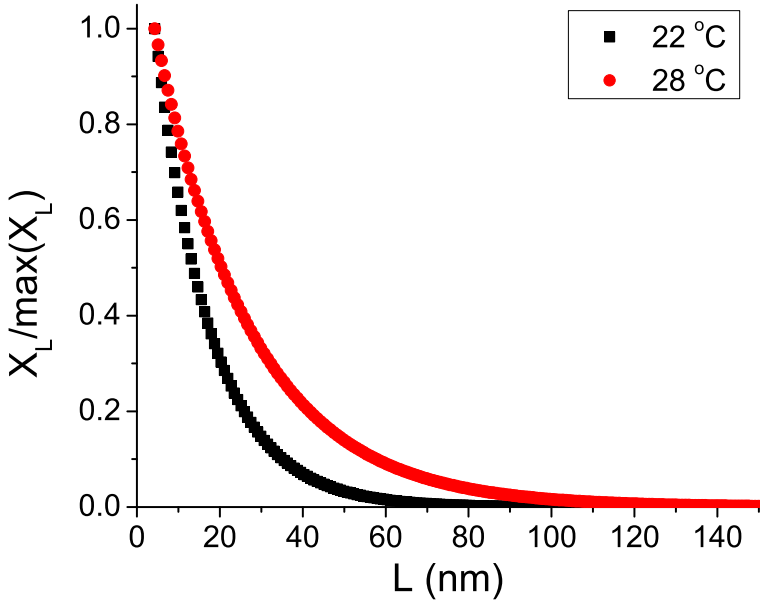

Figure 3.15: Scaled size distributions, $X_L/\max(X_L)$, as function of micelle length, L, at temperatures 22 ^{o}C (black squares) and 28 ^{o}C.

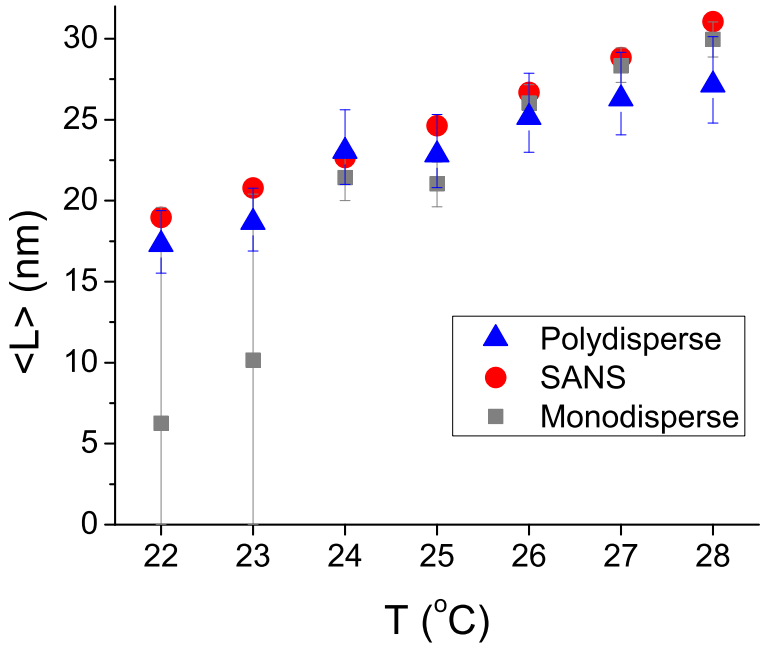

Figure 3.16: Average length, $\langle L \rangle$, of the surfactant micelles extracted from interaction potentials using the polydisperse model (blue triangles), the monodisperse model (grey squares), and as measured by small angle neutron scattering (SANS) (red circles) in ref. [3] versus temperature T.

values of M, and thus average lengths, $\langle L \rangle$, that resulted in the potential minima of the theoretical functions and experimental data being equal. The $\langle L \rangle$ that yield the same potential minima as the experimental data are shown in Figure 3.17 along with all other measured lengths. We found that the $\langle L \rangle$ needed to have the potential minima be equal were slightly larger (approximately 1 nm) than the $\langle L \rangle$ calculated from the fits. We did observe however that in forcing the theoretical potentials to have the same minima as the experimental data, location of the minima was shifted to larger r and the potentials wells were wider than the wells studied in experiment (see Figure 3.18 for exemplary curves).

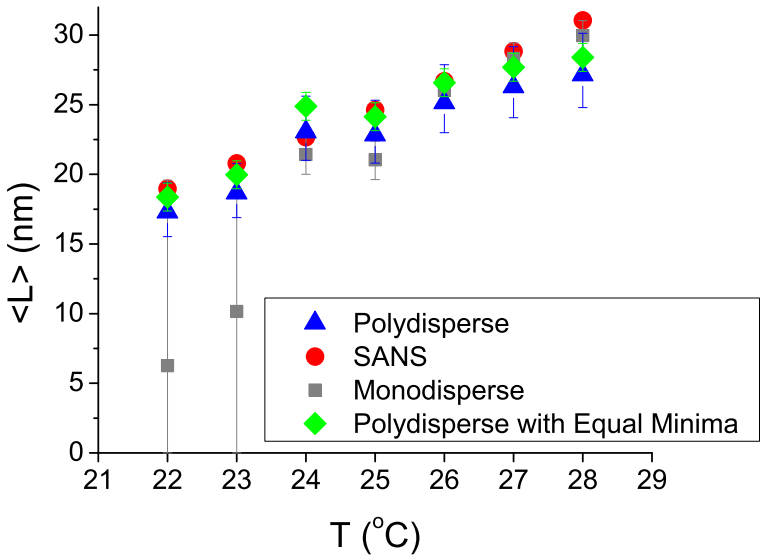

Figure 3.17: Average length, $\langle L \rangle$, of the surfactant micelles that result in the calculated potential minimum being equal to the experimental potential minimum (green diamonds), extracted from interaction potentials using the polydisperse model (blue triangles), the monodisperse model (grey squares), and as measured by small angle neutron scattering (SANS) (red circles) in ref. [3] versus temperature T.

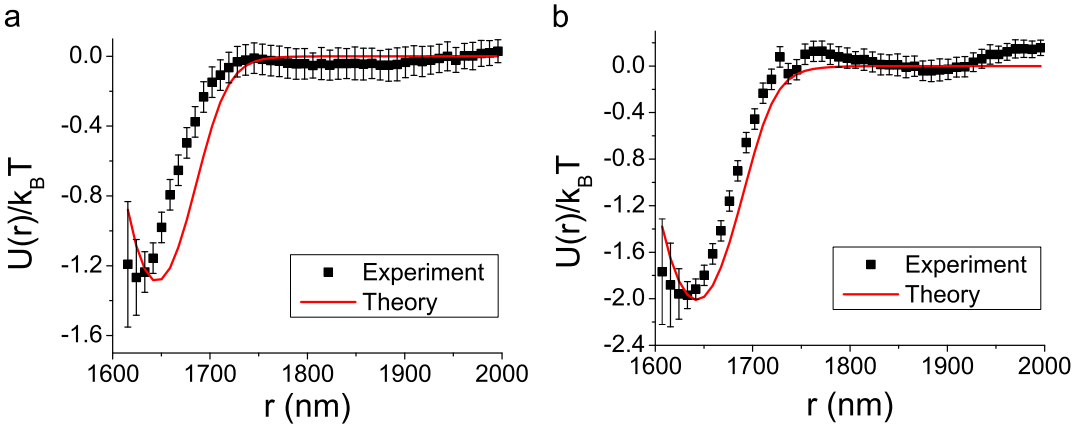

Figure 3.18: Measured depletion interaction potentials (black squares) and theoretical potentials calculated using polydisperse rod depletant model (red lines) such that potential minima of two curves are equal for temperatures a) $24\ ^{o}$C and b) $28\ ^{o}$C.

3.5.4 Lengths Extracted Without Screening Length

There is some debate as to whether the use of the Debye screening length, κ^{-1}, should be used in the fitting procedures, described earlier, to extract the lengths of $C_{12}E_6$ surfactant micelles. $C_{12}E_6$ is a nonionic surfactant, *i.e.*, have a net charge equal to zero. Interestingly, the assignment of zero charge to the C12E6 nonionic surfactant (and surfactant micelle) is currently debated. We explored this issue in the literature and with colleagues, and it seems that considerable evidence has been gathered to support the notion that the ethylene oxide groups of the C12E6 surfactant micelles can acquire charge due in the presence of salt [173–175]. In such cases, the micelles acquire charge that would be screened in solution. Thus, we chose to incorporate the screening length, κ^{-1}, in our initial calculations, and used effective dimensions, $L' = L + 2\kappa^{-1}$ and $D' = D + 2\kappa^{-1}$, as discussed previously. Nevertheless, because of this controversy, we carried out the fitting procedures for both the monodisperse model (Equation 3.1) and polydisperse model (Equation 3.8) using the bare dimensions L and D, instead of the effective dimensions, L' and D'. See Figure 3.19 and Figure 3.20 for the fits of the monodisperse model and polydisperse model, respectively, wherein the bare dimensions were used in the fitting procedure. Remember that the cross-sectional diameter, D, is 4.3 nm [3] and held fixed during the fitting process.

We observe that with both the monodisperse model and polydisperse model (Figure 3.21), the extracted average micelle lengths, $\langle L \rangle$, increased with sample temperature, while the cross-sectional diameter, D, remained constant. Therefore, the increase in attraction strength between colloidal particles measured here is still due to an increase micelle shape anisotropy. The lengths extracted using the bare dimensions, L and D, were not in as good agreement with the lengths

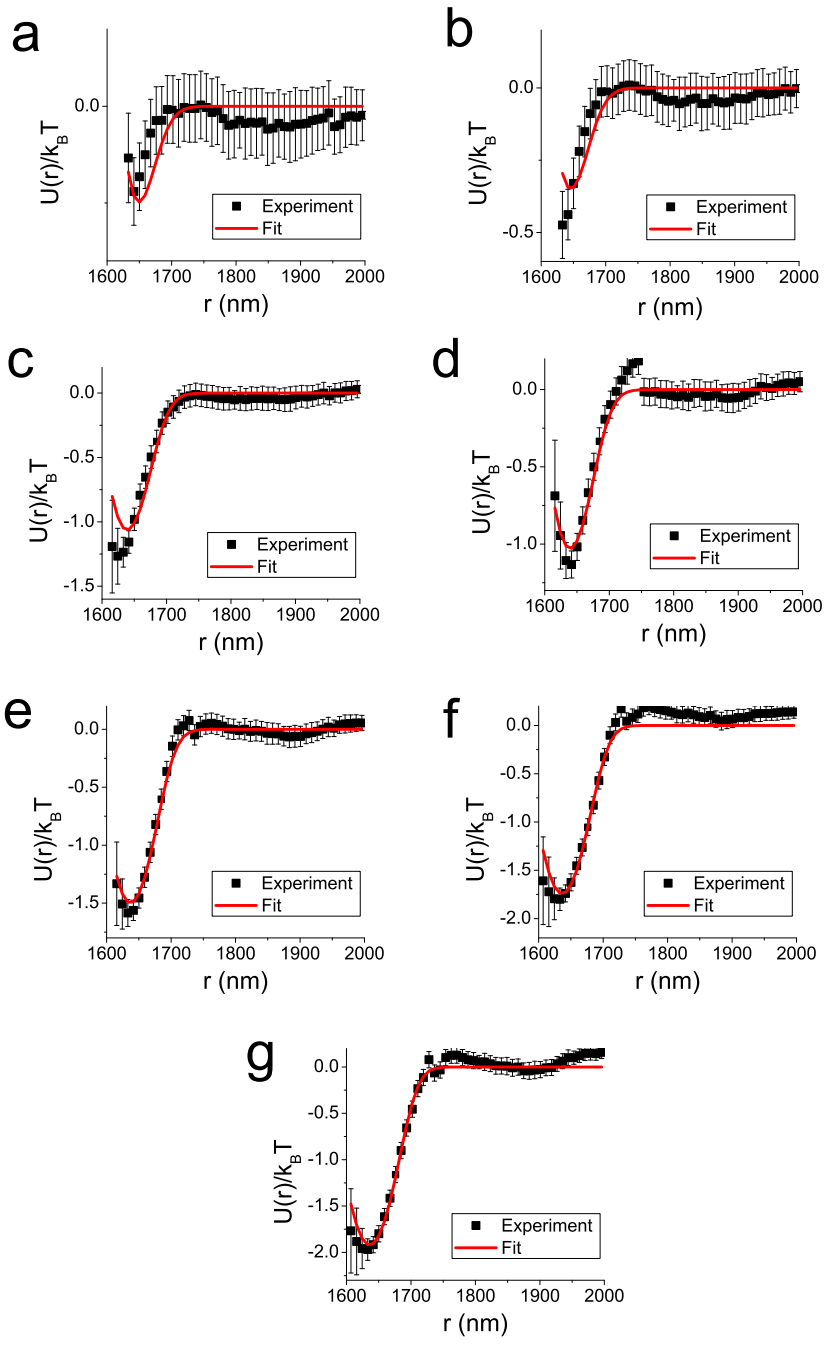

Figure 3.19: Experimentally measured interparticle potentials $U(r)/k_BT$ (black squares) and fits from the theoretical function for a monodisperse suspension of ellipsoidal depletants using the bare dimensions, L and D, (red lines) for all temperatures. a) 22 °C, b) 23 °C, c) 24 °C, d) 25 °C, e) 26 °C, f) 27 °C, and g) 28 °C.

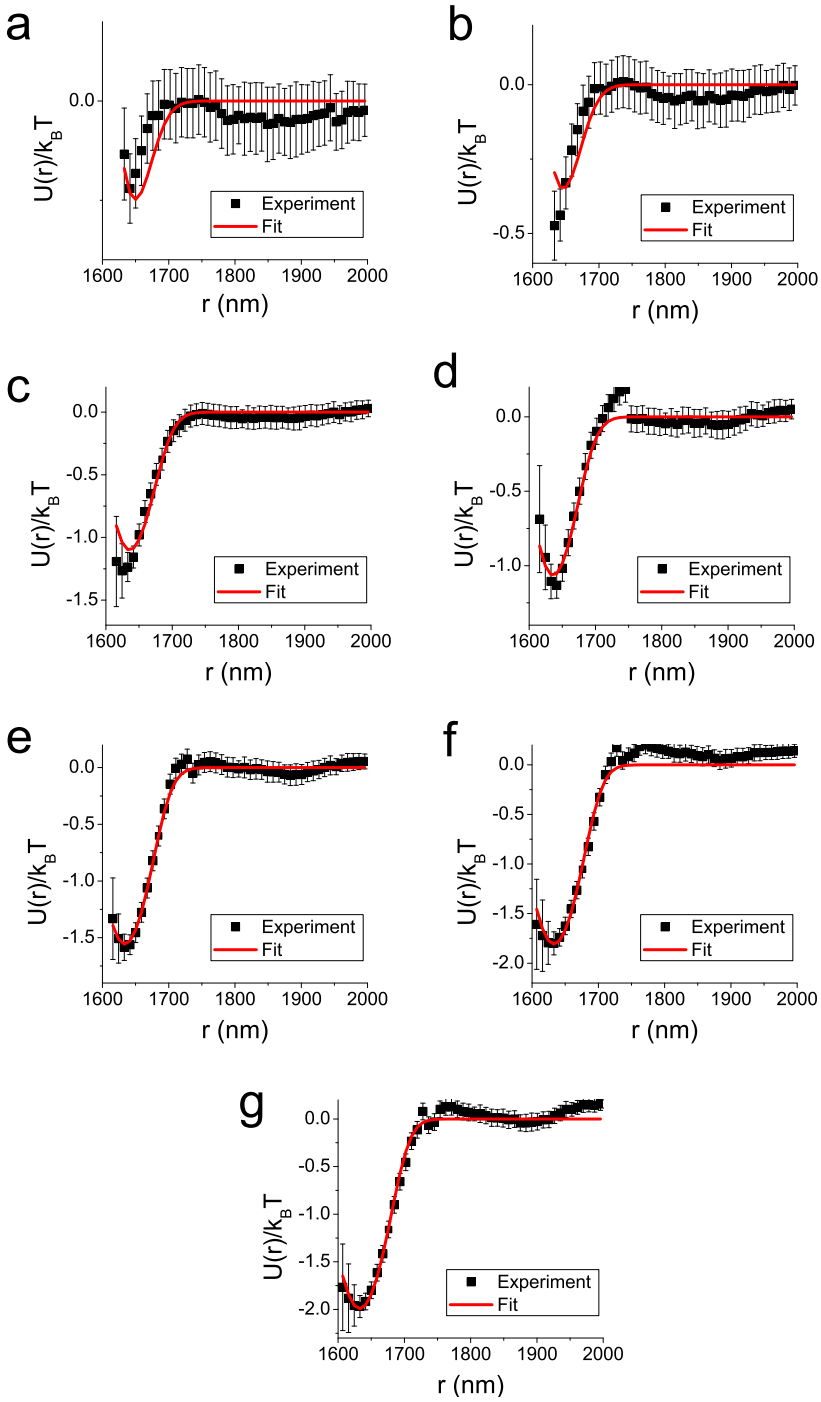

Figure 3.20: Experimentally measured interparticle potentials $U(r)/k_BT$ (black squares) and fits from the theoretical function for a polydisperse suspension of ellipsoidal depletants using the bare dimensions, L and D, (red lines) for all temperatures. a) 22 °C, b) 23 °C, c) 24 °C, d) 25 °C, e) 26 °C, f) 27 °C, and g) 28 °C.

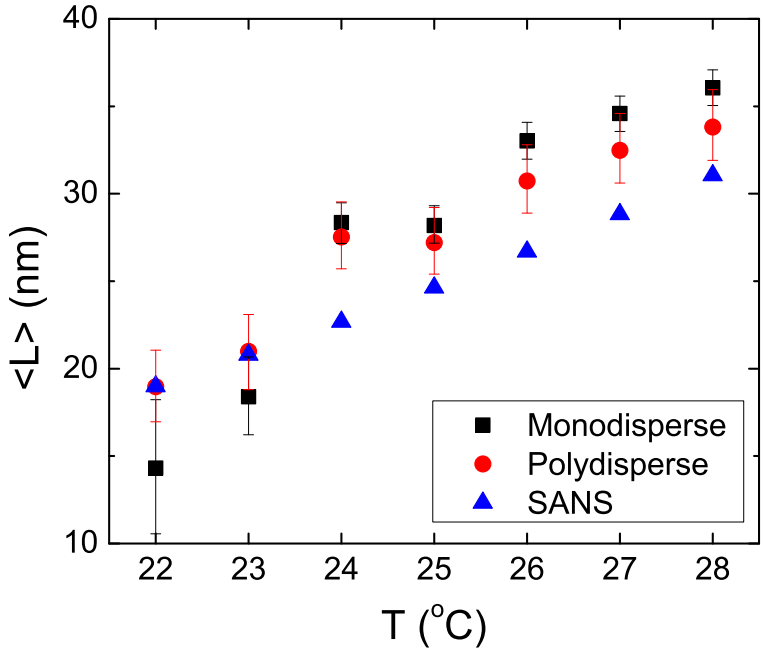

Figure 3.21: Average bare length, $\langle L \rangle$, of the surfactant micelles extracted from interaction potentials using the monodisperse model (black squares) and polydisperse model (red circles), without incorporating the Debye screening length, κ^{-1}, and as measured by small angle neutron scattering (SANS) (blue triangles) in ref. [3] versus temperature T.

measured by small angle neutron scattering (SANS) experiments compared to the lengths extracted when incorporating the Debye screening length. However, the main conclusion of this experiment, that the attraction strength between colloidal particles induced by $C_{12}E_6$ surfactant micelles increases due to an increase of the micelle shape anisotropy, remains true.

3.6 Conclusion

In summary, we measured the strength and range of the depletion attraction between colloidal particles induced by $C_{12}E_6$ surfactant micelles *in situ* as a function of temperature. We demonstrated that tuning shape anisotropy of these surfactant micelles facilitates modulation of this entropic attraction. Specifically, we showed that the increase in the measured strength and range

of the depletion attraction arises from an increase in the aspect ratio of the depletant micelles. This approach introduces a simple and useful tool for controlling interactions in suspension. We also independently measured the rod length and size distribution of $C_{12}E_6$ surfactant micelles as a function of temperature. The exact lengths of the micelles, as a function of temperature, depend upon whether there is a build up of charge on the surface of the surfactant micelles. Assuming there is a build up of charge on the surface of the micelles, and thus the screening length is important, the lengths measured are in good agreement with those reported in neutron scattering experiments. If there is no build up of charge on the surface of the micelles, then the lengths measured are smaller than those reported in neutron scattering experiments, but are still reasonable. Therefore, we demonstrated that measuring the depletion interaction between micron-size colloidal particles via the optical microscopy techniques presented here is a new method of measuring the size and shape of nano-scale macromolecule depletants.

3.7 Future Work

In situ modulation of colloidal attraction via shape anisotropy permits easy phase space exploration of the state diagram of colloidal glasses with attractive interparticle interactions. Most previous studies of the state diagram of colloidal glasses with attractive interparticle interactions controlled the strength of the interparticle attraction by making a large number of samples with various concentrations of depletant molecules [17, 30–34]. In the next chapter of this thesis, we show that utilizing $C_{12}E_6$ surfactant micelle depletants permits us to explore this phase space simply by changing the temperature of a single sample.

Use of this tunable depletion effect also potentially opens up a route to the self-assembly

of colloidal bigels, interpenetrating gel networks [176, 177]. Bigels could be formed in a bidispersed colloidal suspensions with $C_{12}E_6$ surfactant micelles using a two step process. First, the sample temperature is set low to permit large spheres to aggregate and form a gel network. Then, the sample temperature could be raised to permit small spheres to aggregate and form a second gel (or composite) network. Thus, two interpenetrating gel networks would exist: a large particle gel network and a small particle gel network.

Finally, this novel experimental method offers a qualitatively new and effective means to measure the size and shape of many types of depletant molecules in the nanoscale range. One interesting opportunity is to study depletion due to lyotropic chromonic liquid crystals [178–181] wherein the underlying plank-like macromolecules stack to produce rod-like mesogens which in turn assemble into liquid crystalline phases; the present method offers a novel way to measure the average length and length distribution of the stacks. In principle, the measurement also offers a tool to probe the size, shape, and folding of proteins.

Chapter 4

Phonon Behavior of Two-Dimensional Colloidal Glasses with Increasing Interparticle Attraction Strength

4.1 Introduction

Many properties of glasses, such as the Debye-Waller factor which is related to the mean-squared displacement, are predicted to depend on the interaction potential between the constituent particles [141–145]. In glasses with a high packing fraction, two states have been observed to depend on the strength of the short range attraction between constituent particles. Glasses with very weak interparticle attraction strength are commonly called “repulsive” glasses, and glasses

with strong interparticle attraction strength are commonly called “attractive” glasses. The internal particle dynamics in repulsive versus attractive glasses have been observed to be different [17, 19, 30, 32–34, 146]. These studies, however, have focused primarily on comparing the two limits, *i.e.*, glasses with no interparticle attraction (hard-spheres) and glasses with very strong interparticle attraction. Very little work, however, has been done to explore the transition in the properties of glasses as the interparticle attraction strength gradually increases from nearly hard-sphere to strongly attractive.

In this chapter, we describe experiments that explore the changes in the vibrational properties of colloidal glasses induced by changes in interparticle interactions. In particular, we study the vibrational phonons of quasi-2D colloidal glasses whose interparticle interactions are controlled via the temperature tunable depletion interaction developed and discussed in **Chapter 3**. This tunable attraction enables us to study the changes in the properties of a colloidal glass as the interparticle attraction strength is gradually increased from very weak (nearly hard-sphere) to very strong. We observed that particle dynamics slow monotonically with increasing attraction strength, and then saturate at a strong enough attraction strength. The shape of the phonon density of states are also revealed to change with increasing attraction strength. Specifically, comparatively more low-frequency modes were observed in glasses with weak attraction strength than those with strong attraction.

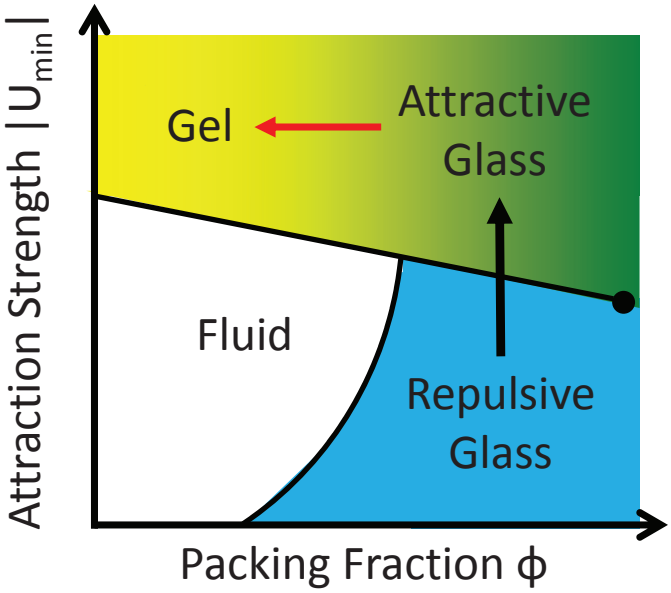

Figure 4.1: Qualitative "state" diagram for disordered glassy packings as a function of particle packing fraction, ϕ, and interparticle attraction strength, $|U_{min}|$. Black arrow represents direction in state diagram studied in these experiments. Red arrow represents direction studied in experiments by Lohr *et al* [4].

4.2 Contextual and Theoretical Background

4.2.1 Repulsive vs. Attractive Glasses

Mode coupling theory (MCT) has predicted that in densely packed glasses with short range interparticle attraction two distinct arrested states exist [5, 141, 182–184]: a "repulsive" glass when the interparticle attraction is weak and an "attractive" glass when the interparticle attraction is strong (see Figure 4.1). The prediction of these two states has been confirmed by experiment [30, 146, 185] and simulation [19, 143, 186, 187].

The differences in the properties of repulsive versus attractive glasses arise due to different mechanisms of dynamical arrest. In repulsive glasses, the particle dynamics slow due to local crowding, wherein particles are trapped in an entropic "cage" created by neighboring particles.

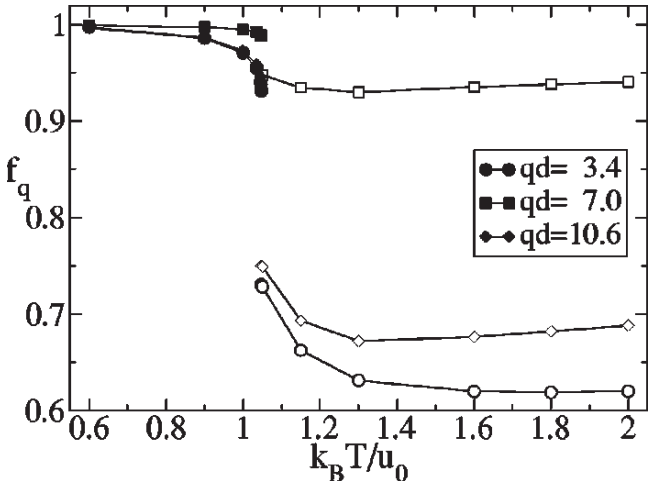

Figure 4.2: Debye-Waller factor f_q as function of reduced temperature k_BT/u_0 for various dimensionless wave vectors qd from ref. [5]. Here, u_0 is the potential well depth, q is the wave vector, and d is the particle diameter. Observe a discontinuous jump in f_q at the transition point $k_BT/u_0 = 1$.

In attractive glasses, local crowding is also present, but particle dynamics are slowed even further due to strong inter-particle attractive bonds. The dynamics in attractive glasses have also been observed to be heterogeneous over a larger range of length and time scales compared to repulsive glasses [146]. The cooperative rearrangement regions (CRRs) in repulsive glasses are string-like, while in attractive glasses CRRs are compact. The differences in dynamical arrest also lead to differences in bulk rheological properties, for example, two-step yielding in attractive glasses [31].

The transition from the repulsive glass state to the attractive glass state predicted by MCT [5, 141,182–184] was signified by discontinous jumps in various quantities with respect to attraction well depth. For example, Figure 4.2) shows the Debye-Waller factor f_q as a function of reduced temperature k_BT/u_0, where u_0 is the depth of the interparticle potential well, *i.e.*, attraction

strength.

The work presented in this chapter represents the first experiments to explore this transition, *i.e.*, to experimentally study the change in behavior of a glass as interparticle attraction strength gradually increases from very weak (repulsive) to very strong, or if there is a discontinous jump in the behavior at the transition as predicted by MCT. One of the goals of this work was to quantitatively define the attraction strength near the transition. Put more simply, our work seeks to discern what attraction strengths are "weak", leading to the repulsive glass state, and "strong", leading to the attractive glass state? Further, this work searched for quantities measured at the single-particle level that display the transition; what are these quantities and do these quantities change gradually or sharply around the transition point.

4.2.2 Low-Frequency Phonon Behavior of Disordered Solids

A discussion of the low frequency behavior of disordered (glassy) solids was presented in **Chapter 2** of this thesis. Here, we will give a brief overview of similar topics relevant for the results presented in this chapter, especially differences in low-frequency phonon behavior of attractive densely packed glasses compared to attractive sparsely packed gels.

In disordered solids, *e.g.*, glasses, an excess of low-frequency vibrational modes is typically found. This excess is not predicted by the Debye model, and is known as the "boson" peak [62]. This boson peak is observed as a "bump" at low frequencies when the vibrational Density of States ($DOS(\omega)$) is scaled by the expected Debye behavior, *i.e.*, $DOS(\omega)/\omega^{d-1}$, where d is the dimension (Figure 4.3). The presence and height of the boson peak has been previously used as an indicator of the glass transition [2, 188]. It has also been observed that these low-frequency modes in glasses are quasi-localized and display enhanced participation in regions

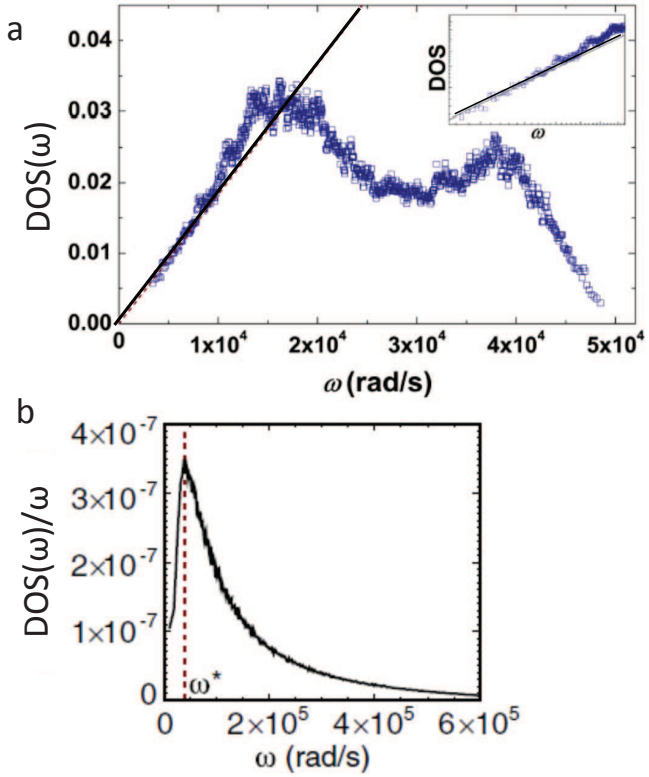

Figure 4.3: a) $DOS(\omega)$ for a 2D colloidal crystal at a liquid crystal-air interface reported in ref. [1]. Black line represents Debye prediction for 2D system, $DOS(\omega) \sim \omega$. Inset focuses on low frequency regime. Note this inset is in log-log scale with a slope equal to 1. Observe $DOS(\omega)$ follows Debye prediction at low frequencies. b) Density of states scaled by Debye predictions, $DOS(\omega)/\omega$, for a 2D colloidal glass reported in ref. [2]. The location of the Boson peak is represented by ω^*.

prone to rearrangements [2, 63–69].

The vibrational phonon mode distribution, namely $DOS(\omega)$, has also been shown to describe the cross over from the attractive glass state to the gel state, where more conventional order parameters had failed to distinctly describe the transition [4]. This previous work studied the vibrational phonons of disordered materials with a strong interparticle attraction that was held constant as a function of packing fraction, *i.e.*, moving from right to left in the upper part of the state diagram provided in Fig. 4.1 at strong attraction strength. It was observed that sparsely

packed gel-like states have an excess of low frequency modes compared to densely packed attractive glass states. This excess of modes arises largely from localized vibrations involving small clusters of particles. These results provide further motivation for the work presented herein. If the vibrational phonons could describe the transition from the densely packed attractive glass state to the sparsely packed gel state, something traditional order parameters had failed to do, then perhaps the study of vibrational phonons will provide insight into the attractive to repulsive glass transition that is not accessible via studies of traditional structural and dynamical properties.

4.3 Experimental and Analytical Methods

4.3.1 Experimental Materials

Samples are composed of silica spheres at a volume fraction of approximately, $\phi = 0.1$, suspended in a solution of 44 mM hexaethylene glycol monododecyl ether ($C_{12}E_6$) and 17 mM NaCl in water. The colloidal particles used were silica spheres with diameters 1.57 μm and 1.2 μm (a size ratio $\approx$ 1.3). The number ratio of the two sizes in suspension was set to be $1:1$. The size ratio and number ratio in the samples helped to insure that crystallization is frustrated [72, 189, 190], and thus a geometrically disordered glass formed. Note, initially the colloidal volume fraction in the sample is relatively dilute. However, as the next section will explain, gravity is used to create dense 2D colloidal glasses which we study.

Attraction between the constituent colloidal particles was achieved using the depletion interaction induced by the suspension of $C_{12}E_6$ surfactant micelles. As discussed in detail in **Chapter 3**, the depletion interaction is an entropic force between colloidal particles that arises

when small non-adsorbing particles, known as depletants, are added to the suspension. We showed that the use of $C_{12}E_6$ micelles as depletants provides a temperature tunable depletion interaction; wherein the strength of the interparticle attraction increases as sample temperature is increased.

Note, the concentrations of $C_{12}E_6$ and NaCl used in these experiments are the same used in the depletion experiments described in **Chapter 3**. At these concentrations, the attraction strength, $|U_{min}|$, defined as the depth of the potential well, was measured to be small ($< 1k_BT$), *i.e.*, nearly hard-sphere, at temperatures below $24\ ^oC$. It increased monotonically with temperature. Therefore, to experimentally study a colloidal glass at various attraction strengths, we did not need to make a large number of samples with various depletant concentrations as has been done in previous experiments. Instead, a single sample was made, and the interparticle attraction strength was varied via control of the sample temperature using a Bioptechs objective heater. In the end, we studied a densely packed colloidal glass with constant packing fraction, $\phi = 0.82$, and the interparticle attraction strengths ranged from nearly hard-sphere repulsive (weak attraction) to strongly attractive.

4.3.2 Preparation of Wedge Cells

Creating densely packed quasi-2D colloidal glasses with the above mentioned temperature tunable depletants proved to be a difficult endeavor. Due to the sample's high viscosity, simply sandwiching the sample solution between a glass slide and glass coverslip, as done in many of our group's previous experiments, did not yield 2D domains. Thus, another means of sample preparation was required.

For experiments presented herein, we found that the use of wedge cells provided a means

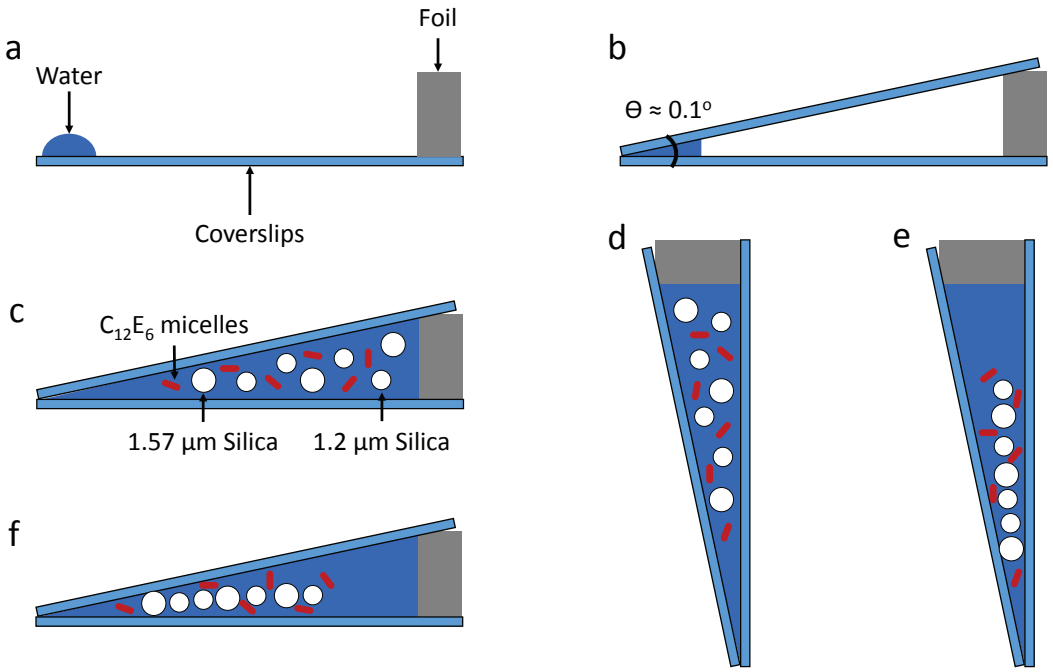

Figure 4.4: Diagram of wedge cell construction. Drawings are not to scale. a) On a cleaned 22 mm by 50 mm microscope coverslip, a small drop of water is placed on one end, while a piece of aluminum foil is placed on the other end of the coverslip. b) A second cleaned coverslip is then pressed against the first coverslip such that the water spreads as much as possible. c) The sample cell is loaded with the sample material from the foil side, and sealed with UV glue. Here the sample is a bidispersed suspension of 1.57 μm and 1.2 μm silica spheres in a suspension of $C_{12}E_6$ surfactant micelles. d) After the glue has fully cured (4-6 hours), the sample is tilted upright with the thin end pointing downward. e) After 2-3 days, the colloidal particles have sedimented to the thin end and are packed in a dense quasi-2D packing. f) The wedge cell is then left to lie flat for 24 hours. After which the sample is ready to be imaged.

of repeatably creating large quasi-2D domains (> 8 mm^2 in area) of densely packed colloid. Further, the samples did not alter the temperature tunability of the depletion interaction. The wedge cells were constructed using a procedure adapted from the procedure used by Gerbode *et al* [191]. A diagram of the procedure is presented in Figure 4.4, and explained in detail below.

First, two 22 mm by 50 mm coverslips (Fisher Scientific) were dipped in ethanol to form a thin coating of the ethanol on the surface of each coverslip. The ethanol coated coverslips

were then passed through a flame from a Bunsen burner. This burned off the ethanol coating as well as the coating the manufacturer uses to prevent the coverslips from sticking together. Removing the manufacturer's coating prevents the colloidal particles from sticking to the sample cell walls when the depletion force is strong, and it also makes the coverslips hydrophilic. Both of these effects are necessary for my experiments. If particles become immobile at high attraction strength then we cannot study their vibrational properties. The hydrophilicity is also necessary for the next step in the cell construction.

Next, a very small drop of water (≤ 0.2 μL) is placed at one end of one of the coverslips. A small piece of aluminum foil is then placed at the other end. The foil used in these experiments was measured to have a thickness of 12.5 μm. The two coverslips are then pressed together. The water droplet on the one end of the coverlsip spreads, creating a seal, and acting as a tiny spacer between the two coverslips. A rough calculation based on the volume of the water droplet and the area covered after the droplet had spread suggested the height/separation between the coverslips at this end of the cell, referred to here as the "thin end", was less than 1 μm. At the other end of the cell, where the piece of foil acts as a spacer, the seperation between the two coverslips is not smaller than the thickness of the foil (12.5 μm). The foil end of the chamber is referred to as the "wide end". Thus, we create a chamber whose thickness increases from below 1 μm to 12.5 μm over a distance of 50 mm, or in other words, a wedge with an angle approximately equal to 0.1 degrees.

The sample solution was then loaded into the chamber with a pipette at the wide end of the chamber. By using a dilute suspension of colloids to start, the sample solution easily flows into the sample cell. The sample cell is sealed and glued to a microscope slide using UV optical

glue (Norland Optics), and left under a UV lamp for $4-6$ hours to ensure the glue is cured completely. This is necessary as the following steps take $4-5$ days and the samples need to be as air tight as possible to avoid evaporation over this time period.

Once the glue has cured, the samples are then tilted upright such that the thin end of the cells are pointed down and left for $2-3$. Then, gravity does the work for us. The colloidal particles sediment to the thin end of the sample cell. After $2-3$ days, most of the particles have packed tightly at the thin end of the chamber. The samples cells are then laid flat on the work bench over night to allow the sample to equilibrate. The next morning the sample cell is placed on the microscope for imaging.

There is a large region (> 8 mm^2) near the thin end of the cell such that the thickness of the cell is approximately 1.1 times the particle diameter. In this region the sample is quasi-2D and densely packed (Figure 4.5). The angle of the wedge is shallow enough that over the field of view (60 μm by 60 μm), and the cell walls are effectively parallel. As one moves to regions where the cell thickness increases above 1.1 times the particle diameter, but still near the thin end of the sample cell, densely packed multilayered region is observed as well (shown on right hand side of cartoon in Fig. 4.5). On the other side of this densely packed multilayered regions, which is the thick end of the wedge cells, is an extremely dilute colloidal fluid. However, only the quasi-2D domain of the sample is studied.

4.3.3 The Depletion Interaction in Wedge Cell Chambers

The use of these wedge cells, as well as the use of the same depletant and salt concentrations as discussed in **Chapter 3**, also allow us to approximate the value of the interparticle potential well depth, $|U_{min}|$, *i.e.*, attraction strength, as a function of temperature, to be equivalent to the values

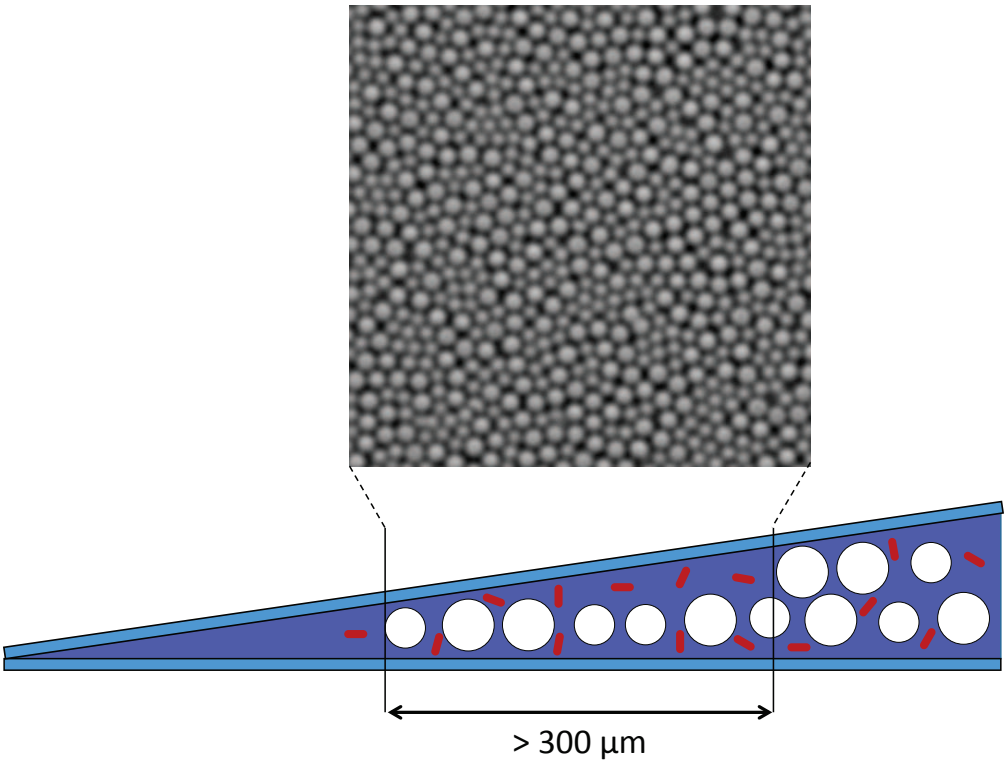

Figure 4.5: Cartoon representation of wedge cell with experimental image of quasi-2D dense colloidal glass. The angle of wedge cell is shallow enough such that over a distance of larger than 400 μm, the sample is quasi-2D and the top and bottom walls are effectively parallel. Drawings not to scale.

presented in **Chapter 3**. We make these approximations using osmotic pressure arguments in the ideal gas limit, as well as using the Carnahan-Starling equation of state [192].

The densely packed multilayered region mentioned above acts as a semipermeable membrane between the densely packed quasi-2D region, the region we are interested in studying, and the dilute colloidal fluid. The depletant molecules can pass through the membrane and the colloidal particles cannot. Our system is thus analogous to the system in the traditional osmotic pressure problem, where two compartments are separated by a semipermeable membrane. The

pressure of the two sides of our semipermeable membrane must be equal. For the following arguments, we denote the side of the membrane consisting of the colloidal fluid as $compartment\ 1$, and all quantities associated with $compartment\ 1$ with a subscript 1, and the densely packed quasi-2D region as $compartment\ 2$, and all associated quantities with a subscript 2.

We first look at $compartment\ 1$, the dilute colloidal fluid. Here, because the concentration of $C_{12}E_6$ depletants and colloidal particles is the same as in the experiments presented in **Chapter 3**, the depletion interactions on this side are the same as those measured in **Chapter 3**. The (3D) colloidal particle volume fraction, $\rho_{spheres,1} << 0.1$, is negligible compared to the volume fraction of the depletants, $\rho_{depl,1} = 0.2$. Note, here we use ρ to denote *3D volume fractions* instead of the more commonly used ϕ because we have previously defined ϕ as *2D area fractions*. The pressure of $compartment\ 1$, P_1, is dominated by the pressure of the depletants, $P_{depl,1}$, on that side of the semipermeable membrane, $i.e.$, $P_1 = P_{depl,1}$, because of low the colloidal volume fraction is. The depletants are treated as ideal gas, and thus the pressure $P_1 = n_{depl,1} k_B T / V_1$, where $n_{depl,1}$ is the number of depletants in $compartment\ 1$ and V_1 is the total volume of $compartment\ 1$. We next define the free volume accessible to the depletants, $V_{free,1} = V_1 - V_{spheres,1}$, where $V_{spheres,1}$ is the total volume of the colloidal particles in $compartment\ 1$. The total volume of the colloidal particles is negligible compared to the total volume of the compartment, and therefore $V_{free,1} \approx V_1$. Remember, the volume fraction of the depletants in this compartment is the same as in the experiments in **Chapter 3**, and therefore the number density of depletants from the previous depletion experiments, n/V, is equal to the number density of depletants in $compartment\ 1$, $n_1/V_{free,1}$. Knowing the volume fraction, ρ, and dimensions of rod-shaped depletants (length L and cross-sectional diameter D) the pressure

in $compartment\ 1$ can be written as $P_1 = 4\rho k_B T/\pi D^2 L$. Using reasonable approximations for the average size/dimensions of the (rod-shaped) $C_{12}E_6$ micelle depletants (based off the results from **Chapter 3**), for example a length $L = 20$ nm and diameter $D = 4$ nm, and knowing the depletant volume fraction $\rho = 0.2$, we calculate $P_1 \approx 8 \times 10^{-5}\ k_B T$ nm^{-3}.

Next, we look at the densely packed quasi-2D region, $compartment\ 2$, wherein the colloidal particle volume fraction, $\rho_{spheres,2}$, is no longer negligible. The pressure of $compartment\ 2$, P_2, is the sum of the pressures from the depletants, $P_{depl,2}$, and the colloidal particles, $P_{spheres,2}$, $i.e.$, $P_2 = P_{depl,2} + P_{spheres,2}$. The pressure of the two compartments must be equal, therefore:

$$P_{depl,2} + P_{spheres,2} = P_1 = \frac{n}{V} k_B T \approx \frac{n_{depl,1}}{V_{free,1}} \approx 8 \times 10^{-5}\ k_B T\ \ nm^{-3}, \tag{4.1}$$

where P_1 is the pressure of $compartment\ 1$, n/V is the number density of depletants from the experiments **Chapter 3**, and $n_{depl,1}/V_{free,1}$ is the number density of depletants in the free volume accessible to depletants in $compartment\ 1$ ($n_{depl,1}/V_{free,1} = n/V$, as shown in the previous paragraph). In the densely packed quasi-2D region, the colloidal particle volume fraction $\rho_{sphere,2} \approx 0.5$. At this volume fraction, we cannot treat the colloidal particles as an ideal gas, but we can approximate the pressure using the Carnahan-Starling equation of state, $P_{spheres,2} = Z n_{spheres,2} k_B T/V_2$, where $n_{spheres,2}$ is the number of colloidal particles in $compartment\ 2$, V_2 is the total volume of $compartment\ 2$, and Z is the compressibility factor defined as:

$$Z = \frac{1 + \rho_{spheres,2} + \rho_{spheres,2}^2 - \rho_{spheres,2}^3}{\left(1 - \rho_{spheres,2}\right)^3}. \tag{4.2}$$

The colloidal particle number density in $compartment\ 2$, $n_{spheres,2}/V_2 = 2.45 \times 10^{-10}$, and

volume fraction $\rho_{sphere,2} \approx 0.5$ yields a pressure of $P_{spheres,2} \approx 3.2 \times 10^{-9}\ k_BT$ nm^{-3}. Looking back to Equation 4.1, we see $P_{spheres,2}$ is 4 orders of magnitude smaller than the pressure of $compartment\ 1$, $P_1 \approx 8 \times 10^{-5}\ k_BT$ nm^{-3},and is thus negligible. Therefore, the pressure of $compartment\ 2$ must be dominated by the pressure of the depletants, $P_{depl,2}$, and so $P_{depl,2} \approx P_1$.

In $compartment\ 2$ (the densely packed quasi-2D region), the pressure of the depletants, $P_{depl,2} = n_2 k_B T / V_{free,2}$ [93], where n_2 is the number of depletants and $V_{free,2}$ is the free volume accessible to the depletants in $compartment\ 2$. We define the free volume accessible to the depletants in $compartment\ 2$ similarly to the definition of the free volume in $compartment\ 1$. Specifically, $V_{free,2} = V_2 - V_{spheres,2}$, where V_2 is the total volume of $compartment\ 2$ and $V_{spheres,2}$ is the volume of colloidal particles in $compartment\ 2$. We can now rewrite Equation 4.1:

$$\frac{n_{depl,2}}{V_{free,2}} k_B T = \frac{n_{depl,1}}{V_{free,1}} k_B T = \frac{n}{V} k_B T. \tag{4.3}$$

Finally, after the temperature terms cancel, we find the number density of depletants in the accessible free volume of $compartment\ 2$, $n_{depl,2}/V_{free,2}$, is equal to the number density of depletants from the experiments in **Chapter 3**. Therefore, the strength of the attractive depletion interaction, $|U_{min}|$, as a function of temperature, between colloidal particles in the densely packed quasi-2D region we study should be equal to the attraction strengths measured in **Chapter 3**.

4.3.4 Image Recording and Particle Tracking

Particle motion was recorded using video microscopy. Bright-field microscopy video was recorded at 100 frames per second for $100,000$ frames. Videos were taken at 12 sample temperatures ranging from 23 °C to 35 °C in 1 °C steps. The sample temperature was controlled using an objective heater (Bioptechs) connected to the microscope oil immersion objective. Subpixel particle tracking algorithms were employed to find positions of the $N_{tot} \approx 1700$ particles in each frame of the videos [87].

4.3.5 Correcting for Oscillatory Noise

Long wavelength oscillations were observed in the individual particle displacements due to very small temperature fluctuations from the objective heater. A sample of a single particle's displacement from the average position, $u_i(t)$ as a function of time is provided in Figure 4.6a. In this figure, the long wavelength oscillations are clearly observable. These long wavelength oscillations are not part of the Brownian motion of the particles. They had to first be removed before the the data could be properly analyzed.

To remove these oscillations, Fourier analysis was utilized to find the specific frequencies at which the objective heater was oscillating, and a Fourier filter was implemented to remove those frequencies. First, the Fourier signal, $f_i(q)$, of the displacements from the equilibrium position for each particle in each dimension was calculated (Fig. 4.6b), where q is the Fourier frequency and $i = [1, 2, ..., 2N_{tot}]$ is the indices representing each particle in each dimension. Then, the power spectrum of each $f_i(q)$, $|f_i(q)|^2$, was calculated and averaged over all i, $I(q)$. In Fig. 4.6d, an example of one such $I(q)$ is provided. Notice there is a large peak near the zero frequency

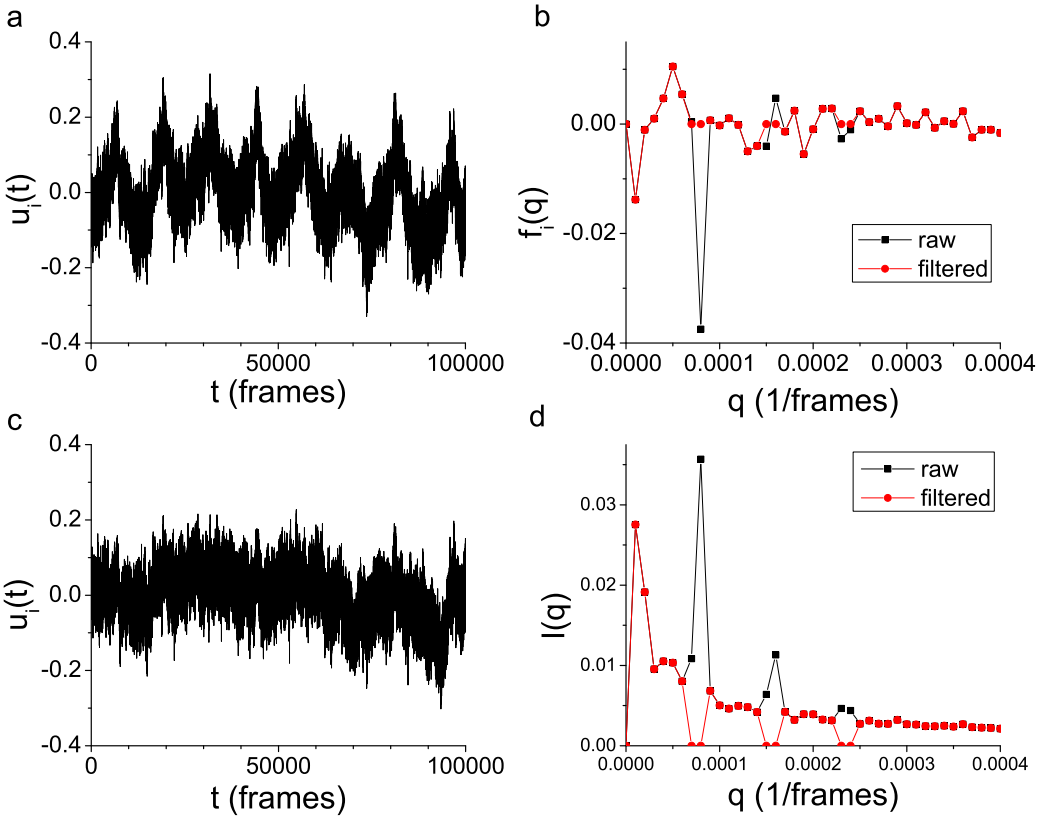

Figure 4.6: a) Displacement from the equilibrium position, $u_i(t)$, for a single particle in the 32 ^{o}C data set. b) Fourier signal, $f_i(q)$, of the displacement in a) before (black squares) and after (red circles) Fourier filter procedure. c) Fourier filtered displacement from equilibrium position. d) Power spectrum, $I(q)$, of Fourier signal in b) before (black squares) and after (red circles) filtering.

which is due to the finite time of the data, but there are other distinct peaks at slightly larger q that are from the long wavelength noise observed in the particle displacements. It is these peaks that are larger than the zero frequency peak that must be removed.

To filter those peaks out, one need only find the frequency at which the first peak occurs, we call this frequency q^*, as all other peaks are at integer multiples of q^*. The Fourier signal was set to zero for frequencies between $nq^* - \delta$ and $nq^* + \delta$, where δ is an integer value selected manually such that the entire peak is set to zero, and $n = 1, 2, 3, ...$ is an integer representing the

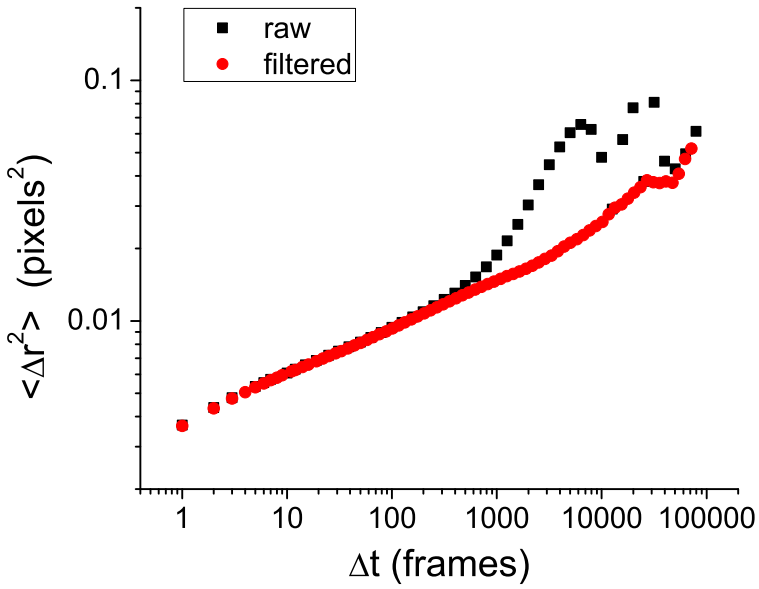

Figure 4.7: Mean-squared displacement, $\langle \Delta r^2 \rangle$, of 32 ^{o}C data set versus lag time Δt before (black squares) and after (red circles) Fourier filtering procedure.

integer multiple of q^* for the higher frequency peaks that are to be removed. Figure 4.6b shows an exemplary fourier signal before and after filtering for the displacement presented in Fig. 4.6a, and Fig. 4.6d shows the power spectra of the raw signal and the filtered signal.

Finally, an inverse Fourier transform is performed on the filtered Fourier signal of each particle and each direction. The real part of the inverse Fourier signals are the real particle displacements without the long wavelength oscillations caused by the objective heater, and thus are the displacements used in the measurements and calculations presented. Figure 4.6c shows the displacement presented in Fig. 4.6a after filtering.

An exemplary mean-squared displacement, $\langle \Delta r^2 \rangle$, versus lag time, δt, is presented in Figure 4.7. It is apparent that this filtering does not significantly alter the the overall motion in the sample; it just removes the underlying oscillitory noise.

4.3.6 Vibrational Phonons Calculated from Particle Trajectories and Accounting for Finite Sampling

The vibrational phonons were calculated from particle trajectories, and finite sample effects were corrected, using the same techniques discussed in **Chapter 2** of this thesis. The accumulated mode number $N(\omega)$ is defined as the number of modes with frequency $\leq \omega$. The density of states $DOS(\omega)$ is defined as the derivative of $N(\omega)$ with respect to ω, $dN(\omega)/d\omega$. Equivalently, we can say the $DOS(\omega)$ is the number of modes in the frequency range, or bin, $[\omega, \omega + d\omega]$ divided by $d\omega$. Commonly, the $DOS(\omega)$ is calculated using a constant $d\omega$, which is very similar to calculating the histogram of modes. Here we compensate for varying statistics at different frequency ranges by allowing $d\omega$ to vary, but keeping the number of modes per bin, *i.e.*, dN, constant. The $DOS(\omega)$ was then calculated from $dN = M$ consecutive modes, where M is an intereger, in the frequency range $[\omega_j, \omega_{j+M}]$. The density of states is then defined as $DOS(\omega_j) = M/(\omega_{j+M} - \omega_j)$.

4.4 Results and Discussion

4.4.1 Structural Characterization

To check if any structural changes arise as the temperature/attraction strength increases, the pair correlation function, $g(r)$, was calculated for all temperatures studied. The $g(r)$ for a subset of the temperatures are provided in Figure 4.8. All data presents behavior commonly observed in a glass of a bidispersed colloid suspension. Specifically, 3 nearest neighbor peaks arising from small-small, small-big, and big-small particle bonds are observed. We find no changes in $g(r)$

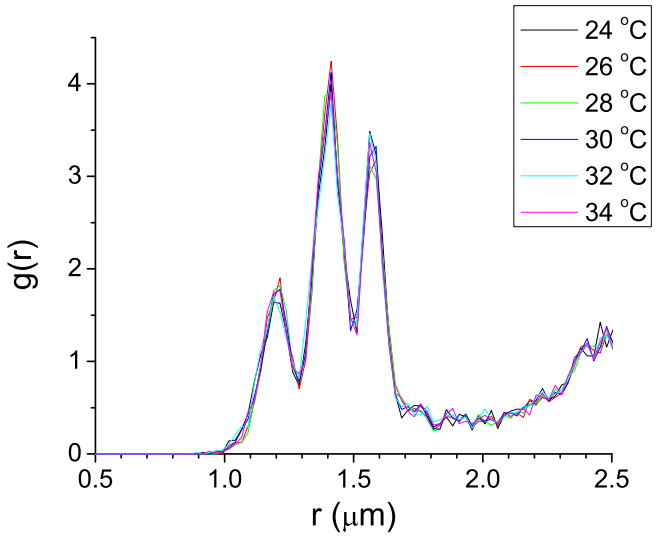

Figure 4.8: Pair correlation function, $g(r)$, for a representative subset of temperatures (24 ^{o}C, 26 ^{o}C, 28 ^{o}C, 30 ^{o}C, 32 ^{o}C, and 34 ^{o}C).

as the strength of the interparticle attraction varies, and so evidence of the repulsive glass to attractive glass transition is not present (within our signal-to-noise) in the structural properties of the system. Therefore, we turn to the vibrational and dynamical properties to shed light on this transition. Note that in **Chapter 3** we presented a method of measuring the interparticle attraction from $g(r)$, however this was only possible because that experiment was done in the dilute colloid packing fraction limit. In this experiment the colloids are packed to nearly their maximum packing fraction. Therefore, the structure is dominated by the entropy of particle packing and not by the interparticle interactions [26, 76].

4.4.2 Particle Dynamics

The particles dynamics at all temperatures are highly arrested (Figure 4.9), displaying a plateau in the mean-squared displacements (MSD), $\left\langle \Delta r^2 \right\rangle$. This plateau is a classic feature of colloidal glasses [19, 78, 146, 193–195], which arises from the particles exploring "cages" formed by their

neighbors. Note that the upturn commonly seen in glasses at long lag times is not observed because no rearrangements are observed during the chosen experimental time interval in order to insure the vibrational phonons can be calculated. To observe rearrangements, as well as to measure other traditional dynamical quantities such as the four point susceptibility, χ_4, a longer time interval is needed. However, information about the particle dynamics can still be ascertained with the time interval studied here.

We observed that the MSD monotonically decreases with increasing temperature/attraction strength. To more clearly observe this, we plot the MSD for a given lag time (21.8 seconds) as a function of temperature, T (Fig. 4.9b). We also provide the attraction strengths, $|U_{min}|$, measured in the previous chapter, and extrapolate to higher temperatures, on the upper x-axis. It is expected that the dynamics are slow at the higher attraction strengths since the particles are arrested by both their cage and nearest neighbor bonds. At weaker attraction strengths the motion is arrested primarily due to caging. We observe that while the MSD decreases monotonically with increasing attraction strength, it does not decrease linearly. Specifically, we observe what appears to be a saturation in the slowing of the dynamics at strong interparticle attraction strengths, and this saturation appears to begin when the attraction is between $1.5k_BT$ and $2k_BT$.

This saturation of the dynamics suggests the presence of a transition. However, we do not see a discontinous jump in the MSD as a function of attraction strength, as was observed in the Debye-Waller factor calculated by MCT. To further explore, and hopefully define, the transition from the repulsive glass state to the attractive glass state, we calculated the vibrational phonon modes.

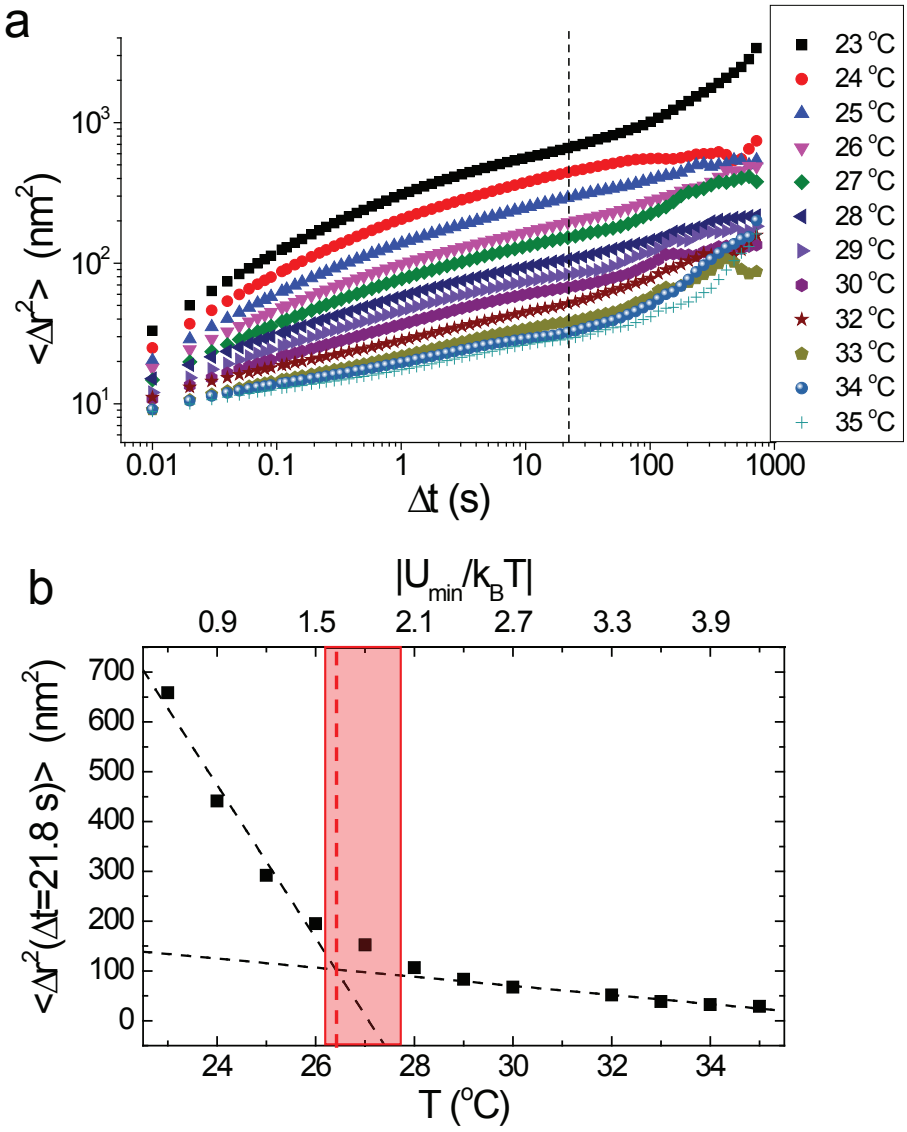

Figure 4.9: a) Mean-squared displacement, $\langle \Delta r^2 \rangle$, for all temperatures studied. Dashed line represents lag time $\Delta = 21.8$ seconds. b) $\langle \Delta r^2 \rangle$ for $\Delta t = 21.8$ seconds of all temperatures, T, studied. Top x-axis is $|U_{min}/k_B T|$ measured in depletion experiments explained in previous chapter. Black dashed lines are linear fits to the two regimes (monotonic decrease and plateau), corresponding to the two glass states (repulsive and attractive). The red dashed line represents the intersection of the two fits. The shaded red region represents the range of temperatures/attraction strengths at which the repulsive-to-attractive glass cross-over could reasonable occur.

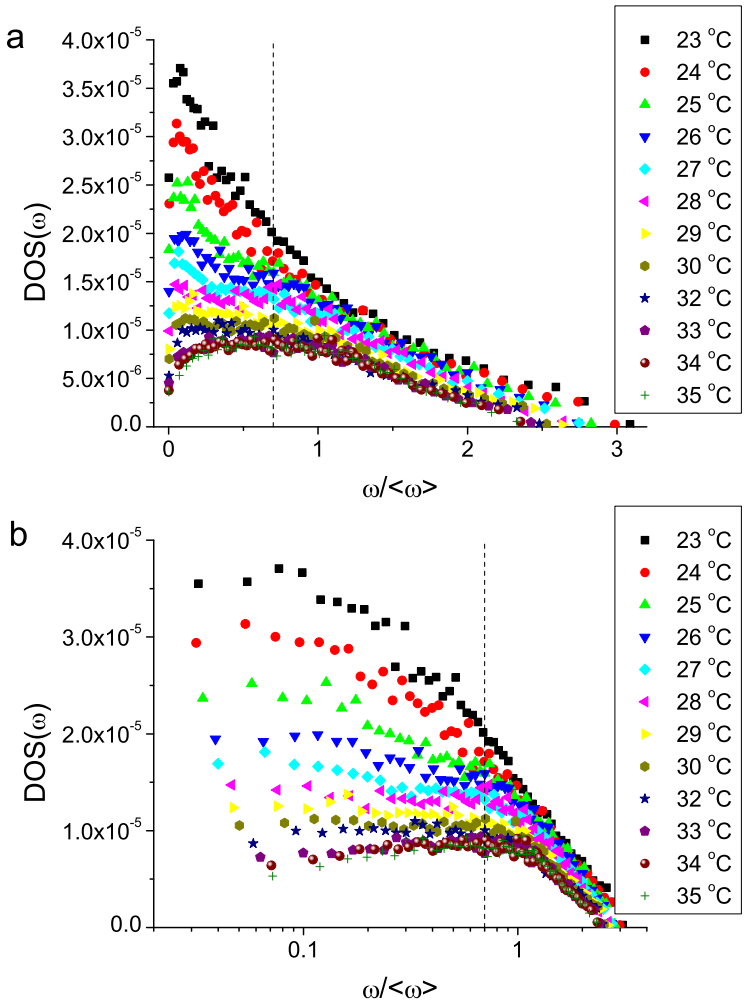

Figure 4.10: Vibrational Density of States, $DOS(\omega)$, versus scaled phonon frequency, $\omega/\langle\omega\rangle$, in a) linear and b) semi-log plots. Dashed line represents $\omega/\langle\omega\rangle = 0.7$.

4.4.3 Vibrational Phonon Behavior

The distribution of the $DOS(\omega)$ changes as the strength of interparticle attraction increases (Figure 4.10). Specifically, we observe the $DOS(\omega)$ of low frequency modes decreases as the strength of the attraction grows, *i.e.*, the number of low frequency modes decreases with increasing attraction strength. This is clearly observed when $DOS(\omega)$ is plotted as a function of the scaled phonon frequency, $\omega/\langle\omega\rangle$, on a log-scale (Fig. 4.10b). We qualitatively observe

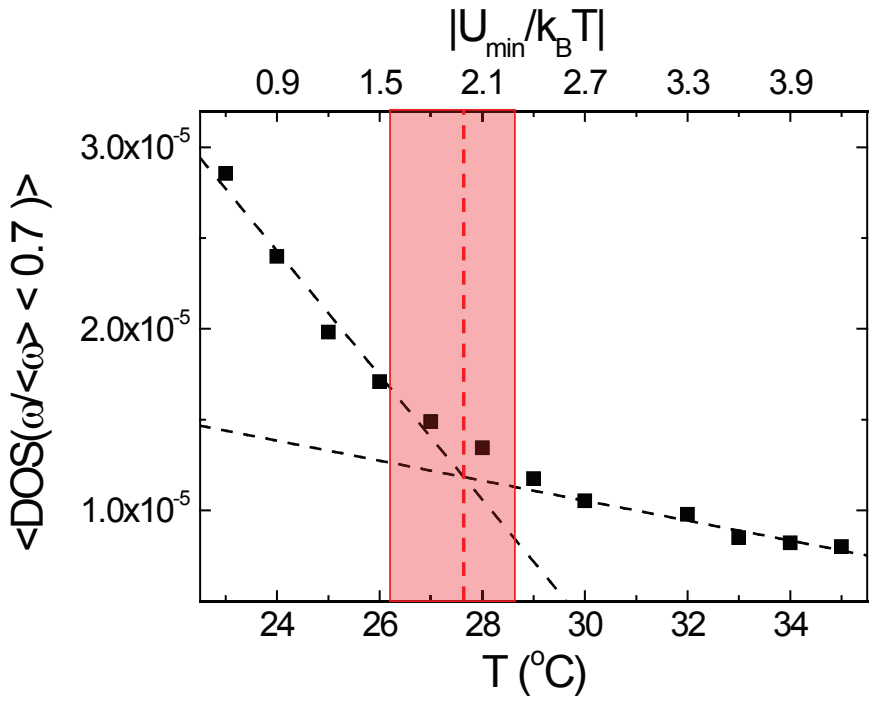

Figure 4.11: Average $DOS(\omega)$ for $\omega/\langle\omega\rangle < 0.7$, $\langle DOS(\omega/\langle\omega\rangle < 0.7)\rangle$, for all temperatures, T. Top x-axis is $|U_{min}/k_BT|$ measured in depletion experiments. Black dashed lines are linear fits to the two regimes (monotonic decrease and plateau), corresponding to the two glass states (repulsive and attractive). The red dashed line represents the intersection of the two fits. The shaded red region represents the range of temperatures/attraction strengths at which the repulsive-to-attractive glass cross-over could reasonable occur.

that the value of $DOS(\omega)$ at low frequencies decreases monotonically with increasing temperature/attraction strength. To quantifiy this effect, we calculated the average $DOS(\omega)$, $\langle DOS(\omega)\rangle$, for modes with $\omega/\langle\omega\rangle < 0.7$ (Figure 4.11). We observe a trend similar to that found in the MSD, where $\langle DOS(\omega/\langle\omega\rangle < 0.7)\rangle$ decreases monotonically and plateaus at strong attraction strengths. We observe that $\langle DOS(\omega/\langle\omega\rangle < 0.7)\rangle$ plateaus at attraction strengths larger than $2k_BT$. This provides further evidence of a transition occurring when the interparticle attraction strength is approximately $2k_BT$.

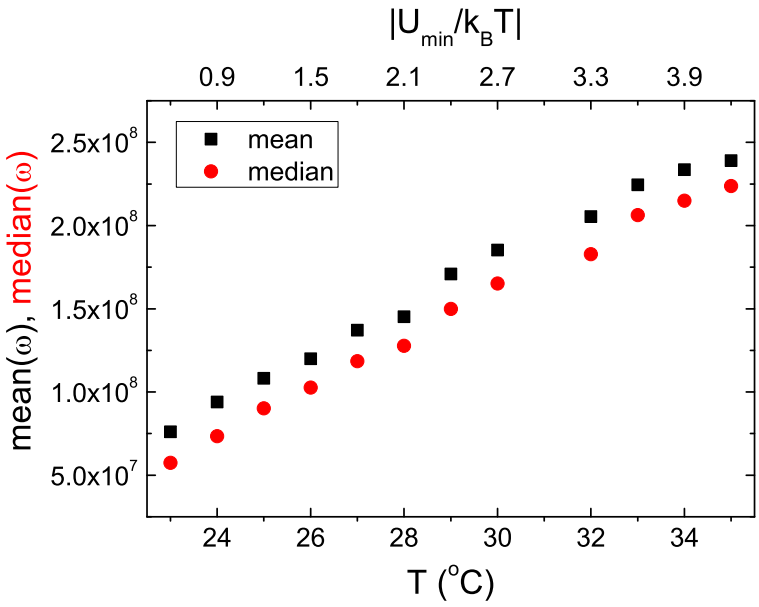

Figure 4.12: Mean (black squares) and median (red circles) frequencies for all temperatures, T. Top x-axis is $|U_{min}/k_BT|$ measured in depletion experiments.

It was observed that the mean and median phonon frequencies calculated increased monotonically with temperature (Figure 4.12). There was no evidence of a transition in the mean and median frequencies similar to the trends observed in the MSD and shape of the $DOS(\omega)$, as the mean and median frequencies appeared to follow a nearly linear trend with increasing temperature. This continuous increase in the mean and median frequencies is consistent with the fact that the interparticle attraction strength increases linearly with temperature. We expect that with increasing attraction strength, the effective spring constants, k, between all pairs of particles increase. Increasing spring constants leads to increasing frequencies since $\omega \propto \sqrt{k}$. The continuous increase of the mean frequencies is evidence that the strength of the interparticle bonds is continuously increasing. Therefore, the plateaus observed in other measured and calculated quantities are not caused by a saturation in the interparticle bond strength, but due to a saturation of the dynamical arrest in the system.

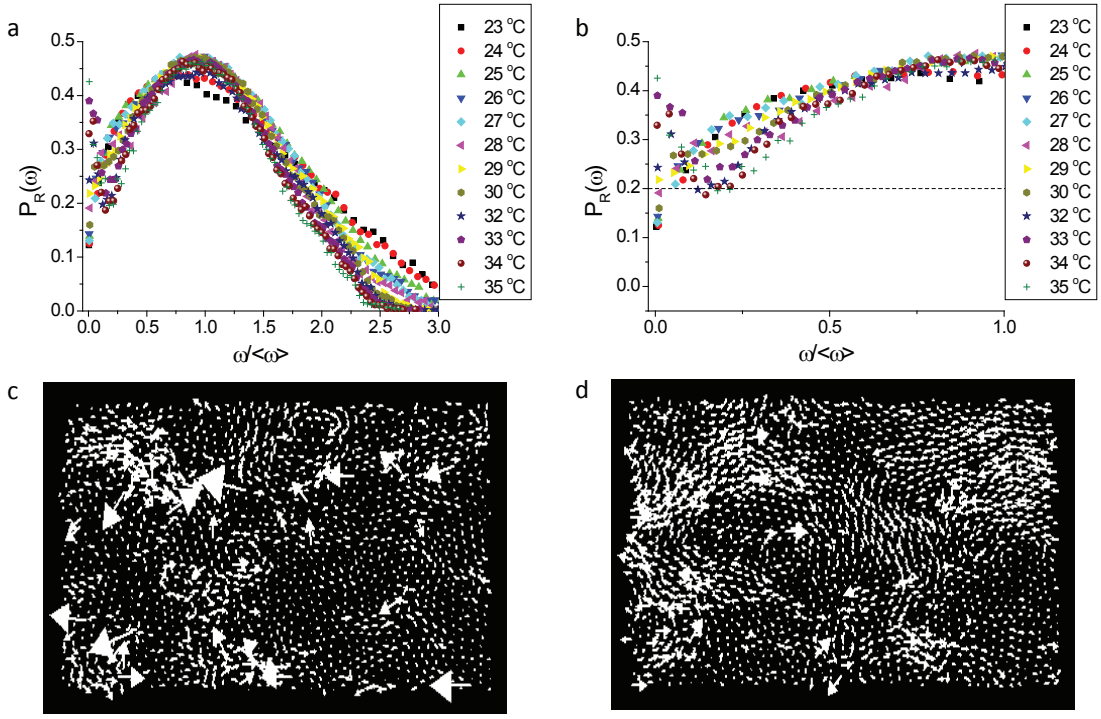

Figure 4.13: a) Participation ratio, $P_R(\omega)$, for all temperatures versus scaled frequency, $\omega/\langle\omega\rangle$. b) $P_R(\omega)$ of modes with $\omega/\langle\omega\rangle < 1$. Dashed line represents the cut-off value for extended ($P_R(\omega) > 0.2$) and localized ($P_R(\omega) < 0.2$) modes. c) and d) Vector displacement plots of representative low frequency modes in a repulsive glass ($T = 23\ ^o$C, $|U_{min}| = 0.5k_BT$) and an attractive glass ($T = 35\ ^o$C, $|U_{min}| = 4.2k_BT$), respectively.

We also measured the localization of the motion of these low frequency modes using the participation ratio. As previously described in **Chapter 2**, the participation ratio is defined as $P_R(\omega) = (\sum_\alpha e_{\alpha x}^2(\omega) + e_{\alpha y}^2(\omega))^2/(N_{tot}\sum_\alpha e_{\alpha x}^4(\omega) + e_{\alpha y}^4(\omega))$, where $e_{\alpha x}(\omega)$ and $e_{\alpha y}(\omega)$ are the x and y eigenvector components for particle α, respectively. Following convention, we refer to frequencies with a participation ratio below 0.2 as localized, and frequencies with participation ratio above 0.2 as extended [64]. At strong interparticle attractions, extended modes are observed that are not found in samples with weak interparticle attractions (Figure 4.13a-b).

Representative low frequency modes of a repulsive glass and an attractive glass are presented in Fig. 4.13a and b, respectively. These representative modes help visualize the effect that in

repulsive glasses the motion at low frequencies is quasi-localized, whereas in attractive glasses extended collective motion is found throughout the sample. The low frequency behavior of the repulsive glasses studied here are consistent with those previously studied [2,63–69], specifically the presence of quasi-localized modes is found. The extended motion observed here in the low frequency modes of attractive glasses is likely due to the strong interparticle bonds in attractive glasses. As one particle moves, it pulls its neighbors with it, who in turn pull their neighbors. This same reasoning can be used to account for the size and shape of cooperative rearrangement regions (CRRs) observed in attractive glasses is larger than those observed in repulsive glasses [146].

To quantify the presence of these extended low frequency modes in attractive glasses, we looked at the lowest 100 modes and found those modes that have a participation ratio larger than 0.2, *i.e.,* are extended. Looking at the number of the lowest 100 modes that are extended (Figure 4.14), we again see the same trend as observed in all of our other data: the number of extended modes of the lowest 100 modes that plateaus at attraction strengths above $2k_BT$. Thus, numerous quantities show the same trend: the vibrational and dynamical properties of colloidal glasses change monotonically as the interparticle attraction strength increases, and then saturates when the attraction strength is larger than $2k_BT$. This saturation signifies the transition from the repulsive glass state to the attractive glass state.

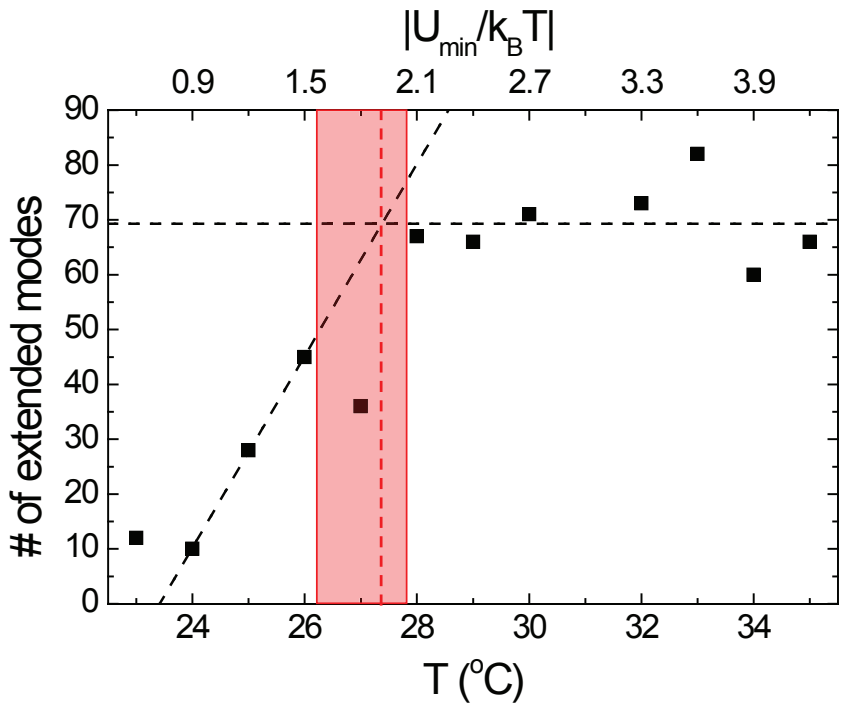

Figure 4.14: Number of extended modes ($P_R(\omega) > 0.2$) of the lowest 100 modes. Top x-axis is $|U_{min}/k_BT|$ measured in depletion experiments. Black dashed lines are linear fits to the two regimes (monotonic decrease and plateau), corresponding to the two glass states (repulsive and attractive). The red dashed line represents the intersection of the two fits. The shaded red region represents the range of temperatures/attraction strengths at which the repulsive-to-attractive glass cross-over could reasonable occur.

4.5 Conclusion

In summary, we experimentally studied the vibrational phonons of 2D colloidal glasses with increasing attraction strength, and present evidence that the transition from the repulsive glass state to the attractive glass state occurs above an interparticle attraction strength of $2k_BT$. This transition is signified by changes in the distribution of the $DOS(\omega)$, as well in a saturation of the particle dynamics. We observe that repulsive glasses have an excess of low frequency modes compared to attractive glasses. Furthermore, the motion of a majority of the lowest frequency modes in attractive glasses is spatially extended, wherein repulsive glasses the motion at low

frequencies is quasi-localized. We also observed that particle dynamics decreased monotonically with increasing attraction strength, but for attraction strengths larger than $2k_BT$ particle dynamics are saturated, signifying the system reaching a point of maximal arrest. The quantities measured herein did not display a discontinous jump at the transition point like those calculated from MCT, yet still displayed a noticeable change in behavior at the transition point.

There are two things to note in comparing the results presented here and the results from MCT. First, the state diagram predicted by MCT is for three-dimensional (3D) systems, while the work here is in 2D. Second, and perhaps more importantly, MCT uses a single interparticle attraction strength between all particles. However, in our experiments, three interparticle attraction strengths arise due to the bidispersed colloidal suspension used to frustrate crystallization. Remember that the depletion force is proportional to the size of the colloidal spheres, and so the three particle combinations (small-small, small-large, large-large) present in the sample are the cause of the three attraction strengths. Thus, our system is not a perfect experimental model for MCT.

4.6 Future Work

Looking forward, we intend to study how the dynamical heterogeneity in colloidal glasses changes with changing interparticle attraction strength. Previous studies have shown that the dynamics in attractive glasses are heterogeneous over a larger range of length and time scales compared to repulsive glasses [146]. These studies further showed that the cooperative rearrangement regions (CRRs) in attractive glasses are more compact and include more particles than the string-like CRRs in repulsive glasses. It would thus be interesting to see how the size

and shape of CRRs changes as a function of interparticle attraction strength.

To accomplish this study, samples will be made following the procedure set forth here, but video microscopy data will be recorded for at least 2 hours. Imaging over such a long time period ensures a number of rearrangements will be observed, and the upturn in the mean-squared displacement at long lag times can be measured. Quantification of the dynamical heterogeneity will be accomplished by measuring the four-point susceptibility, χ_4. Previous studies have used the peak value of χ_4 as an indicator of the crystal-to-glass transition in samples with increasing structural disorder [72]. It would thus be interesting to see if the peak in χ_4 can be a further indicator of the transition from the repulsive glass state to the attractive glass state along with the measurements presented in this chapter.

It would also be interesting to see if the re-entrance phenomenon observed in 3D experiments [30, 32–34] is also present in 2D samples (see Figure 4.1). Re-entrance in 3D occurs at lower colloidal packing fractions than the repulsive-to-attractive glass transition. This phenomenon is found when the attraction strength between particles increases, and the system transitions from the repulsive glass state to the fluid state. As interparticle attraction strength increases further, the system undergoes a second transition from the fluid state to the (solid) gel state. This is where the name "re-entrance" comes from; the system transitions from a solid state to a liquid state, and then back to a solid state. To date, re-entrance has not been observed in 2D. Exploring re-entrance in 2D would contribute to the larger picture of studying the role of dimensionality in the state diagram of glasses with attractive interparticle interactions, and would provide further insight into the glass transition.

Chapter 5

Conclusion/Future Directions

5.1 Summary

The vibrational properties of densely packed colloidal packings depend on the interparticle interactions and configurations of the constituent particles. In this thesis, we explored how the vibrational behavior of colloidal packings varied as the interparticle interactions evolved away from the traditional hard-sphere potential. Specifically, the interactions varied from hard-sphere repulsion to soft-sphere repulsion to depletion attraction. As part of this process, we developed a new means of tuning the attractive depletion interaction between colloids via control of depletant shape anisotropy; the scheme introduced a novel methodology for measuring properties of nano-scale macromolecules using video microscopy techniques.

In the first group of experiments, the phonons of colloidal crystals with bond strength disorder were studied. Vibrational modes in soft-particle crystals doped with hard particles were found to exhibit three distinct frequency regimes. At low frequencies, crystalline (Debye-like)

behavior in the density of states $DOS(\omega)$ was observed in all systems regardless of the number of hard-particle dopants, *i.e.* regardless of the degree of bond heterogeneity. These low frequency modes display long wavelength behavior in which hard and soft particles participate equally. At intermediate frequencies, the modes are extended and dominated by soft particles. At the highest frequencies, the modes are more localized and are dominated by hard particles. Computationally generated spring networks were created for comparison and exhibited many of the trends observed; they also offered means for extrapolation of the observed behavior to higher number-fractions of hard spheres. These experimental results imply that while the introduction of bond-strength disorder does indeed alter some of the vibrational properties of crystalline materials, compared to the introduction of structural disorder (at least for the levels of disorder probed by our experiments), the bond-strength does not as readily destroy the crystalline/Debye-like properties at low frequencies.

The second group of experiments measured the strength and range of the depletion attraction between colloidal particles *in situ* as a function of temperature. The depletants were surfactant micelles. We demonstrated that tuning the shape anisotropy of surfactant micelles permits modulation of the entropic attraction. This work introduces a simple and useful tool for controlling interactions in suspension. As part of this research, we also measured the rod length of $C_{12}E_6$ surfactant micelles as a function of temperature. The measured lengths are in good agreement with lengths reported by neutron scattering experiments. We show that the procedure reported is also an effective way to accurately measure the size and shape of the depletant molecules, even in the nanoscale range. Thus, the geometric properties of nanoscale macromolecules, *e.g.*, nanoparticles, surfactant micelles, chromonic liquid crystal stacks, *etc.*, could be ascertained by

measuring the depletion interaction between colloids suspended in a solution of the nanoscale macromolecules via the same approach.

The third group of experiments studied the phonons of 2D colloidal glasses as a function of interparticle potential, from hard-sphere like to depletion with increasing attraction strength. The work presents evidence for the existence of a cross-over transition from the repulsive glass state to the attractive glass state as the interparticle attraction strength increases above approximately $2k_BT$. This transition is signified by changes in the distribution of the $DOS(\omega)$, as well as in a saturation of various properties of the particle dynamics. We observed that repulsive glasses have an excess of low frequency modes compared to attractive glasses. Furthermore, the motion of a majority of the lowest frequency modes in attractive glasses tend to be spatially extended, whereas the motion in the low frequency modes of repulsive glasses tend to be quasi-localized. We also observed that for a given lag time the mean-squared displacement decreased monotonically with increasing attraction strength, but for attraction strengths larger than $2k_BT$ particle dynamics saturated, signifying the system had reached a point of maximal arrest. Therefore, we show that in 2D colloidal glasses the transition from the repulsive glass state to the attractive glass state exists and occurs at an interparticle attraction strength of about $2k_BT$.

5.2 Future Directions

In this section, ideas for future work with colloids whose interactions are different from the traditional hard-sphere interaction are described. Further, some of the groundwork for the proposed experiments has been worked out and is discussed below.

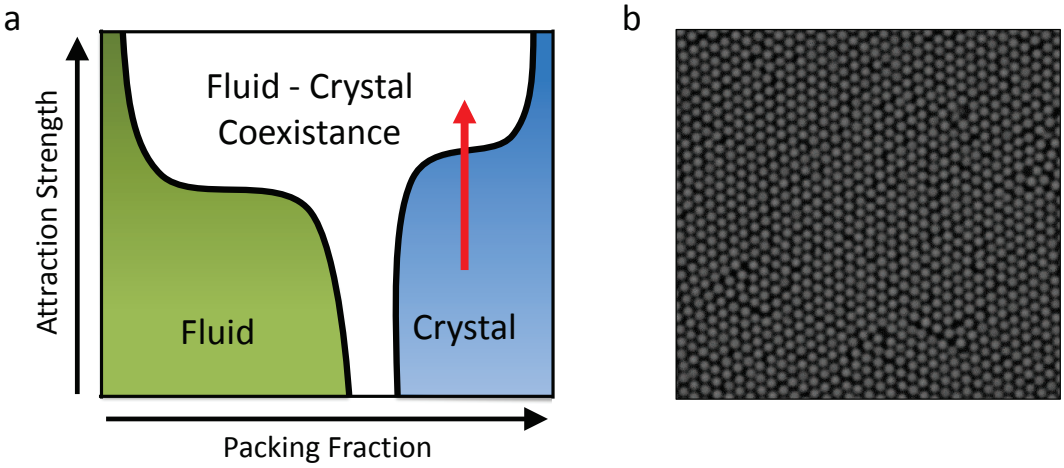

Figure 5.1: a) Qualitative representation of the state diagram of monodispersed colloidal packings with interparticle attraction. Red arrow represents the transition to be studied. b) Sample image of crystal at lowest temperature studied ($T = 24.5\ ^{o}$C) in preliminary experiments.

5.2.1 Attractive Interactions in Colloidal Crystals

Experiments with colloidal crystals that are modestly similar to the study of structurally *disordered* glasses with increasing interparticle attraction strength would be interesting to carry out. In particular, one could consider how the introduction of attractive interactions changes the behavior of structurally *ordered* crystals. Theoretical studies [196] and simulation work [20, 21] have shown that a phase transition is induced when the interparticle attraction strength between constituent particles in a crystal becomes sufficiently strong (Figure 5.1). Specifically, a single crystal evolves into a fluid-crystal coexistence regime, wherein the resulting crystal phase is denser than the initial crystal. Using the temperature tunable depletion interaction presented in this thesis, a detailed experimental study (the first) of this transition is possible.

We have taken the first steps towards this study. In preliminary work we observed structural changes in a colloidal crystal as the temperature, and thus interparticle attraction strength, increased. This preliminary sample was prepared following a similar procedure to that used to

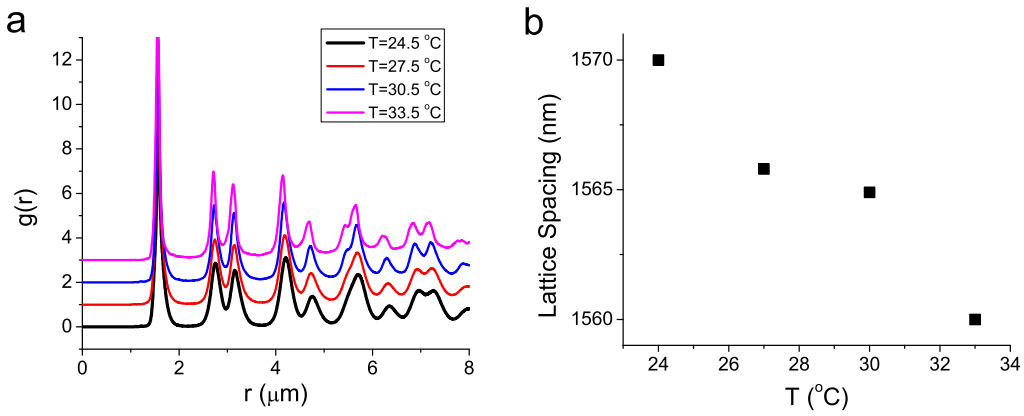

Figure 5.2: a) Measured pair correlation function, $g(r)$, for all temperatures studied. b) Lattice constant obtained from first peak in $g(r)$ as function of temperature.

make the glassy samples discussed in **Chapter 4**. The only difference in the procedure was that a monodisperse suspension of spheres (1.57 μm in diameter) was used to enable crystallization to occur (Fig 5.1). Therefore, a triangular lattice is formed. The overall structure of the system was not observed to change significantly, as evidenced by the measured $g(r)$ at each of the few temperatures studied, which were found to be very similar (Figure 5.2a). The first peak in $g(r)$ represents the lattice spacing of the crystal. Further, the overall structure of $g(r)$ was not observed to change; we found that the lattice constant shrank monotonically with increasing attraction strength (Fig. 5.2b).

We then observed that the number of defects increased with increasing attraction strength. In a perfect triangular lattice, all particles should have 6 nearest neighbors, NN. Therefore, we defined a defect as particle who has $NN \neq 6$. We see the number of defect particles increased as the temperature (attraction strength) increased (Figure 5.3a), while the number of particles with $NN = 6$ obviously decreased (Figure 5.3b). In order to have a single crystal transition into a coexistence regime between a dilute fluid and a dense crystal, interparticle bonds must be broken

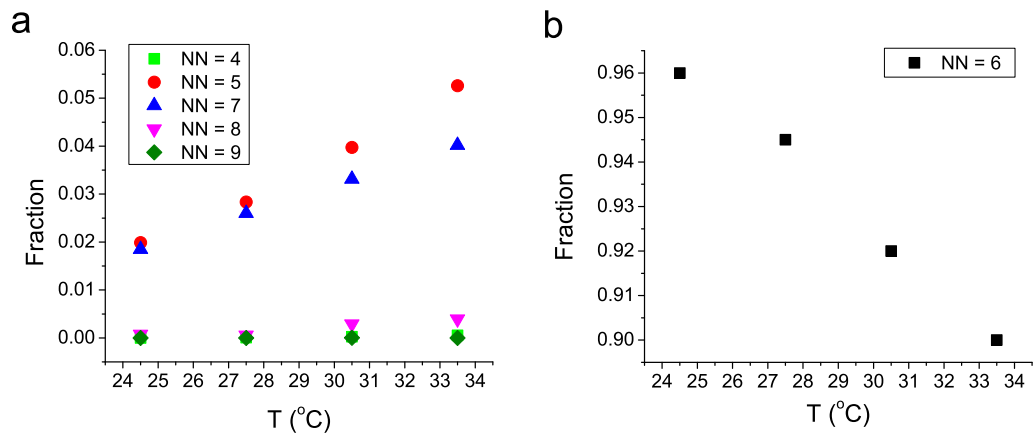

Figure 5.3: Fraction of a) defected particles, *i.e.*, particles with number of nearest neighbors $NN \neq 6$ and b) particles with $NN = 6$ as a function of temperature T.

to allow some regions of the crystal to melt into a fluid. Thus it makes sense that the number of defect particles increases.

While these preliminary results on the lattice constants and nearest neighbors show continuous changes with no clear signature of a transition, the susceptibility, χ_6, of the orientational order parameter, ψ_6, may provide an indicator for the crystal to fluid-crystal coexistence. We observed a sharp change in χ_6 as the interparticle attraction strength increased (Figure 5.4). However, more temperatures (attraction strengths) are necessary in order to fully characterize and understand these changes in χ_6.

To fully map out the phase transition from the crystal to the crystal-fluid coexistence phase, we also need to study several colloidal particle packing fractions. Further, to more accurately study this transition, we would ideally start with a perfect crystal lattice, *i.e.*, a crystal with no defects or grain boundaries. The crystal studied in the preliminary work had a number of defects and a grain boundary; this situation could affect the behavior of the system as the attraction strength is increased. Defects, especially grain boundaries, are the most likely to affect

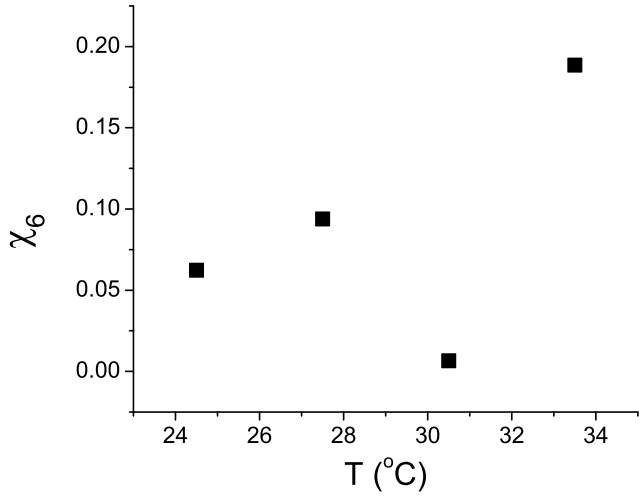

Figure 5.4: Susceptibility, χ_6, of the orientational order parameter as a function of temperature, T.

the quantities measured; their presence could make quantifying the transition difficult (but also interesting). The use of fractionation techniques should decrease the polydispersity in the particle size which, in turn, could reduce disorder in the crystals, since even a small amount of polydispersity is known to affect the structural order of a colloidal crystal. By decreasing the particle size polydispersity, we should be able to create larger crystal grains, and then by calculating χ_6 as a function of attraction strength for these larger crystal grains, we should be able to experimentally map out the phase diagram of crystals with attractive interparticle interactions.

5.2.2 Tuning Local Structure of Colloidal Gels

The use of the temperature tunable depletion interaction discussed in this thesis also provides a route to controlling the local structure in colloidal gel networks. Most (if not all) colloidal gel experiments to date have not had control over the local structure of the gel networks studied. The investigators were content to simply study the dynamical [30, 32–34], rheological [31], and vibrational properties [4] of gels whose constituent particles are structurally disordered.

However, it would be interesting to see how the properties of gel networks change as the local structure becomes more or less ordered.

We have conducted some qualitative experiments to explore our ability to control the local structure in a 2D colloidal gel network via tunable depletion interactions. These preliminary observations were accomplished utilizing the fact that the depletion force between colloidal spheres is proportional to the size of spheres along with temperature tunable depletion interactions. Specifically, in a binary suspension of colloids with temperature tunable depletion interactions, the sample temperature can first be set to a temperature at which the large particles aggregate, denoted as T_1. We then hold the sample temperature at T_1 for some time, τ, to allow the large particles to self-assemble into colloidal crystallites. Then the sample temperature is raised to the temperature at which the small particles aggregate, denoted as T_2, and a gel network is formed. This procedure is much easier (but also somewhat similar) to what would be needed to create colloidal bigels, as briefly discussed in **Chapter 3**.

The time τ at which the sample remains at T_1 is the knob that can be used to control the local structure of the gel. For longer τ, larger crystal domains of large particles form. Preliminary observations were done using a binary suspension of 1.57 μm (large) and 1 μm (small) silica spheres in a suspension of $C_{12}E_6$ surfactant micelles and salt (NaCl). The number-ratio of big to small particles was set to approximately 1:1 in these samples. The concentrations of $C_{12}E_6$ and NaCl are the same as those used in the various experiments explained in this thesis. With these two sizes of colloidal particles and the concentrations of $C_{12}E_6$ and NaCl used, $T_1 = 29\ ^oC$ and $T_2 = 35\ ^oC$. Since the temperature tunability of the depletion interaction is reversible, large quantities of data can be acquired from a single sample by decreasing the sample temperature to

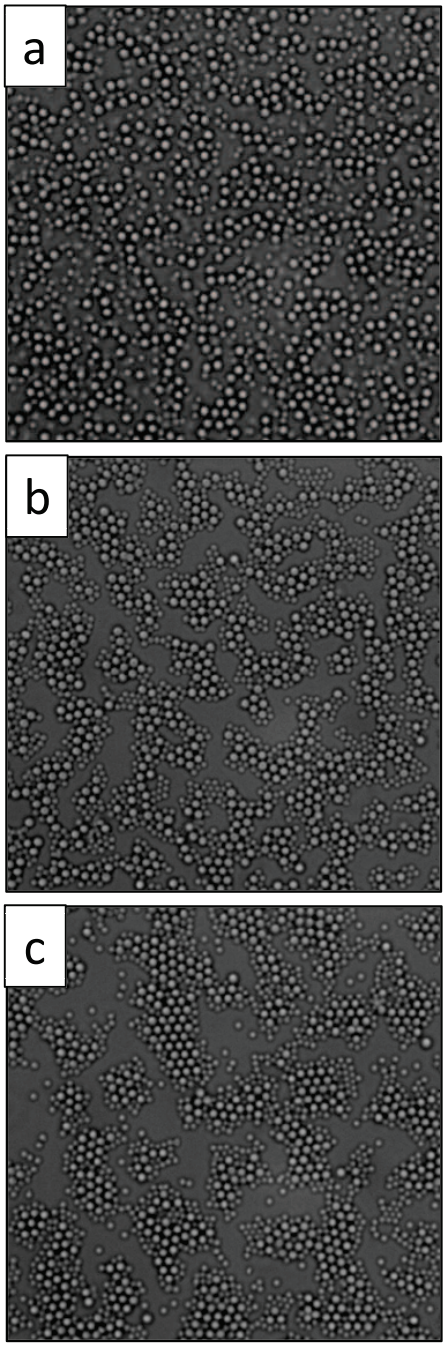

Figure 5.5: a) Colloidal fluid at temperature $T < T_1 = 29\ ^oC$. b) and c) Gel networks formed with $\tau = 0$ and 60 minutes, respectively.

below T_1 and waiting for the system to fully melt back into the fluid state (Figure 5.5a).

Qualitatively, the structure was observed to be significantly different for various values of τs. For $\tau = 0$, we observe the traditional structurally disordered glass network (Fig. 5.5b). The gel networks formed with $\tau = 60$ minutes appear as crystal domains of large particles connected by "bridges" of small particles (Fig. 5.5c).

Looking to the future, it would be interesting to characterize the structures formed as a function of τ, and then study the dynamical and vibrational properties of the various structures. Perhaps an even more interesting and application-based study would be to measure the rheological properties of gels as a function of their local structure. The use of an interfacial rheometer [197, 198] would provide a means to study concurrent changes in structure at the single-particle level while the system is driven by an oscillatory stress.

5.2.3 Vibrational Behavior and Particle Dynamics in Buckled Colloidal Monolayers

Previous colloid experiments have observed that quasi-two-dimensional densely packed colloidal spheres form in-plane triangular lattices with out-of-plane up and down buckling. These samples are sandwiched between parallel walls with a separation approximately 1.5 times the particle diameter [199, 200]. The buckled monolayer configurations are classical colloids analogous to the famous antiferromagnetic Ising model. Particles that buckle upwards (downwards) are associated with the "up" ("down") spin state (Figure 5.6a). The nearest-neighbor excluded volume interactions between particles favor opposite states. More simply, up particles want to be next to down particles, and vice versa. In 1D, these bond requirements are easily fulfilled. In a 2D triangular lattice however, for any given triangle two bonds are satisfied, but the third

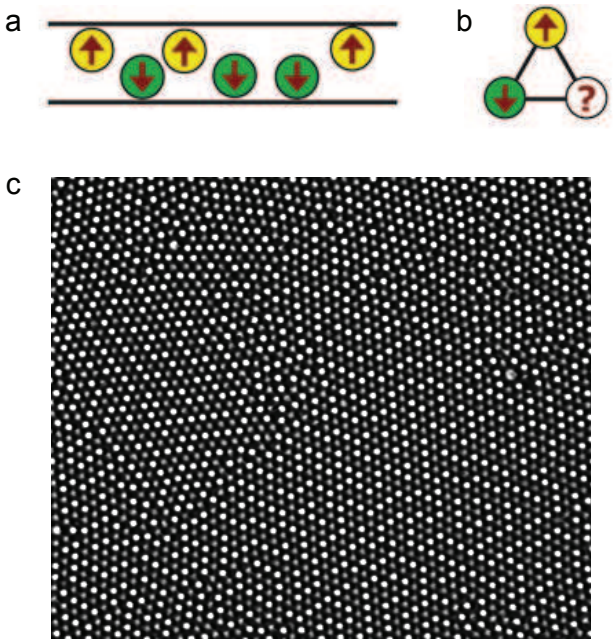

Figure 5.6: a) Side view of buckled monolayer. Particles buckled upwards (downwards) are those in the up (down) state. b) Three spins on a triangular plaquette cannot simultaneously satisfy all antiferromagnetic interactions. c) Experimental image of buckled colloidal monolayer. White (grey) particles are considered to be in the "up" ("down") state.

cannot be satisfied. Thus the system is considered "frustrated" (Fig. 5.6b). In fact, this is the classic example of a frustrated system.

Our previous experiments, and accompanying theory, showed that single-particle dynamics governed by in-plane lattice distortions partially relieve frustration and produce ground states with zigzagging stripes (Fig. 5.6c). The out-of-plane particle motions in these studies were treated as binary, *i.e.*, up or down. To shed further light on such systems it would be interesting to measure the in-plane and out-of-plane Brownian motion (Brownian vibrations) of the particles.

We performed preliminary experiments along these lines, decomposing the in-plane and out-of-plane particle motions. The key to carrying out this task is to realize that the out-of-plane motion can be derived from the intensity of the particles as measured by video microscopy.

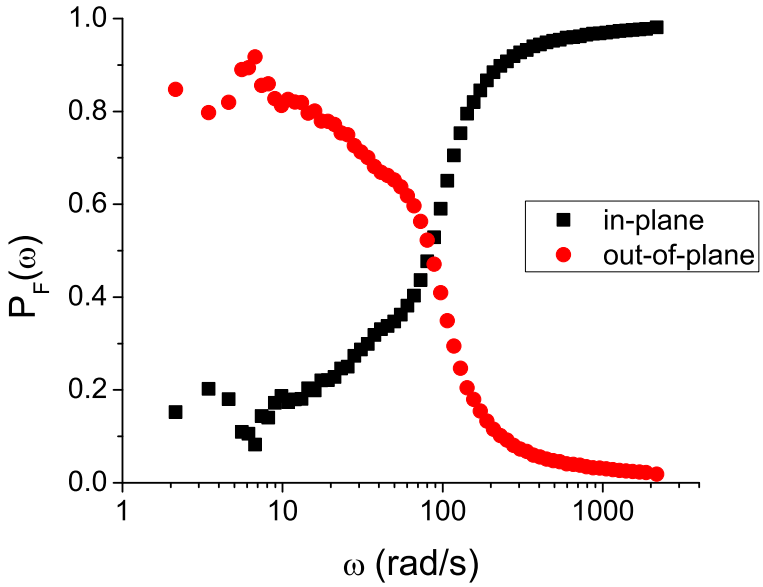

Figure 5.7: Participation fraction, $P_F(\omega)$, for the in-plane (black squares) and out-of-plane (red circles) particle vibrations.

Specifically, we measured the vibrational phonons of the zigzagging stripe ground state. We observed that the motion at low frequencies was dominated by the out-of-plane motion, while the motion at high frequencies was dominated by the in-plane motion (Figure 5.7). Presently, the conversion of particle intensity to out-of-plane motion was somewhat coarse and could be improved. To further the study of the in- and out-of-plane vibrations, a more accurate mapping of the particle intensities to particle motions is necessary. The use of holographic video microscopy [201] might be a useful tool for this endeavor.

In the future, it would be interesting to further explore the differences between the in-plane and out-of-plane motion in such a frustrated system. In-plane, the average particle positions are stable as the 2D structure of the system is always a triangular lattice. However, particles can "flip" from the up state to the down state and vice versa. One could consider this changing of state as somewhat analogous to rearrangements observed in glasses. When decomposing the

particle motions into their in-plane and out-of-plane contributions, it might be observed that the in-plane motion follows behavior found in ordered crystals, while the out-of-plane motion follows behavior more commonly found in disordered packings. Perhaps this frustrated system might lead to a new form of material due to its display of both crystalline and glassy behavior.

5.2.4 Measuring Length Distributions of Lyotropic Chromonic Liquid Crystal Stacks

Liquid crystals (LCs) are partially oredered matter that are found in our every-day lives, in devices such as computer screens, phone screens and television screens. The most prevalent LC phase of interest is the nematic phase wherein the rod-like mesogens tend to align along a particular direction (they are orientationally ordered) but the mesogens are translationally disordered. An especially interesting set of liquid crystals are lyotropic chromonic liquid crystals (LCLCs). LCLCs are composed of stacks of plate-like molecules. The stacks are very long compared to the cross-sectional width (one molecule), and so the aspect ratio of the stack is large, *i.e.,* the stacks have a large anisotropy and can be modeled as thin rods. The phases observed in LCLCs are found to depend on the length of the stacks, which can be tuned via concentration or temperature. Ultimately, it is desirable to know the distribution of stack sizes in order to better understand these LCLC systems, and also to further advance the various technologies that make use of these particular liquid crystals which reside in water-based media and thus hold potential to bring LC technology to biomaterials.

Previous (unpublished) research in our lab has shown that the LCLC Disodium cromoglycate (DSCG) can be used as a depletant to induce an attractive force between colloidal spheres

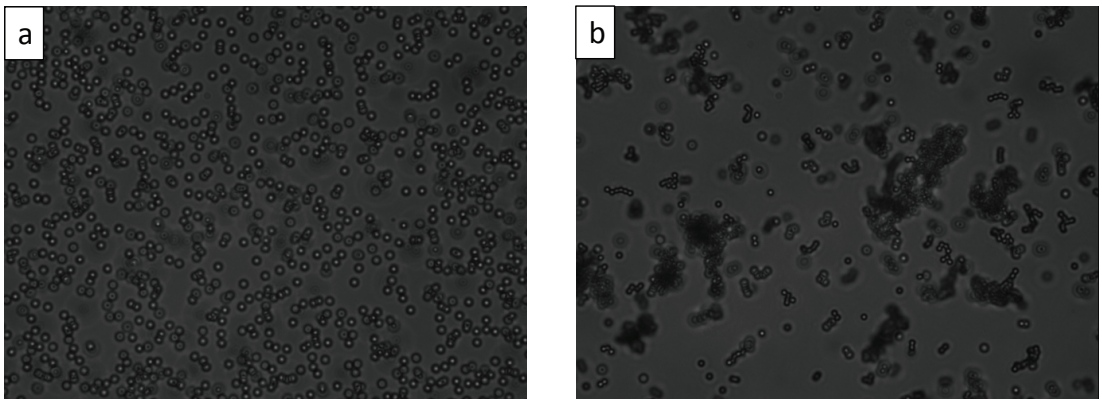

Figure 5.8: Sample images of 1 μm polystyrene spheres in a suspension of 0.1% NaCl a) 0.01% and b) 7% DSCG. Observe that at low concentrations of DSCG (a) no aggregation is found, while at high concentrations (b) aggregation is observed due to depletion interactions.

suspended in a solution of DSCG (Figure 5.8). In this work, we observed that at very low concentrations of DSCG no attraction arose between the colloidal particles (Fig. 5.8), but when the concentration of DSCG was increased, then the colloidal spheres began to aggregate (Fig. 5.8). In **Chapter 3** of this thesis, we described a method to measure the sizes of anisotropic nanoscale macromolecules; this approach measured the depletion interaction between micron-size colloidal particles. While our early work on LCLC aggregation was qualitative, in the context of this new experimental probe we should be able to measure the average size (and size distribution) of the DSCG LCLCs *in situ*. In particular, by fine tuning of various experimental parameters, *e.g.*, concentrations of DSCG and salt (NaCl) and sample temperature, the experimental procedure described in **Chapter 3** could be employed to quantitatively characterize the size and distribution of sizes of DSCG stacks as a function of both concentration and temperature. This information would be new, and ultimately, understanding the size distributions of the DSCG stacks would help us further understand and predict the phase behavior of such LCLCs.

Bibliography

[1] Wei-Shao Wei, Mohamed Amine Gharbi, Matthew A. Lohr, Tim Still, Matthew D. Gratale, T. C. Lubensky, Kathleen J. Stebe, and A. G. Yodh. Dynamics of ordered colloidal particle monolayers at nematic liquid crystal interfaces. Submitted for publication, 2016.

[2] Ke Chen, Wouter G. Ellenbroek, Zexin Zhang, Daniel T. N. Chen, Peter J. Yunker, Silke Henkes, Carolina Brito, Olivier Dauchot, Wim van Saarloos, Andrea J. Liu, and A. G. Yodh. Low-Frequency Vibrations of Soft Colloidal Glasses. *Physical Review Letters*, 105(2):025501+, July 2010.

[3] Jacek Gapinski, Jedrzej Szymanski, Agnieszka Wilk, Joachim Kohlbrecher, Adam Patkowski, and Robert Holyst. Size and shape of micelles studied by means of sans, pcs, and fcs. *Langmuir*, 26(12):9304–9314, June 2010.

[4] Matthew A. Lohr, Tim Still, Raman Ganti, Matthew D. Gratale, Zoey S. Davidson, Kevin B. Aptowicz, Carl P. Goodrich, Daniel M. Sussman, and A. G. Yodh. Vibrational and structural signatures of the crossover between dense glassy and sparse gel-like attractive colloidal packings. *Phys. Rev. E*, 90:062305, Dec 2014.

[5] K. Dawson, G. Foffi, M. Fuchs, W. Götze, F. Sciortino, M. Sperl, P. Tartaglia, Th. Voigtmann, and E. Zaccarelli. Higher-order glass-transition singularities in colloidal systems with attractive interactions. *Phys. Rev. E*, 63:011401, Dec 2000.

[6] Jean Perrin. *Atoms*. D. Van Nostrand Company, 1916.

[7] P.N. Pusey, W. Van Megen, S.M. Underwood, P. Bartlett, and R.H. Ottewill. Colloidal fluids, crystals and glasses. *Physica A: Statistical Mechanics and its Applications*, 176(1):16 – 27, 1991.

[8] Hartmut Löwen. Melting, freezing and colloidal suspensions. *Physics Reports*, 237(5):249 – 324, 1994.

[9] Tullio Scopigno, Giancarlo Ruocco, Francesco Sette, and Giulio Monaco. Is the fragility of a liquid embedded in the properties of its glass? *Science*, 302(5646):849–852, 2003.

[10] M. D. Ediger and Peter Harrowell. Perspective: Supercooled liquids and glasses. *The Journal of Chemical Physics*, 137(8), 2012.

[11] Gary L. Hunter and Eric R. Weeks. The physics of the colloidal glass transition. *Reports on Progress in Physics*, 75(6):066501+, June 2012.

[12] Julie A. Champion, Yogesh K. Katare, and Samir Mitragotri. Making polymeric micro- and nanoparticles of complex shapes. *Proceedings of the National Academy of Sciences*, 104(29):11901–11904, 2007.

[13] C. C. Ho, A. Keller, J. A. Odell, and R. H. Ottewill. Preparation of monodisperse ellipsoidal polystyrene particles. *Colloid and Polymer Science*, 271(5):469–479, 1993.

[14] Peter J. Yunker, Tim Still, Matthew A. Lohr, and A. G. Yodh. Suppression of the coffee-ring effect by shape-dependent capillary interactions. *Nature*, 476(7360):308–311, August 2011.

[15] Peter J. Yunker, Ke Chen, Zexin Zhang, Wouter G. Ellenbroek, Andrea J. Liu, and A. G. Yodh. Rotational and translational phonon modes in glasses composed of ellipsoidal particles. *Physical Review E*, 83(1):011403+, January 2011.

[16] Zhongyu Zheng, Feng Wang, and Yilong Han. Glass transitions in quasi-two-dimensional suspensions of colloidal ellipsoids. *Phys. Rev. Lett.*, 107:065702, Aug 2011.

[17] Chandan K. Mishra, Amritha Rangarajan, and Rajesh Ganapathy. Two-step glass transition induced by attractive interactions in quasi-two-dimensional suspensions of ellipsoidal particles. *Phys. Rev. Lett.*, 110:188301, Apr 2013.

[18] A. G. Yodh, K. Lin, J. C. Crocker, A. D. Dinsmore, R. Verma, and P. D. Kaplan. Entropically driven self–assembly and interaction in suspension. *Philosophical Transactions of the Royal Society of London A: Mathematical, Physical and Engineering Sciences*, 359(1782):921–937, 2001.

[19] Emanuela Zaccarelli and Wilson C. K. Poon. Colloidal glasses and gels: The interplay of bonding and caging. *Proceedings of the National Academy of Sciences*, 106(36):15203–15208, 2009.

[20] Peter Bolhuis, Maarten Hagen, and Daan Frenkel. Isostructural solid-solid transition in crystalline systems with short-ranged interaction. *Phys. Rev. E*, 50:4880–4890, Dec 1994.

[21] Z T Nemeth and C N Likos. Solid to solid isostructural transitions: The case of attractive yukawa potentials. *Journal of Physics: Condensed Matter*, 7(41):L537, 1995.

[22] P. C. Hemmer, E. Velasco, L. Mederos, G. Navascus, and G. Stell. Solid-solid transitions induced by repulsive interactions. *The Journal of Chemical Physics*, 114(5):2268–2275, 2001.

[23] H. Senff and W. Richtering. Influence of cross-link density on rheological properties of temperature-sensitive microgel suspensions. *Colloid & Polymer Science*, 278(9):830–840, September 2000.

[24] Johan Mattsson, Hans M. Wyss, Alberto Fernandez-Nieves, Kunimasa Miyazaki, Zhibing Hu, David R. Reichman, and David A. Weitz. Soft colloids make strong glasses. *Nature*, 462(7269):83–86, November 2009.

[25] D. J. W. Aastuen, N. A. Clark, L. K. Cotter, and Bruce J. Ackerson. Nucleation and growth of colloidal crystals. *Phys. Rev. Lett.*, 57:1733–1736, Oct 1986.

[26] P. N. Pusey and W. van Megen. Phase behaviour of concentrated suspensions of nearly hard colloidal spheres. *Nature*, 320(6060):340–342, March 1986.

[27] A. D. Dinsmore, A. G. Yodh, and D. J. Pine. Phase diagrams of nearly-hard-sphere binary colloids. *Physical Review E*, 52(4):4045–4057, October 1995.

[28] C. Patrick Royall, Wilson C. K. Poon, and Eric R. Weeks. In search of colloidal hard spheres. *Soft Matter*, 9:17–27, 2013.

[29] W C K Poon. The physics of a model colloidpolymer mixture. *Journal of Physics: Condensed Matter*, 14(33):R859, 2002.

[30] K. N. Pham, S. U. Egelhaaf, P. N. Pusey, and W. C. K. Poon. Glasses in hard spheres with short-range attraction. *Phys. Rev. E*, 69:011503, Jan 2004.

[31] N. Koumakis and G. Petekidis. Two step yielding in attractive colloids: transition from gels to attractive glasses. *Soft Matter*, 7:2456–2470, 2011.

[32] Laura J. Kaufman and David A. Weitz. Direct imaging of repulsive and attractive colloidal glasses. *The Journal of Chemical Physics*, 125(7):–, 2006.

[33] A. Latka, Y. Han, A. M. Alsayed, A. B. Schofield, A. G. Yodh, and P. Habdas. Particle dynamics in colloidal suspensions above and below the glass-liquid re-entrance transition. *EPL (Europhysics Letters)*, 86(5):58001, 2009.

[34] Nikoleta B. Simeonova, Roel P. A. Dullens, Dirk G. A. L. Aarts, Volkert W. A. de Villeneuve, Henk N. W. Lekkerkerker, and Willem K. Kegel. Devitrification of colloidal glasses in real space. *Phys. Rev. E*, 73:041401, Apr 2006.

[35] Stefano Sacanna, David J. Pine, and Gi-Ra Yi. Engineering shape: the novel geometries of colloidal self-assembly. *Soft Matter*, 9:8096–8106, 2013.

[36] S. Sacanna, W. T. M. Irvine, P. M. Chaikin, and D. J. Pine. Lock and key colloids. *Nature*, 464(7288):575–578, March 2010.

[37] Guangnan Meng, Natalie Arkus, Michael P. Brenner, and Vinothan N. Manoharan. The free-energy landscape of clusters of attractive hard spheres. *Science*, 327(5965):560–563, 2010.

[38] Yu Wang, Yufeng Wang, Xiaolong Zheng, Gi-Ra Yi, Stefano Sacanna, David J. Pine, and Marcus Weck. Three-dimensional lock and key colloids. *J. Am. Chem. Soc.*, 136(19):6866–6869, May 2014.

[39] Daniela J. Kraft, Ran Ni, Frank Smallenburg, Michiel Hermes, Kisun Yoon, David A. Weitz, Alfons van Blaaderen, Jan Groenewold, Marjolein Dijkstra, and Willem K. Kegel. Surface roughness directed self-assembly of patchy particles into colloidal micelles. *Proceedings of the National Academy of Sciences*, 109(27):10787–10792, 2012.

[40] Stéphane Badaire, Cécile Cottin-Bizonne, Joseph W. Woody, Allen Yang, and Abraham D. Stroock. Shape selectivity in the assembly of lithographically designed colloidal particles. *J. Am. Chem. Soc.*, 129(1):40–41, January 2007.

[41] Stéphane Badaire, Cécile Cottin-Bizonne, and Abraham D. Stroock. Experimental investigation of selective colloidal interactions controlled by shape, surface roughness, and steric layers. *Langmuir*, 24(20):11451–11463, October 2008.

[42] Kun Zhao and Thomas G. Mason. Suppressing and enhancing depletion attractions between surfaces roughened by asperities. *Phys. Rev. Lett.*, 101:148301, Sep 2008.

[43] Kun Zhao and Thomas G. Mason. Directing colloidal self-assembly through roughness-controlled depletion attractions. *Phys. Rev. Lett.*, 99:268301, Dec 2007.

[44] Edward Barry and Zvonimir Dogic. Entropy driven self-assembly of nonamphiphilic colloidal membranes. *Proceedings of the National Academy of Sciences*, 107(23):10348–10353, 2010.

[45] Thomas Gibaud, Edward Barry, Mark J. Zakhary, Mir Henglin, Andrew Ward, Yasheng Yang, Cristina Berciu, Rudolf Oldenbourg, Michael F. Hagan, Daniela Nicastro, Robert B. Meyer, and Zvonimir Dogic. Reconfigurable self-assembly through chiral control of interfacial tension. *Nature*, 481(7381):348–351, January 2012.

[46] Tara D. Edwards, Yuguang Yang, W. Neil Everett, and Michael A. Bevan. Reconfigurable multi-scale colloidal assembly on excluded volume patterns. *Scientific Reports*, 5:13612–, September 2015.

[47] B. Sierra-Martin and A. Fernandez-Nieves. Phase and non-equilibrium behaviour of microgel suspensions as a function of particle stiffness. *Soft Matter*, 8(15):4141–4150, 2012.

[48] Matthew D. Gratale, Peter J. Yunker, Ke Chen, Tim Still, Kevin B. Aptowicz, and A. G. Yodh. Phonons in two-dimensional colloidal crystals with bond-strength disorder. *Phys. Rev. E*, 87:052301, May 2013.

[49] Peter J. Yunker, Matthew Gratale, Matthew A. Lohr, Tim Still, T. C. Lubensky, and A. G. Yodh. Influence of particle shape on bending rigidity of colloidal monolayer membranes and particle deposition during droplet evaporation in confined geometries. *Phys. Rev. Lett.*, 108:228303, Jun 2012.

[50] Peter J. Yunker, Zexin Zhang, Matthew Gratale, Ke Chen, and A. G. Yodh. Relationship between neighbor number and vibrational spectra in disordered colloidal clusters with attractive interactions. *The Journal of Chemical Physics*, 138(12), 2013.

[51] P. N. Pusey. Colloidal glasses. *Journal of Physics: Condensed Matter*, 20(49):494202+, November 2008.

[52] Zbigniew H. Stachurski. On Structure and Properties of Amorphous Materials. *Materials*, 4(9):1564–1598, September 2011.

[53] Susanne Schneider. Bulk metallic glasses. *Journal of Physics: Condensed Matter*, 13(34):7723+, August 2001.

[54] M. D. Ediger, C. A. Angell, and Sidney R. Nagel. Supercooled Liquids and Glasses. *J. Phys. Chem.*, 100(31):13200–13212, January 1996.

[55] G. N. Greaves and S. Sen. Inorganic glasses, glass-forming liquids and amorphizing solids. *Advances in Physics*, 56(1):1–166, January 2007.

[56] B. Frick and D. Richter. The microscopic basis of the glass transition in polymers from neutron scattering studies. *Science (New York, N.Y.)*, 267(5206):1939–1945, March 1995.

[57] K. Chen, E. J. Saltzman, and K. S. Schweizer. Segmental dynamics in polymers: from cold melts to ageing and stressed glasses. *Journal of Physics: Condensed Matter*, 21(50):503101+, November 2009.

[58] M. van Hecke. Jamming of soft particles: geometry, mechanics, scaling and isostaticity. *Journal of Physics: Condensed Matter*, 22(3):033101+, January 2010.

[59] C. Brito and M. Wyart. On the rigidity of a hard-sphere glass near random close packing. *EPL (Europhysics Letters)*, 76(1):149–155, January 2007.

[60] Matthieu Wyart. On the Rigidity of Amorphous Solids. *Annales de Physique*, 30(3):1–96, December 2005.

[61] Ning Xu. Mechanical, vibrational, and dynamical properties of amorphous systems near jamming. *Frontiers of Physics in China*, 6(1):109–123, September 2011.

[62] W. A. Phillips, editor. *Amorphous Solids: Low-Temperature Properties*. Springer, 1 edition, April 1981.

[63] N. Xu, V. Vitelli, A. J. Liu, and S. R. Nagel. Anharmonic and quasi-localized vibrations in jammed solids?Modes for mechanical failure. *EPL (Europhysics Letters)*, pages 56001+, June 2010.

[64] Ke Chen, M. L. Manning, Peter J. Yunker, Wouter G. Ellenbroek, Zexin Zhang, Andrea J. Liu, and A. G. Yodh. Measurement of Correlations between Low-Frequency Vibrational Modes and Particle Rearrangements in Quasi-Two-Dimensional Colloidal Glasses. *Physical Review Letters*, 107:108301+, August 2011.

[65] Asaph W. Cooper, Heidi Perry, Peter Harrowell, and David R. Reichman. Localized soft modes and the supercooled liquid's irreversible passage through its configuration space. *The Journal of Chemical Physics*, 131(19):194508+, 2009.

[66] Asaph Widmer-Cooper, Heidi Perry, Peter Harrowell, and David R. Reichman. Irreversible reorganization in a supercooled liquid originates from localized soft modes. *Nat Phys*, 4(9):711–715, September 2008.

[67] A. Tanguy, B. Mantisi, and M. Tsamados. Vibrational modes as a predictor for plasticity in a model glass. *EPL (Europhysics Letters)*, pages 16004+, April 2010.

[68] Carolina Brito and Matthieu Wyart. Heterogeneous dynamics, marginal stability and soft modes in hard sphere glasses. *Journal of Statistical Mechanics: Theory and Experiment*, 2007(08):L08003+, August 2007.

[69] Kai Sun, Anton Souslov, Xiaoming Mao, and T. C. Lubensky. Surface phonons, elastic response, and conformal invariance in twisted kagome lattices. *Proceedings of the National Academy of Sciences*, 109(31):12369–12374, July 2012.

[70] H. S. Chen, H. J. Leamy, and C. E. Miller. Preparation of Glassy Metals. *Annual Review of Materials Science*, 10(1):363–391, 1980.

[71] C. A. Angell. Formation of Glasses from Liquids and Biopolymers. *Science*, 267(5206):1924–1935, March 1995.

[72] Peter Yunker, Zexin Zhang, and A. G. Yodh. Observation of the Disorder-Induced Crystal-to-Glass Transition. *Physical Review Letters*, 104(1):015701+, January 2010.

[73] Antina Ghosh, Vijayakumar K. Chikkadi, Peter Schall, Jorge Kurchan, and Daniel Bonn. Density of States of Colloidal Glasses. *Physical Review Letters*, 104(24):248305+, June 2010.

[74] H. M. Lindsay and P. M. Chaikin. Elastic properties of colloidal crystals and glasses. *The Journal of Chemical Physics*, 76(7):3774–3781, 1982.

[75] Nikoleta B. Simeonova and Willem K. Kegel. Gravity-Induced Aging in Glasses of Colloidal Hard Spheres. *Physical Review Letters*, 93(3):035701+, July 2004.

[76] P. N. Pusey and W. van Megen. Observation of a glass transition in suspensions of spherical colloidal particles. *Physical Review Letters*, 59(18):2083–2086, November 1987.

[77] Hans J. Schöpe, Gary Bryant, and William van Megen. Effect of polydispersity on the crystallization kinetics of suspensions of colloidal hard spheres when approaching the glass transition. *The Journal of Chemical Physics*, 127(8):084505+, 2007.

[78] Eric R. Weeks, J. C. Crocker, Andrew C. Levitt, Andrew Schofield, and D. A. Weitz. Three-Dimensional Direct Imaging of Structural Relaxation Near the Colloidal Glass Transition. *Science*, 287(5453):627–631, January 2000.

[79] See E. Phan, William B. Russel, Jixiang Zhu, and Paul M. Chaikin. Effects of polydispersity on hard sphere crystals. *The Journal of Chemical Physics*, 108(23):9789–9795, 1998.

[80] C. Patrick Royall, Stephen R. Williams, Takehiro Ohtsuka, and Hajime Tanaka. Direct observation of a local structural mechanism for dynamic arrest. *Nat Mater*, 7(7):556–561, July 2008.

[81] R. J. Elliott, J. A. Krumhansl, and P. L. Leath. The theory and properties of randomly disordered crystals and related physical systems. *Reviews of Modern Physics*, 46:465–543, July 1974.

[82] S. N. Taraskin, Y. L. Loh, G. Natarajan, and S. R. Elliott. Origin of the Boson Peak in Systems with Lattice Disorder. *Physical Review Letters*, 86:1255–1258, February 2001.

[83] Walter Schirmacher, Gregor Diezemann, and Carl Ganter. Harmonic Vibrational Excitations in Disordered Solids and the “Boson Peak”. *Physical Review Letters*, 81:136–139, July 1998.

[84] Jan W. Kantelhardt, Stefanie Russ, and Armin Bunde. Vibrational models for the Boson peak. *Journal of Non-Crystalline Solids*, 307-310:96–102, September 2002.

[85] Walter Schirmacher, G. Diezemann, and C. Ganter. Model calculations for vibrational properties of disordered solids and the ? boson peak? *Physica B: Condensed Matter*, 263-264:160–162, March 1999.

[86] W. Schirmacher and G. Diezemann. Propagation and localisation of vibrational modes in 3dimensional disordered systems: the binary force constant model. *Ann. Phys.*, 8(7-9):727–732, November 1999.

[87] John C. Crocker and David G. Grier. Methods of Digital Video Microscopy for Colloidal Studies. *Journal of Colloid and Interface Science*, 179(1):298–310, April 1996.

[88] D. Kaya, N. L. Green, C. E. Maloney, and M. F. Islam. Normal Modes and Density of States of Disordered Colloidal Solids. *Science*, 329(5992):656–658, August 2010.

[89] Carolina Brito, Olivier Dauchot, Giulio Biroli, and Jean-Philippe Bouchaud. Elementary excitation modes in a granular glass above jamming. *Soft Matter*, 6(13):3013–3022, 2010.

[90] Michael Schindler and A. C. Maggs. Truncated correlations in video microscopy of colloidal solids. *Soft Matter*, 8(14):3864–3874, 2012.

[91] Sho Asakura and Fumio Oosawa. Interaction between particles suspended in solutions of macromolecules. *Journal of Polymer Science*, 33(126):183–192, 1958.

[92] A. Vrij. Polymers at interfaces and the interactions in colloidal dispersions. *Pure and Applied Chemistry*, 48(4):471–483, 1976.

[93] S. M. Ilett, A. Orrock, W. C. K. Poon, and P. N. Pusey. Phase behavior of a model colloid-polymer mixture. *Phys. Rev. E*, 51:1344–1352, Feb 1995.

[94] J. R. Savage, D. W. Blair, A. J. Levine, R. A. Guyer, and A. D. Dinsmore. Imaging the sublimation dynamics of colloidal crystallites. *Science*, 314(5800):795–798, 2006.

[95] J. R. Savage and A. D. Dinsmore. Experimental evidence for two-step nucleation in colloidal crystallization. *Phys. Rev. Lett.*, 102:198302, May 2009.

[96] Anna Stradner, Helen Sedgwick, Frederic Cardinaux, Wilson C. K. Poon, Stefan U. Egelhaaf, and Peter Schurtenberger. Equilibrium cluster formation in concentrated protein solutions and colloids. *Nature*, 432(7016):492–495, November 2004.

[97] Marie Adams, Zvonimir Dogic, Sarah L. Keller, and Seth Fraden. Entropically driven microphase transitions in mixtures of colloidal rods and spheres. *Nature*, 393(6683):349–352, May 1998.

[98] Marie Adams and Seth Fraden. Phase behavior of mixtures of rods (tobacco mosaic virus) and spheres (polyethylene oxide, bovine serum albumin). *Biophysical Journal*, 74(1):669 – 677, 1998.

[99] Rebecca W. Perry, Guangnan Meng, Thomas G. Dimiduk, Jerome Fung, and Vinothan N. Manoharan. Real-space studies of the structure and dynamics of self-assembled colloidal clusters. *Faraday Discuss.*, 159:211–234, 2012.

[100] Gregory E. Fernandes, Daniel J. Beltran-Villegas, and Michael A. Bevan. Interfacial colloidal crystallization via tunable hydrogel depletants. *Langmuir*, 24(19):10776–10785, 2008. PMID: 18774826.

[101] Shelley L Taylor, Robert Evans, and C Patrick Royall. Temperature as an external field for colloidpolymer mixtures: quenching by heating and melting by cooling. *Journal of Physics: Condensed Matter*, 24(46):464128, 2012.

[102] P. D. Kaplan, J. L. Rouke, A. G. Yodh, and D. J. Pine. Entropically driven surface phase separation in binary colloidal mixtures. *Phys. Rev. Lett.*, 72:582–585, Jan 1994.

[103] Anthony D Dinsmore, John C Crocker, and Arjun G Yodh. Self-assembly of colloidal crystals. *Current Opinion in Colloid & Interface Science*, 3(1):5 – 11, 1998.

[104] Laura Rossi, Stefano Sacanna, William T. M. Irvine, Paul M. Chaikin, David J. Pine, and Albert P. Philipse. Cubic crystals from cubic colloids. *Soft Matter*, 7:4139–4142, 2011.

[105] G. H. Koenderink, G. A. Vliegenthart, S. G. J. M. Kluijtmans, A. van Blaaderen, A. P. Philipse, and H. N. W. Lekkerkerker. Depletion-induced crystallization in colloidal rod-sphere mixtures. *Langmuir*, 15(14):4693–4696, July 1999.

[106] Keng-Hui Lin, John C. Crocker, Ana C. Zeri, and A. G. Yodh. Colloidal interactions in suspensions of rods. *Phys. Rev. Lett.*, 87:088301, Aug 2001.

[107] W.C.K. Poon, A.D. Pirie, M.D. Haw, and P.N. Pusey. Non-equilibrium behaviour of colloid-polymer mixtures. *Physica A: Statistical Mechanics and its Applications*, 235(12):110 – 119, 1997. Proceedings of the Workshop on Colloid Physics.

[108] H de Hek and A Vrij. Interactions in mixtures of colloidal silica spheres and polystyrene molecules in cyclohexane: I. phase separations. *Journal of Colloid and Interface Science*, 84(2):409 – 422, 1981.

[109] H de Hek and A Vrij. Interactions in mixtures of colloidal silica spheres and polystyrene molecules in cyclohexane. *Journal of Colloid and Interface Science*, 88(1):258 – 273, 1982.

[110] Robert I Feigin and Donald H Napper. Stabilization of colloids by free polymer. *Journal of Colloid and Interface Science*, 74(2):567 – 571, 1980.

[111] R Tuinier, J Rieger, and C.G de Kruif. Depletion-induced phase separation in colloid-polymer mixtures. *Advances in Colloid and Interface Science*, 103(1):1 – 31, 2003.

[112] Amber Sharma, Su Nee Tan, and John Y. Walz. Measurement of colloidal stability in solutions of simple, nonadsorbing polyelectrolytes. *Journal of Colloid and Interface Science*, 190(2):392 – 407, 1997.

[113] Shunxi Ji and John Y. Walz. Depletion forces and flocculation with surfactants, polymers and particles synergistic effects. *Current Opinion in Colloid & Interface Science*, 20(1):39 – 45, 2015.

[114] Edward S. Pagac, Robert D. Tilton, and Dennis C. Prieve. Depletion attraction caused by unadsorbed polyelectrolytes. *Langmuir*, 14(18):5106–5112, September 1998.

[115] P. Richetti and P. Kékicheff. Direct measurement of depletion and structural forces in a micellar system. *Phys. Rev. Lett.*, 68:1951–1954, Mar 1992.

[116] Janine L Burns, Yao de Yan, Graeme J Jameson, and Simon Biggs. Relationship between interaction forces and the structural compactness of depletion flocculated colloids. *Colloids and Surfaces A: Physicochemical and Engineering Aspects*, 162(13):265 – 277, 2000.

[117] Tara D. Edwards and Michael A. Bevan. Polymer mediated depletion attraction and interfacial colloidal phase behavior. *Macromolecules*, 45(1):585–594, January 2012.

[118] R. Verma, J. C. Crocker, T. C. Lubensky, and A. G. Yodh. Attractions between hard colloidal spheres in semiflexible polymer solutions. *Macromolecules*, 33(1):177–186, 2000.

[119] J.-L Doublier, C Garnier, D Renard, and C Sanchez. Proteinpolysaccharide interactions. *Current Opinion in Colloid & Interface Science*, 5(34):202 – 214, 2000.

[120] V.Ya. Grinberg and V.B. Tolstoguzov. Thermodynamic incompatibility of proteins and polysaccharides in solutions. *Food Hydrocolloids*, 11(2):145 – 158, 1997.

[121] A. Syrbe, W.J. Bauer, and H. Klostermeyer. Polymer science concepts in dairy systemsan overview of milk protein and food hydrocolloid interaction. *International Dairy Journal*, 8(3):179–193, March 1998.

[122] C.G de Kruif and R Tuinier. Polysaccharide protein interactions. *Food Hydrocolloids*, 15(46):555 – 563, 2001. 5th International Hydrocolloids Conference.

[123] Ad Overbeek, Fred Buckmann, Emilio Martin, Pablo Steenwinkel, and Tom Annable. New generation decorative paint technology. *Progress in Organic Coatings*, 48(24):125 – 139, 2003. Athens 2002.

[124] S. B. Zimmerman and A. P. Minton. Macromolecular crowding: Biochemical, biophysical, and physiological consequences. *Annual Review of Biophysics and Biomolecular Structure*, 22(1):27–65, 1993. PMID: 7688609.

[125] Allen P Minton. Implications of macromolecular crowding for protein assembly. *Current Opinion in Structural Biology*, 10(1):34 – 39, 2000.

[126] Henk NW Lekkerkerker and Remco Tuinier. *Colloids and the depletion interaction*, volume 833. Springer, 2011.

[127] Y. Mao, M. E. Cates, and H. N. W. Lekkerkerker. Depletion stabilization by semidilute rods. *Phys. Rev. Lett.*, 75:4548–4551, Dec 1995.

[128] Y. Mao, M. E. Cates, and H. N. W. Lekkerkerker. Theory of the depletion force due to rodlike polymers. *The Journal of Chemical Physics*, 106(9):3721–3729, 1997.

[129] Auvray, L. Solutions de macromolcules rigides : effets de paroi, de confinement et d'orientation par un coulement. *J. Phys. France*, 42(1):79–95, 1981.

[130] K. Yaman, C. Jeppesen, and C. M. Marques. Depletion forces between two spheres in a rod solution. *EPL (Europhysics Letters)*, 42(2):221, 1998.

[131] Martin Piech and John Y. Walz. Depletion interactions produced by nonadsorbing charged and uncharged spheroids. *Journal of Colloid and Interface Science*, 232(1):86 – 101, 2000.

[132] Paul van der Schoot. Depletion interactions in lyotropic nematics. *The Journal of Chemical Physics*, 112(20):9132–9138, 2000.

[133] A. W. C. Lau, Keng-Hui Lin, and A. G. Yodh. Entropic interactions in suspensions of semiflexible rods: Short-range effects of flexibility. *Phys. Rev. E*, 66:020401, Aug 2002.

[134] R Roth. Depletion potentials in colloidal mixtures of spheres and rods. *Journal of Physics: Condensed Matter*, 15(1):S277, 2003.

[135] L. Helden, R. Roth, G. H. Koenderink, P. Leiderer, and C. Bechinger. Direct measurement of entropic forces induced by rigid rods. *Phys. Rev. Lett.*, 90:048301, Jan 2003.

[136] M. Triantafillou and R. D. Kamien. Polymer shape anisotropy and the depletion interaction. *Phys. Rev. E*, 59:5621–5624, May 1999.

[137] N Doshi, G Cinacchi, J S van Duijneveldt, T Cosgrove, S W Prescott, I Grillo, J Phipps, and D I Gittins. Structure of colloidal sphereplate mixtures. *Journal of Physics: Condensed Matter*, 23(19):194109, 2011.

[138] L. Harnau and S. Dietrich. Depletion potential in colloidal mixtures of hard spheres and platelets. *Phys. Rev. E*, 69:051501, May 2004.

[139] Derek A. Triplett and Kristen A. Fichthorn. Entropic forces and directed alignment of hard squares in suspensions of rods and disks. *The Journal of Chemical Physics*, 133(14):–, 2010.

[140] P. W. Anderson. Through the glass lightly. *Science*, 267(5204):1615–1616, 1995.

[141] Francesco Sciortino. Disordered materials: One liquid, two glasses. *Nat Mater*, 1(3):145–146, November 2002.

[142] Kenneth A. Dawson. The glass paradigm for colloidal glasses, gels, and other arrested states driven by attractive interactions. *Current Opinion in Colloid & Interface Science*, 7(34):218 – 227, 2002.

[143] G. Foffi, C. De Michele, F. Sciortino, and P. Tartaglia. Scaling of dynamics with the range of interaction in short-range attractive colloids. *Phys. Rev. Lett.*, 94:078301, Feb 2005.

[144] Randall W. Hall* and Peter G. Wolynes. Intermolecular forces and the glass transition. *The Journal of Physical Chemistry B*, 112(2):301–312, 2008. PMID: 17990867.

[145] Ludovic Berthier and Gilles Tarjus. Nonperturbative effect of attractive forces in viscous liquids. *Phys. Rev. Lett.*, 103:170601, Oct 2009.

[146] Zexin Zhang, Peter J. Yunker, Piotr Habdas, and A. G. Yodh. Cooperative Rearrangement Regions and Dynamical Heterogeneities in Colloidal Glasses with Attractive Versus Repulsive Interactions. *Physical Review Letters*, 107:208303+, November 2011.

[147] G. Carini, G. D'Angelo, G. Tripodo, A. Fontana, A. Leonardi, G. A. Saunders, and A. Brodin. Excess of low-energy excitations in glasses. *Physical Review B*, 52:9342–9353, October 1995.

[148] L. Hong, B. Begen, A. Kisliuk, C. Alba Simionesco, V. N. Novikov, and A. P. Sokolov. Pressure and density dependence of the boson peak in polymers. *Physical Review B*, 78:134201+, October 2008.

[149] Y. Inamura, M. Arai, T. Otomo, N. Kitamura, and U. Buchenau. Density dependence of the boson peak of vitreous silica. *Physica B: Condensed Matter*, 284-288:1157–1158, July 2000.

[150] Robert O. Pohl, Xiao Liu, and EunJoo Thompson. Low-temperature thermal conductivity and acoustic attenuation in amorphous solids. *Reviews of Modern Physics*, 74(4):991–1013, October 2002.

[151] Hiroshi Shintani and Hajime Tanaka. Universal link between the boson peak and transverse phonons in glass. *Nat Mater*, 7(11):870–877, November 2008.

[152] Silke Henkes, Carolina Brito, and Olivier Dauchot. Dynamical fluctuations close to Jamming versus Vibrational Modes : a pedagogical discussion illustrated on hard spheres simulations, colloidal and granular experiments, December 2011.

[153] Leonardo E. Silbert, Andrea J. Liu, and Sidney R. Nagel. Normal modes in model jammed systems in three dimensions. *Physical Review E*, 79:021308+, February 2009.

[154] P. M. Derlet, R. Maaß, and J. F. Löffler. The Boson peak of model glass systems and its relation to atomic structure. *The European Physical Journal B - Condensed Matter and Complex Systems*, 85(5):1–20, May 2012.

[155] P. Jund, D. Caprion, and R. Jullien. Structural and vibrational properties of a soft-sphere glass: Influence of the quenching rate. *Philosophical Magazine Part B*, 77(2):313–320, February 1998.

[156] H. R. Schober. Vibrations and relaxations in a soft sphere glass: boson peak and structure factors. *Journal of Physics: Condensed Matter*, 16(27):S2659–S2670, June 2004.

[157] Ahmed M. Alsayed, Yilong Han, and Arjun G. Yodh. Melting and geometric frustration in temperature-sensitive colloids. In *Microgel Suspensions*, pages 229–281. Wiley-VCH Verlag GmbH & Co. KGaA, 2011.

[158] Y. Han, N. Y. Ha, A. M. Alsayed, and A. G. Yodh. Melting of two-dimensional tunable-diameter colloidal crystals. *Physical Review E*, 77(4):041406+, April 2008.

[159] Z. Burda, A. Görlich, A. Jarosz, and J. Jurkiewicz. Signal and noise in correlation matrix. *Physica A: Statistical Mechanics and its Applications*, 343:295–310, November 2004.

[160] Neil W. Ashcroft and N. David Mermin. *Solid State Physics*. Cengage Learning, 1 edition, January 1976.

[161] Ke Chen, Tim Still, Kevin B. Aptowicz, Sam Schoenholz, Michael Schindler, A. C. Maggs, Andrea J. Liu, and A. G. Yodh. Phonons in pristine and imperfect two-dimensional soft colloidal crystals, December 2012.

[162] Zhengyou Liu, Xixiang Zhang, Yiwei Mao, Y. Y. Zhu, Zhiyu Yang, C. T. Chan, and Ping Sheng. Locally Resonant Sonic Materials. *Science*, 289(5485):1734–1736, September 2000.

[163] T. Still, W. Cheng, M. Retsch, R. Sainidou, J. Wang, U. Jonas, N. Stefanou, and G. Fytas. Simultaneous Occurrence of Structure-Directed and Particle-Resonance-Induced Phononic Gaps in Colloidal Films. *Physical Review Letters*, 100(19):194301+, May 2008.

[164] G. Petekidis, L. A. Galloway, S. U. Egelhaaf, M. E. Cates, and W. C. K. Poon. Mixtures of colloids and wormlike micelles: phase behavior and kinetics. *Langmuir*, 18(11):4248–4257, 2002.

[165] Paul J. Missel, N. A. Mazer, G. B. Benedek, C. Y. Young, and Martin C. Carey. Thermodynamic analysis of the growth of sodium dodecyl sulfate micelles. *The Journal of Physical Chemistry*, 84(9):1044–1057, 1980.

[166] Jean-Pierre Hansen and Ian R. McDonald. *Theory of Simple Liquids, 2nd*. Academic Press, 1986.

[167] E M Chan. Two-dimensional born-green-yvon and other integral equations. *Journal of Physics C: Solid State Physics*, 10(18):3477, 1977.

[168] Li-Jen Chen, Shi-Yow Lin, Chiung-Chang Huang, and En-Ming Chen. Temperature dependence of critical micelle concentration of polyoxyethylenated non-ionic surfactants. *Colloids and Surfaces A: Physicochemical and Engineering Aspects*, 135(13):175 – 181, 1998.

[169] Jacob N. Israelachvili. *Intermolecular and Surface Forces*. Academic Press, 1 edition, 1985.

[170] J. Baumgartl and C. Bechinger. On the limits of digital video microscopy. *EPL (Europhysics Letters)*, 71(3):487, 2005.

[171] Marco Polin, David G. Grier, and Yilong Han. Colloidal electrostatic interactions near a conducting surface. *Phys. Rev. E*, 76:041406, Oct 2007.

[172] Henry G. Thomas, Aleksey Lomakin, Daniel Blankschtein, and George B. Benedek. Growth of mixed nonionic micelles. *Langmuir*, 13(2):209–218, 1997.

[173] Andrew W. Wills, David J. Michalak, Peter Ercius, Ethan R. Rosenberg, Talita Perciano, Daniela Ushizima, Rory Runser, and Brett A. Helms. Block copolymer packing limits and interfacial reconfigurability in the assembly of periodic mesoporous organosilicas. *Advanced Functional Materials*, 25(26):4120–4128, 2015.

[174] Seung Hyun Kim, Matthew J. Misner, Ling Yang, Oleg Gang, Benjamin M. Ocko, , and Thomas P. Russell*. Salt complexation in block copolymer thin films. *Macromolecules*, 39(24):8473–8479, 2006.

[175] Graham S. MacGlashan, Yuri G. Andreev, and Peter G. Bruce. Structure of the polymer electrolyte poly(ethylene oxide)6:liasf6. *Nature*, 398(6730):792–794, April 1999.

[176] Francesco Varrato, Lorenzo Di Michele, Maxim Belushkin, Nicolas Dorsaz, Simon H. Nathan, Erika Eiser, and Giuseppe Foffi. Arrested demixing opens route to bigels. *Proceedings of the National Academy of Sciences*, 109(47):19155–19160, 2012.

[177] L. Di Michele, D. Fiocco, F. Varrato, S. Sastry, E. Eiser, and G. Foffi. Aggregation dynamics, structure, and mechanical properties of bigels. *Soft Matter*, 10:3633–3648, 2014.

[178] Viva R. Horowitz, Lauren A. Janowitz, Aaron L. Modic, Paul A. Heiney, and Peter J. Collings. Aggregation behavior and chromonic liquid crystal properties of an anionic monoazo dye. *Phys. Rev. E*, 72:041710, Oct 2005.

[179] John Lydon. Chromonic review. *J. Mater. Chem.*, 20:10071–10099, 2010.

[180] John Lydon. Chromonic mesophases. *Current Opinion in Colloid & Interface Science*, 8(6):480 – 490, 2004.

[181] Yu. A. Nastishin, H. Liu, S. V. Shiyanovskii, O. D. Lavrentovich, A. F. Kostko, and M. A. Anisimov. Pretransitional fluctuations in the isotropic phase of a lyotropic chromonic liquid crystal. *Phys. Rev. E*, 70:051706, Nov 2004.

[182] J. Bergenholtz and M. Fuchs. Nonergodicity transitions in colloidal suspensions with attractive interactions. *Phys. Rev. E*, 59:5706–5715, May 1999.

[183] L. Fabbian, W. Götze, F. Sciortino, P. Tartaglia, and F. Thiery. Ideal glass-glass transitions and logarithmic decay of correlations in a simple system. *Phys. Rev. E*, 59:R1347–R1350, Feb 1999.

[184] F. Sciortino and P. Tartaglia. Glassy colloidal systems. *Advances in Physics*, 54(6-7):471–524, 2005.

[185] T. Eckert and E. Bartsch. Re-entrant glass transition in a colloid-polymer mixture with depletion attractions. *Phys. Rev. Lett.*, 89:125701, Aug 2002.

[186] E. Zaccarelli, G. Foffi, K. A. Dawson, S. V. Buldyrev, F. Sciortino, and P. Tartaglia. Confirmation of anomalous dynamical arrest in attractive colloids: A molecular dynamics study. *Phys. Rev. E*, 66:041402, Oct 2002.

[187] Antonio M. Puertas, Matthias Fuchs, and Michael E. Cates. Comparative simulation study of colloidal gels and glasses. *Phys. Rev. Lett.*, 88:098301, Feb 2002.

[188] Matthieu Wyart. Scaling of phononic transport with connectivity in amorphous solids, March 2010.

[189] Ryoichi Yamamoto and Akira Onuki. Dynamics of highly supercooled liquids: Heterogeneity, rheology, and diffusion. *Phys. Rev. E*, 58:3515–3529, Sep 1998.

[190] Donna N. Perera and Peter Harrowell. Relaxation dynamics and their spatial distribution in a two-dimensional glass-forming mixture. *The Journal of Chemical Physics*, 111(12):5441–5454, 1999.

[191] Sharon J. Gerbode, Desmond C. Ong, Chekesha M. Liddell, and Itai Cohen. Dislocations and vacancies in two-dimensional mixed crystals of spheres and dimers. *Phys. Rev. E*, 82:041404, Oct 2010.

[192] Norman F. Carnahan and Kenneth E. Starling. Equation of state for nonattracting rigid spheres. *The Journal of Chemical Physics*, 51(2):635–636, 1969.

[193] M. D. Ediger. Spatially heterogeneous dynamics in supercooled liquids. *Annual Review of Physical Chemistry*, 51(1):99–128, 2000. PMID: 11031277.

[194] L. Berthier, G. Biroli, J.-P. Bouchaud, L. Cipelletti, D. El Masri, D. L'Hôte, F. Ladieu, and M. Pierno. Direct experimental evidence of a growing length scale accompanying the glass transition. *Science*, 310(5755):1797–1800, 2005.

[195] Peter Yunker, Zexin Zhang, Kevin B. Aptowicz, and A. G. Yodh. Irreversible Rearrangements, Correlated Domains, and Local Structure in Aging Glasses. *Physical Review Letters*, 103(11):115701+, September 2009.

[196] H. N. W. Lekkerkerker, W. C.-K. Poon, P. N. Pusey, A. Stroobants, and P. B. Warren. Phase behaviour of colloid + polymer mixtures. *EPL (Europhysics Letters)*, 20(6):559, 1992.

[197] Carlton F. Brooks, Gerald G. Fuller, Curtis W. Frank, and Channing R. Robertson. An interfacial stress rheometer to study rheological transitions in monolayers at the airwater interface. *Langmuir*, 15(7):2450–2459, 1999.

[198] Sven Reynaert, Paula Moldenaers, and Jan Vermant. Interfacial rheology of stable and weakly aggregated two-dimensional suspensions. *Phys. Chem. Chem. Phys.*, 9:6463–6475, 2007.

[199] Yilong Han, Yair Shokef, Ahmed M. Alsayed, Peter Yunker, Tom C. Lubensky, and Arjun G. Yodh. Geometric frustration in buckled colloidal monolayers. *Nature*, 456(7224):898–903, December 2008.

[200] Yair Shokef, Yilong Han, Anton Souslov, A. G. Yodh, and Tom C. Lubensky. Buckled colloidal monolayers connect geometric frustration in soft and hard matter. *Soft Matter*, 9:6565–6570, 2013.

[201] Sang-Hyuk Lee, Yohai Roichman, Gi-Ra Yi, Shin-Hyun Kim, Seung-Man Yang, Alfons van Blaaderen, Peter van Oostrum, and David G. Grier. Characterizing and tracking single colloidal particles with video holographic microscopy. *Opt. Express*, 15(26):18275–18282, Dec 2007.